Studying Partially Ordered Systems Using Stochastic Differential Equations



Edward Rolls

Pembroke College

University of Oxford

A thesis submitted for the degree of

Doctor of Philosophy

Trinity 2018

A heartfelt thanks to my family and friends for their support in both this and all of my endeavours

Acknowledgements

There are many that I'd like to thank for their contributions, both direct and indirect, to this thesis; apologies to anybody who I have missed out.

First and foremost many thanks to Radek Erban for supervising me these past four years - he has always been happy to help whenever asked and been a fantastic guiding influence on the direction of the work contained. Chapter 2 was made in collaboration with Yuichi Togashi, and Chapter 4 with Apala Majumdar; many thanks to both of them also for their contributions. Also thanks to Martin Robinson for sharing the code behind his paper on which large parts of Chapter 4 is based.

In the mathematics department, many thanks to the entire WCMB group for stimulating discussions about work. In particular, thanks to Daniel Humphries and Jonathan Harrison, with whom I shared an office for three years, for putting up with a not-insignificant number of minor queries about this work and many other topics.

Outside of mathematics, I extend many thank yous to my family and friends for keeping me sane throughout the process of working on my DPhil; my membership of both PCBC and then OUTriC have been major parts of my life beyond this thesis, so thanks to both of them also. I should also thank the coffee shops of Oxford and South West London for their help throughout the thesis writing process.

My place as a student at the University of Oxford has been funded by the EPSRC via the DTC (grant number EP/G03706X/1), with additional funding from the Royal Society University Research Fellowship awarded to Radek Erban to allow both published papers to go open source, as well as the Isaac Newton Institute for Mathematical Sciences, Cambridge, for hosting Radek and myself during the programme 'Stochastic Dynamical Systems in Biology: Numerical Methods and Applications'.

Abstract

This thesis looks at two different problems in the field of partially ordered systems - modelling biopolymers on multiple scales as well as modelling two-dimensional nematic liquid crystal wells - and seeks to gain insight using stochastic differential equations, through mathematical analysis and numerical simulations.

In the field of biopolymers, we generalize existing models for a coarse-grained polymer to multiple resolutions, which allows for faster computations while maintaining a high level of detail in regions of interest. This is done for two bead spring models; the Rouse model, which does not account for hydrodynamic interactions, as well as the bead-spring model with hydrodynamic interactions. For both models mathematical analysis is done to find expressions for global statistics to derive scaling laws for the models. This is implemented by generalizing existing algorithms using a multi-resolution approach which utilizes multiple spatial and temporal scales. These simulations show that the scaling laws for multiple resolutions match expected analytic results through simulations. For the Rouse model, a model for the binding of a protein to DNA is introduced, along with a mechanism for changing resolutions along the filament on-the-fly. Within reasonable error, the results for the chain in multiple resolutions matches the chain modelled entirely in high-resolution.

The work on nematic liquid crystals is concerned with a stochastic dynamics model of nematic liquid crystals contained within a square well, looking at their behaviour under Brownian motion using the Gay-Berne potential. In particular, we are interested in the parameter regimes which are responsible for different types of steady states to form in the system and whether steady states suggested by continuum modelling are stable.

Contents

1 Introduction **1**

1.1 Brownian Dynamics 1
1.2 Biological Background to Polymer Modelling 6
1.3 Polymer Modelling 9
1.4 Multiscale Modelling 13
1.5 Physical Background to Nematic Liquid Crystals 15
1.6 Modelling Nematic Liquid Crystals 16
1.7 Confined Systems of Nematic Liquid Crystals 22
1.8 Structure of this thesis 24

2 Varying the resolution of the Rouse model on temporal and spatial scales: application to multiscale modelling of DNA dynamics **26**

2.1 Multi-resolution bead-spring model 28
2.2 Macroscopic properties and parameterizations of multi-resolution bead-spring models 32
2.2.1 Translational diffusion coefficient 34
2.2.2 End-to-end distance 36
2.2.3 Optimal model refinement in time and space 39
2.2.4 Simulation results 42
2.2.4.1 Comparison at equilibrium 42
2.2.4.2 Compacting the filament 44
2.3 DNA binding model 46
2.3.1 Resolution increase with MCMC 47
2.3.2 Model description 50
2.3.3 Results of the Binding Model 53
2.4 Discussion 56

3 Multi-resolution polymer Brownian dynamics with hydrodynamic interactions **59**
3.1 Multi-resolution bead-spring model 60
3.1.1 Static Description 61
3.1.2 Dynamic Model Description 62
3.2 Approximation of the Diffusion Coefficient and Ideal Parameterization 65
3.2.1 Diffusion Approximation 65
3.2.2 Scaling of Parameters 71
3.3 Simulation Method 73
3.4 Simulations 77
3.5 Discussion 84

4 Investigating Steady States of Confined Nematic Liquid Crystal Systems in Two Dimensions **86**
4.1 Methods 87
4.1.1 Gay-Berne Potential 88
4.1.2 Equations of Motion 89
4.1.3 Numerical Scheme 92
4.1.4 Boundary Conditions 95
4.1.5 Nematic Equilibria 95
4.1.6 Initial Conditions 97
4.1.7 The Scalar Comparison Parameter 100
4.2 Results 101
4.2.1 Random Configurations 102
4.2.2 Systems Which Begin in Nematic Equilibria 105
4.3 Discussion 106

5 Conclusion **109**
5.1 Further Extensions to my Work 110
5.2 How my work relates to the field 112

Bibliography **116**

List of Figures

1.1 Folding of DNA on multiple scales 8
1.2 A summary of different approaches to modelling DNA at microscopic scales 14
1.3 A description of the orientation of an NLC molecule 17
1.4 Steady states forming in liquid crystal wells 23

2.1 Schematic of the multi-resolution bead-spring model 29
2.2 The rms end-to-end distance for a compacted filament re-extending towards equilibrium 45
2.3 Schematic of the resolution increase MCMC model 48
2.4 Snapshots of the DNA binding model 51
2.5 A comparison of the probability of binding of the protein to the DNA filament between the single scale and OMR models 55

3.1 The difference between the matrix formulation for the diffusion coefficient and the long chain limit 81
3.2 CPU times to simulate multi-resolution and single-scale models . . . 83

4.1 Behaviour of the GB potential 90
4.2 The three nematic equilibria studied 97
4.3 Schematic of the growth of a system of beads into a 'random' configuration 99
4.4 Demonstration of the four different initial configurations in the 'growing' system 100
4.5 Demonstration of different values of the scalar comparison parameter 102
4.6 Comparison of the formation of LdG nematic equilibria from random initial configuration 104
4.7 The stability of LdG suggested nematic equilibria for different temperatures k_BT 106

List of Tables

1.1 Brief summary of liquid crystal models introduced 21

2.1 Parameters of the OMR model system used to demonstrate consistency 43
2.2 Comparison of results between the original Rouse model, the multi-resolution Rouse model and analytic results 44
2.3 Parameters of OMR systems used to test resolution regimes outside of equilibrium 45
2.4 Parameter selection for the DNA binding model 54

3.1 An explanation of the simulation method running on multiple timesteps 75
3.2 Results for diffusion and the rms end-to-end distance in single-scale simulations 80
3.3 Results for diffusion and the rms end-to-end distance in multi-resolution simulations 83

5.1 Brief summary of hybrid polymer models 114

List of Abbreviations

3C	Chromosome conformation capture
BD	Brownian dynamics
bp	base pairs
CG	Coarse-grained moleculdar dynamics
DPD	Dissipative particle dynamics
EM	Euler-Maruyama
EV	Excluded volume
FENE	Finitely extensible nonlinear elastic
FJC	Freely jointed chain
FP	Fokker-Planck
GB	Gay-Berne
GC	Gaussian chain
HI	Hydrodynamic interactions
LdG	Landau-de Gennes
LCD	Liquid crystal display
LJ	Lennard-Jones
MCMC	Markov chain Monte Carlo
MD	Molecular dynamics
NEBD	Non-equilibrium Brownian dynamics
NLC	Nematic liquid crystal
OMR	Optimal multi-resolution
OU	Ornstein-Uhlenbeck
QM/MM	Quantum mechanics/molecular mechanics hybrid modelling
rms	Root mean-squared
RPY	Rotne-Prager-Yamakawa
SDE	Stochastic differential equation
WORS	Well order reconstuction solution

List of Symbols

$\mathbf{a}$	The position of the DNA binding factor
$\mathbf{B}_{nm}$	Cholesky decomposition of the mobility matrix $\mathbf{H}_{nm}$
b_n	Kuhn length of the n^{th} bead
$\widetilde{b}_\alpha$	The Kuhn length in the α^{th} region of a multi-resolution bead-spring model
$\mathbf{C}$	Stationary covariance matrix
C	Proposed chain in the MCMC resolution increase model
D_G	Translational diffusion coefficient
D_P	Particle diffusion coefficient
$\mathrm{d}X$	A differential in X
d	Diameter of a rod in Onsager theory
d_0	Initial distance from the filament
d_B	Binding radius
d_∞	Distance above which a particle drifts to infinity in the DNA binding model
E	Scalar comparison parameter
$\mathbf{F}_n$	Inter-bead force
$\widetilde{\mathbf{F}}^t_{mn}$	Discretized force
$\mathbf{f}_n$	Random thermal noises acting on the n^{th} bead
f	Free energy
$G_n^{(\nu)}(x)$	Gegenbauer polynomial
$\mathbf{H}_{nm}$	Mobility matrix
$\widehat{H}_{nm}$	Pre-averaged mobility matrix
h^*	Strength of HI parameter
$\mathbf{I}$	Identity matrix
J_n	A random variable which takes either $+1$ or -1 with equal probability
K	Domain size of a confined liquid crystal system

k_B	Boltzmann's constant
k_n	Spring constant of the n^{th} bead
L	Length of a rod in Onsager theory
M	Number of new beads on a chain when the resolution increases
$\mathbf{m}$	Diagonal matrix of particle masses
m_i	The weight of particle i
$\mathcal{N}(\alpha, \beta^2)$	The normal distribution with mean α and variance β^2
$\widetilde{N}_\alpha$	The number of particles in the α^{th} region of a multi-resolution bead-spring model
N	The number of particles or molecules in a system
N_K	The number of particles in each row of the initial grid for the confined NLC system
$\mathbf{n}$	The direction of the nematic order
$P_2(x)$	The second Legendre polynomial
P_B	Probability of binding
$\mathbf{p}$	The vector of particle momenta
p_i	The momentum of the i^{th} particle
$\mathbf{Q}$	The Q-tensor
$Q(j, i)$	Indicator function equal to 1 if j is a factor of i, equal to 0 otherwise
$\mathbf{q}$	The vector of particle positions
$\mathbf{q}_\alpha$	The boundary beads in the DNA binding model
q_i	The position of the i^{th} particle
$\mathbb{R}$	The real numbers
$\mathbb{R}^{m \times n}$	A matrix of real numbers size $m \times n$
$\mathbf{R}$	End-to-end vector
$\mathbf{R}_n$	The n^{th} bond vector
R	Number of regions to describe a multi-resolution bead-spring model
$\mathbf{r}_G^t$	Centre of mass of a polymer at time t
$\mathbf{r}_h$	Hydrodynamic center of resistance
$\widehat{\mathbf{r}}_{mn}$	Unit vector between beads m and n

$\mathbf{r}_n$	Position vector of the n^{th} particle
r_c	Cutoff radius
r_I	Resolution increase radius
$\mathbb{S}^1$	The unit circle
S	Scalar order parameter
s	Eccentricity of a NLC molecule
s_α	Resolution of the α^{th} region
$\mathbf{T}$	Torque
T	Temperature
t	Time
t_{grow}	Time to 'grow' a system of NLCs
$U(\mathbf{q})$	A potential acting on the set of particle positions $\mathbf{q}$
U_{ij}	Pairwise interaction potential between particles i and j
$\mathbf{u}$	The orientation of a particle in a liquid crystal system
$\mathbf{v}_n$	Translational velocity vector for the n^{th} particle
$\mathbf{W}$	A vector of Wiener processes
$W(t)$	Wiener process at time t
X_n, Y_n	The state of a system at the n^{th} step
Z	Zoom out factor
Γ	Circle of allowable points
$\Gamma(x)$	The gamma function
γ	Friction coefficient
Δt_n	Timestep associated with the n^{th} bead
$\widetilde{\Delta t}_\alpha$	The timestep in the α^{th} region of a multi-resolution bead-spring model
$\delta_{\alpha\beta}$	Kronecker delta function equal to 1 if $\alpha = \beta$; equal to 0 otherwise
$\delta(y)$	Continuous function on the real numbers equal to 1 if $y = 0$; equal to 0 otherwise
δt	The size of a timestep in a random walk
δx	The size of a spatial step in a random walk

ζ_n	Frictional drag coefficient of the n^{th} bead
ζ_t, ζ_r	Translational and angular friction constants
η	Solvent viscosity
κ	Molecular aspect ratio
κ'	Well depth ratio
λ	Force applied to ensure unit vector for orientation
μ	rms end-to-end distance
ξ	Normally randomly distributed variable with mean 0 and variance 1
$\widetilde{\boldsymbol{\rho}}_n^t$	Discretized noise term
ρ	Particle density
$\sigma(\mathbf{u}_n, \mathbf{u}_m, \widehat{\mathbf{r}}_{nm})$	Shape parameter
σ_e	NLC molecule length
σ_n	Bead radius of the n^{th} bead
σ_s	NLC molecule width
$\widetilde{\sigma}_\alpha$	The bead radius in the α^{th} region of a multi-resolution bead-spring model
$\Phi(\mathbf{r}_{nm})$	Probability distribution for the vector between the n^{th} and m^{th} bead
$\phi(C)$	Probability distribution for a chain C of beads
$\Psi(\{\mathbf{r}_n\})$	Conformational distribution function of a chain
ψ_n	Distribution for the n^{th} bond vector
$\boldsymbol{\omega_n}$	Angular velocity vector for the n^{th} particle
ω	NLC particle mass
Ω	Mass of a polymer filament
$\mathbf{0}$	The zero matrix
$\emptyset$	The empty set
$\langle * \rangle_{\text{eq}}$	Equilibrium average

Chapter 1

Introduction

Contained in Chapter 1 is an introduction to the material covered in the thesis. In Section 1.1, I begin with a look at Brownian dynamics (BD) as a model, by doing a non-rigorous derivation of the governing equations for the work in this thesis. In Section 1.2, I give a biological introduction to polymer modelling, to motivate the work in Chapter 2 and Chapter 3, followed by a summary in Section 1.3 of previous approaches taken to model polymers with BD and in Section 1.4 a look at the use of multiscale modelling in other fields.

The remainder of the Introduction is focused on my work on nematic liquid crystal (NLC) molecules in confined domains for Chapter 4, with a physical background given in Section 1.5 to motivate the simulations. A brief summary of modelling NLC molecules is given in Section 1.6, followed by specific experimental and modelling approaches for the confined problem in Section 1.7.

The overall structure of the thesis is given in Section 1.8.

1.1 Brownian Dynamics

BD is a modelling approach in which the behaviour of entities within a system can be written in terms of stochastic equations for their time evolution. This approach

is valid where some entities of the system (in our case beads on a chain or NLC molecules) move on both temporal and spatial scales significantly different to the underlying solvent.

It is possible to rigorously define BD in greater depth than will be done here, but as this has been done elsewhere [33, 99, 124], we shall simply introduce the concept and outline the approach taken to derive it.

BD is a *stochastic model*, which is a type of model which contains at least one random variable. The first study of Brownian motion is often attributed to Robert Brown in 1828 [19], with a more rigorous mathematical basis being formed behind the work in the late 1800's and 1900's.

Perhaps the simplest example of a stochastic model is the random walk [42] and is often used to introduce BD [99]. We shall consider a spatial random walk, but it can be used to describe non-spatial phenomena from gambling to stock prices. A random walk occurs in a discrete time frame, where the next position of a particle in a system is given as the current position plus a random variable. If we describe the position of our particle at step n as X_n with spatial step size δx then the random walk gives the position of the particle at step $n+1$ as:

$$X_{n+1} = X_n + \delta x J_n, \tag{1.1}$$

where J_n is equal to either $+1$ or -1 with equal probability.

We can also consider the model from an alternative perspective, where we define the timestep δt to be the time taken between each step, and let $t_n = n\delta t$ be the n^{th} step. If $Y_n = Y(t_n)$ is the state of the system at step n, then we describe the system as:

$$Y_{n+1} = Y_n + \sqrt{\delta t} J_n, \tag{1.2}$$

where we have let the size of the step δx be equal to $\sqrt{\delta t}$ as a scaling relationship

between the step sizes in space and time.

In a limit known as the *diffusion limit*, where we hold this scaling $\delta t = \delta x^2$ as $\delta t \to 0$, we can create the notion of an everywhere continuous, but almost nowhere smooth path which is called a *Wiener process* $W(t)$. The Wiener process is the sum of the random steps from the random walk in the diffusion limit, which can be given via the Central Limit Theorem to be described by the normal distribution [99]

$$W(t) \sim \mathcal{N}(0, t), \tag{1.3}$$

with the special property that for any $t, s \in \mathbb{R}$ we have $W(t) - W(s) \sim \mathcal{N}(0, |t - s|)$, so that the Wiener process is a Markov process, i.e. it is memoryless.

Now we have introduced the concept of the Wiener process $W(t)$, we can utilize this description to define a *stochastic differential equation* (SDE). If we have smooth functions $a(x, t)$ and $b(x, t)$ then the limit of a more general version of the random walk [99] can be written in terms of differentials

$$\mathrm{d}X = a(X, t)\mathrm{d}t + b(X, t)\mathrm{d}W, \tag{1.4}$$

which is a general scalar SDE.

A specific example of an SDE is the *Ornstein-Uhlenbeck* (OU) equation for the motion of particles in a system of N non-interacting particles with mass m_i. The momentum p_i of the i^{th} particle is given by the SDE:

$$\mathrm{d}p_i = -\gamma p_i \mathrm{d}t + \sqrt{2\gamma k_B T m_i}\mathrm{d}W, \tag{1.5}$$

for $\gamma > 0$, which samples the Gibbs-Boltzmann distribution [99] with temperature T and Boltzmann's constant k_B. In order to complete the equations of motion of the

system there is a differential equation to give the position q_i of the i^{th} particle:

$$\mathrm{d}q_i = m_i^{-1} p_i \mathrm{d}t. \tag{1.6}$$

In order to define *Langevin dynamics*, we consider a model for a thermal bath, in which a single heavy particle interacts with a large number of light particles, modelled as coupled oscillators with potential for the heavy particle $U(q)$. It is possible to show that under certain conditions the action of the light particles on the heavy particle can be approximated as a Wiener process. This gives the equation of motions of the heavy particle as an OU process with an additional term for the action of the potential [36, 99]:

$$\begin{aligned} \mathrm{d}q &= m^{-1} p \mathrm{d}t, \\ \mathrm{d}p &= -U'(q)\mathrm{d}t - \gamma p \mathrm{d}t + \sqrt{2\gamma k_B T m}\mathrm{d}W \end{aligned} \tag{1.7}$$

which is known as a *Langevin equation* and γ is known as the friction coefficient.

This can be extended to a system of N heavy particles with equations of motion for momentum $\mathbf{p} \in \mathbb{R}^{3N}$ and position $\mathbf{q} \in \mathbb{R}^{3N}$ in vectoral form:

$$\begin{aligned} \mathrm{d}\mathbf{q} &= \mathbf{m}^{-1}\mathbf{p}\mathrm{d}t, \\ \mathrm{d}\mathbf{p} &= -\nabla U(\mathbf{q})\mathrm{d}t - \gamma \mathbf{p}\mathrm{d}t + \sqrt{2\gamma k_B T}\mathbf{m}^{1/2}\mathrm{d}\mathbf{W}, \end{aligned} \tag{1.8}$$

where $\mathbf{m} \in \mathbb{R}^{3N\times 3N}$ is a diagonal matrix with elements as the weights of each particle

$$\mathbf{m} = \begin{pmatrix} m_1 & 0 & 0 & 0 & \dots & 0 \\ 0 & m_1 & 0 & 0 & \dots & 0 \\ 0 & 0 & m_1 & 0 & \dots & 0 \\ 0 & 0 & 0 & m_2 & \dots & 0 \\ \vdots & \vdots & \vdots & \vdots & \ddots & \vdots \\ 0 & 0 & 0 & 0 & \dots & m_N \end{pmatrix},$$

$\mathbf{W}$ is a vector of $3N$ independent Wiener processes and the potential $U(\mathbf{q})$ may include interaction terms between multiple heavy particles.

If we take the limit for large γ, known as the *overdamped* limit, this results in dynamics which are dominated by collisional effects rather than particle acceleration, with equations

$$\begin{aligned} \mathrm{d}\mathbf{q} &= \mathbf{m}^{-1}\mathbf{p}\mathrm{d}t, \\ 0 &= -\nabla U(\mathbf{q})\mathrm{d}t - \gamma\mathbf{p}\mathrm{d}t + \sqrt{2\gamma k_B T}\mathbf{m}^{1/2}\mathrm{d}\mathbf{W}, \end{aligned} \tag{1.9}$$

and if we solve this we find an SDE for $\mathbf{q}$ given by

$$\mathrm{d}\mathbf{q} = -\gamma^{-1}\mathbf{m}^{-1}\nabla U(\mathbf{q})\mathrm{d}t + \sqrt{\frac{2k_B T}{\gamma}}\mathbf{m}^{-1/2}\mathrm{d}\mathbf{W}, \tag{1.10}$$

which is known as *Brownian dynamics*, which is the foundation for the models contained within this thesis.

For further reading, there are many texts on the properties of BD models [36,124], as well as material for general simulation methods [57,83,131].

1.2 Biological Background to Polymer Modelling

Chapter 2 and Chapter 3 of this thesis are looking at the behaviour of polymers, motivated primarily by biopolymers. Chapter 2 looks primarily at the application of polymer modelling to DNA polymers, but the work of Chapter 3 could be applied to other polymeric structures in which BD modelling is a valid modelling approach to take.

Inside a living cell we see a variety of structures which can be analyzed through polymer modelling. Examples of application areas include protein filaments [70, 72, 97, 104], cytoskeletal filaments like actin [7, 141], RNA [182, 199], block copolymers in nanotechnology to act as drug carriers [122], as well as DNA filaments [93, 94, 106, 172, 174, 201], which is where much of the focus of Chapter 2 lies.

One of the main biological phenomena that we seek to understand through polymer modelling is the structure and folding of DNA. This is necessary in order to unlock the ability to answer important biological questions, ranging from the accessibility for relevant proteins to DNA, through to gene distribution [93]. Inside the cell nucleus, genetic information is stored within strands of long and thin DNA fibres, which are separated into chromosomes. These DNA fibres are folded into structures related to the function of the genes contained [43]. Different genes can be enhanced or inhibited depending upon this structure. Folding also minimizes space taken up in the cell by DNA [86], and can be unfolded when required by the cell for different stages in the cell cycle or to alter gene expression.

The folding of DNA occurs on multiple scales as shown in Figure 1.1. On a microscopic scale, DNA is wrapped around histone proteins to form the nucleosome structure [194]. This in turn gets folded into a chromatin fibre which gets packaged into progressively higher order structures until we reach the level of the entire chromosome [43]. The finer points of how the nucleosome packing occurs on the chromatin fibre and how these are then packaged into higher-order structures is still a subject of

much debate, with long-held views regarding mesoscopic helical fibres becoming less fashionable in favour of more irregular structures in vivo [114].

In the most compact form of chromatin, many areas of DNA are not reachable for vital reactions such as transcription [43]. One potential explanation to how this is overcome by the cell is to position target DNA segments at the surface of condensed domains when it is needed [27, 113], so that transcription factors can find expressed genes without having to fit into these tightly-packed structures. If we have a greater understanding of the physics behind how DNA folds and moves, then this would help scientists answer these questions.

Modelling approaches to DNA can be informed by recent developments in experimental techniques. Fluorescence *in situ* hybridization (FISH) experiments [163], in combination with live cell imaging [20], have revealed much about the organization of chromosomes. Chromosome conformation capture (3C)-related techniques [30, 31], particularly at a genome-wide level using high-throughput sequencing like Hi-C [101], provide information on the spatial proximity in the chromosomes, although in an averaged manner in most cases. Using the experimental restraints, three dimensional structures are reconstructed [34]. These restraints [51, 183] as well as site-specific mechanical properties (e.g. rDNA) [195] can be also incorporated into polymer models, to consider dynamic behaviour. Recent Hi-C experiments also revealed fine structures such as loops induced by DNA-binding proteins such as CCCTC-binding factor (CTCF) and cohesin [165]. In the framework of polymer models, such loop formation by binding of proteins could be modelled by the strings and binders switch model [10] and similar models [18]. Moreover, recent imaging techniques have enabled us to observe simultaneously the motion and transcription of designated gene loci in living cells [125].

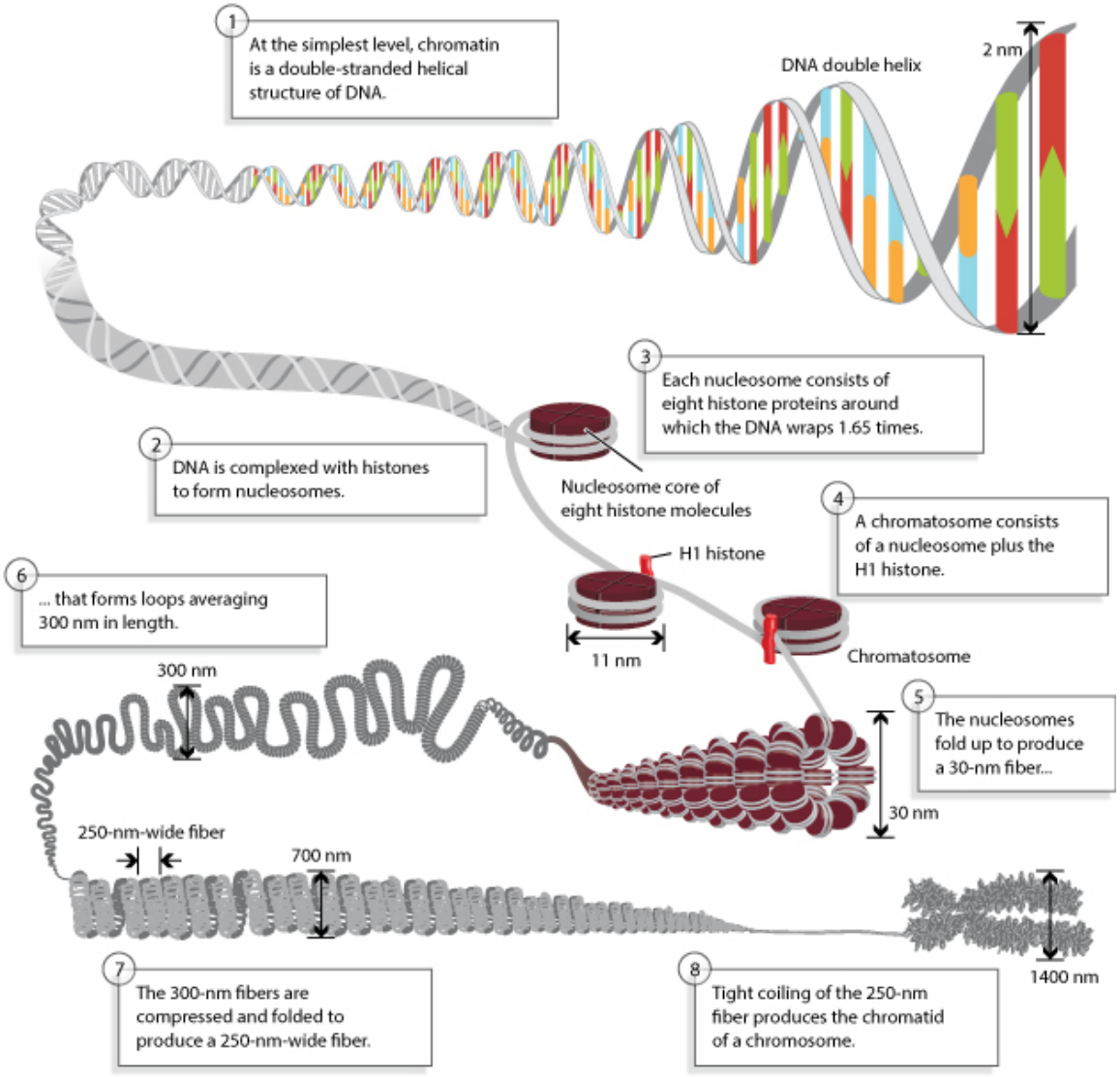


Figure 1.1: *A schematic of the folding of DNA on multiple scales. Image reprinted from* [8] *under the articles' terms of use; this image was in turn adapted from* [140].

1.3 Polymer Modelling

Over the past 70 years, there have been multiple attempts to dynamically model the movement of polymer chains with BD [15,90,160,161,203], which have more recently been used as a model for DNA filament dynamics [7].

The type of polymer model which we will be looking at are bead-spring models, where the continuous filament is modelled at a mesoscopic scale with beads connected by springs [7]. In more macroscopic models, these 'beads' are not representative of any physical entities (like nucleosomes), but instead are a tool for coarse-graining a filament. For example, in the case of modelling DNA, a bead may be placed every x base pairs (bp). The choice of x varies depending on the scale at which the model is applied, but can vary from hundreds to many millions of bp per bead. A discussion of the coarse-graining process for a polymer has been given by Underhill and Doyle [185]. There are other types of modelling approaches for a polymer, for example bead-rod models [7, 189], but these are outside the scope of this thesis.

One of the first and simplest bead-spring models was the Rouse model, developed in 1953 [161]. The only forces exerted on beads are Gaussian noise, Hookean spring forces from adjacent beads and viscous drag. One of the advantages of the simplicity of the model is that it is mathematically tractable, so many global properties can be derived in exact form [33], whilst also managing to agree with several properties of polymer chains from experiments [90, 151]. Generalizing this model to multiple resolutions is the focus of Chapter 2 of this thesis.

The first layer of complexity which is often added to the Rouse model is to introduce hydrodynamic forces between different beads, which occur when the movement of one bead creates a flow field which exerts forces on the other beads of the system [33, 203]. In most situations, this model is a more realistic modelling approach and has had success in modelling multiple application areas of polymer physics, for example modelling the relaxation of stretched DNA [137], stepping kinetics of

kinesin [202], dynamics for λ-phage DNA [77, 146, 167], polystyrene [5, 65] and modelling in confined geometries [149, 150].

There is a significant amount of mathematical analysis which has been to derive properties for the model with hydrodynamic interactions (HI). Much of the initial analysis of the single-scale model was done by Kirkwood and Riseman [82], who introduced elements of the BD model and gave an approximation to the translational diffusion coefficient which uses equilibrium averages for internal configurations. Following this, Zimm [203] found an approximation to the translational diffusion coefficient by pre-averaging the inter-particle distances in the hydrodynamic interaction tensor, known as the Zimm model. Öttinger [130] found a more accurate approximation equivalent to the previous work of Fixman [44] by considering the centre of hydrodynamic resistance and manipulating the diffusive displacement equation. In Chapter 3, we will look to expand this model to a multi-resolution model, by building on Öttinger's work [131] to obtain equations for the diffusion coefficient.

The original Rouse model and the model with HI both study what is known as a *theta solvent*, which is where the system lies at a temperature (known as the *theta temperature*) such that attraction and repulsion forces between beads along the chain effectively cancel each other out [131]. In most biologically realistic situations, we see that there is a net repulsive force between different areas of the polymer, which results in a *good solvent* and therefore the need to include excluded volume (EV) forces into the model [174], so that a pairwise repulsive force is included in the potential between pairs of either beads or springs. As an approach, significant amounts of analytical work has been carried out [33, 47, 49, 132] to provide an approximation for the *radius of gyration* of the polymer, which is a measure of the distance that a polymer lies from its centre of mass. This analytic work has then been extended to BD simulations using a soft-core Gaussian approach [92, 131, 135].

As we go into higher resolutions and include more realistic interactions, strands of

DNA can be modelled as smooth [7], unlike freely jointed chain (FJC) models where angles between beads are unconstrained. The wormlike chain model of Kratky and Porod [89], implemented via algorithm by Hagermann and Zimm [64], gives a non-uniform probability distribution for the angles between each bead, but done in such a way that closed form equations for intra-bead distances can be derived [64]. The advantage of including constraints for the angles between beads is that we introduce a notion of *persistence length* [7], which is a measure of the stiffness of the chain. This has been implemented using BD with HI [3, 94] to give bending as well as stretching forces.

There are also many further approaches to include more realistic potentials for forces between beads than the Hookean spring introduced in the Rouse model [54, 84, 159, 167], however many of these models lose mathematical tractability in forming analytic expressions of global properties as the polymer no longer resembles a Gaussian chain in equilibrium. An example of an improvement would be to model a finitely extensible nonlinear elastic (FENE) chain [16, 190], which is applicable in situations where underlying assumptions of the Rouse model are broken, in particular where the coarse-graining is sufficiently finely detailed such that the distance between adjacent beads represents only a few monomers, or in flow with high shear rates [191].

The previously discussed models still use a degree of coarse-graining to aggregate forces of long stretches of DNA into a bead-spring framework. If we wish to model on a more microscopic scale, there are BD models which look at individual histones and consider forces between these, for example in the model of Rosa and Everaers [159] which includes Lennard-Jones (LJ) and FENE forces between beads. Even more microscopic modelling includes the 3SPN (3-Sites-Per-Nucleotide) model of DNA [84], which uses three sites per nucleotide and can describe the more complicated dynamics found on these scales, however would be unwieldy if it were to be used on large domains, which creates the potential for hybrid models to be used to pair with this

model.

As we look at even more microscopic and detailed modelling, the BD assumption for a solvent and the model for the polymer acting on different temporal and spatial scales starts to beak down, so we need to explicitly model the solvent with a molecular dynamics (MD) approach. The key difference between the two approaches of MD and BD lies in how the surrounding solvent is modelled - in BD we aggregate solvent into a noise term in the equations of motion, while in atomistic MD we consider every atom of the system, including the solvent molecules, and calculate Newtonian forces between them [1, 99]. Although there is a rich field in improving algorithms [69, 98, 136, 186] for the quick calculation of forces in MD, available in a variety of software packages (for example Gromacs [13] and NAMD [139] are two of the more popular packages available), computationally this approach remains very costly, so systems studied are small - usually on the scale of nanometers or tens of nanometers [99].

In order to improve speeds, coarse-grained MD approaches have been created, which involves grouping together atoms and aggregating the forces and modelling dynamics with a Newtonian approach [99]. For example in DNA, coarse-grained MD can combine a nucleotide into one [175], or many sites [68]. This can be done from either a top-down approach, where different force contributions are chosen from intuition and parameters derived from experiment, or a bottom-up approach is taken, where parameters are derived from the underlying atomistic model [144]. A variety of structure-based coarse-grained models have been used for modelling chromatin [121, 144], for the interaction with transcription factors [180] as well as in nanotechnology, modelling the interaction between copolymers and lipid membranes [122]. Multiscale modelling techniques (e.g. [87] with iterative coarse-graining), as well as adaptive resolution models (e.g. [200] for solvent molecules), have been developed to connect all-atom models with coarse-grained approaches. A demonstration of the range of approaches available for modelling DNA to these microscopic levels is given in Figure 1.2.

Coarser BD models can also be estimated from MD models either analytically [37] or numerically [38], depending on the complexity of the MD model, which gives the potential for the development of hybrid models to be created between the two approaches.

An alternative approach to modelling of polymers with SDEs could be to consider the evolution for the probability distribution of the system using a partial differential equation known as the Fokker-Planck (FP) equation. Under certain assumptions [33, 131], the transition probability densities for the SDEs outlined in Section 1.1 are governed by an FP equation.

The FP approach has seen success in being used to model polymers on macroscopic scales, for example in polymer kinetic theory [107, 153]. However we choose to not tackle the modelling problem in this way as SDE models for the polymer can be more interpretable and amenable to developing simulation algorithms which are easily adaptable to situations like modelling protein binding in Section 2.3.

1.4 Multiscale Modelling

Most of the polymer models discussed in Section 1.3 consider the filament on only a single scale. In some applications, a modeller is interested in a relatively small region of a complex system. In these situations, it is often possible to use a hybrid model which is relatively accurate in the region of interest, and couple this with a model which is more computationally efficient in the rest of the simulated domain [37, 38, 46, 111]. It would be desirable when modelling a polymer using this kind of hybrid model that global properties of the system are maintained compared to a single-scale model, while bringing computational savings compared to the high resolution model.

This approach has become an increasingly popular technique in recent years as a method to look at complex models on larger spatial scales with more biologically

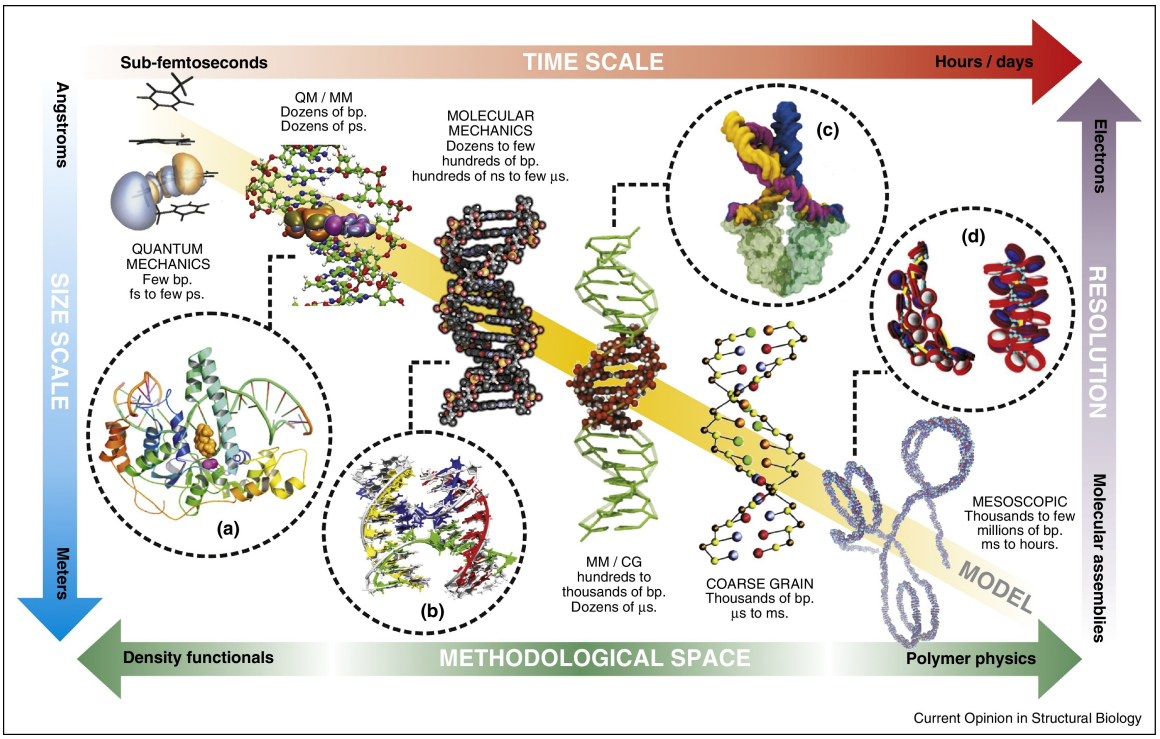


Figure 1.2: *A summary of different approaches to modelling* DNA *from microscopic to mesoscopic scales, varying in length-scale from a few bp of DNA to millions and in time from fs to hours. This image was reprinted from* [28] *with permission from* Elsevier. *Enclosed images (a)-(d) were adapted for the figure in* [28] *and have been reprinted here with permission. (a) shows a mixed Quantum Mechanics and Molecular Mechanics (QM/MM) model of* DNA [170] *which combines quantum approaches with MD. (b) gives a Holliday-junction simulated using MD* [75]. *(c) shows multi-scale modelling between MD and coarse-grained MD (CG) scales using the* SIRAH *forcefield* [112]. *(d) gives a mesoscopic Monte-Carlo model of chromatin fibre dynamics* [26].

relevant timescales [37, 38, 87, 178, 200]. This is useful, for example, in modelling the interaction between a DNA-binding protein and a DNA filament, where only the area near the protein needs to be modelled in high resolution and other areas can be modelled in a lower resolution, which is an application area which is explored in Chapter 2 of the thesis.

1.5 Physical Background to Nematic Liquid Crystals

In Chapter 4 of this thesis, we look at modelling NLC molecules in confined 2D systems.

We define a *crystal* to be a special type of solid where atoms lie in a periodic lattice which forms a regular array in 2D or 3D [169]. This gives a crystal a significant degree of regularity in the placement of atoms, with this periodic lattice repeating over relatively large distances.

The liquid crystal is a state which lies between that of a crystal and a liquid; with properties which share similarities with both. In the context of liquid crystals, there are two key differences between a liquid and a crystal [169]. Firstly, in a liquid atoms are equally likely to be in any position, while in a crystal atoms have an enhanced probability of being found in certain positions (i.e. at lattice sites), so we say a crystal possesses *positional order*. The other key difference is that in a liquid we are equally likely to find atoms oriented in any direction, while in a crystal atoms lie along special directions, so we say that the crystal has *orientational order*.

The liquid crystal is said to be a *mesophase* in that it lies between the two states of crystal and liquid by possessing partial order - it has orientational order but no positional order (or sometimes positional order but only in one or two dimensions.) This is possible as the molecules which make up a liquid crystal are not spherical,

instead they are long and thin with a preference to align with neighbours [179], which results in orientational order without positional order.

If we split molecules into a long axis and a short axis, we can define a *nematic liquid crystal* as a liquid crystal where the long axes of molecules tend to align along some preferred direction called the *anisotropic axis* [179]. There are other types of liquid crystal which possess different properties of ordering, for example cholesteric or smectic liquid crystals, but these are considered outside the scope of this thesis.

Liquid crystals were first discovered in 1888 by Friedrich Reinitzer [148] while investigating various derivatives of cholesteryl benzoate, where he discovered that two melting points existed from solid to cloudy liquid and from cloudy liquid to clear liquid [179]. In the years since liquid crystals have been witnessed in many natural systems [133], and are being used in a large range of application ranging from biomedical [147, 171] and material science applications [81, 133, 142], in an ever-growing field [56].

The most well-known and commercially successful application of liquid crystals has been in the development of LCDs (liquid crystal displays), which are found in modern television screens, as well as watches, calculators and other devices. This is due to their birefringence, which is the phenomenon of the level at which light refracts changes depending on polarization and propagation direction, as well as their tendency to align with electric fields [133]. The starting blocks of the science behind these devices was developed in the 1960's by RCA [192], before requiring many years of development before becoming commercially viable in television screens [21].

1.6 Modelling Nematic Liquid Crystals

In order to study NLC molecules it becomes important to have an order parameter, to quantify system behaviour, which can tell us the degree to which a system of

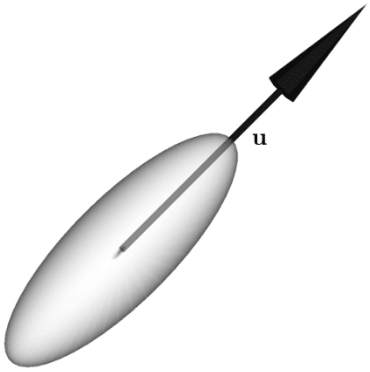


Figure 1.3: *The vector* $\mathbf{u}$ *gives the orientation of an NLC molecule. Figure made using* VTK [168].

molecules is in the nematic phase rather than the isotropic phase. Let the orientation of a particle be given by a vector $\mathbf{u}$, and the brackets $\langle * \rangle$ denote system average, then if we define the *tensor order parameter*, or Q-tensor, $\mathbf{Q}$ with components defined by

$$Q_{\alpha\beta} = \left\langle \frac{3}{2} u_\alpha u_\beta - \frac{1}{2}\delta_{\alpha\beta} \right\rangle, \tag{1.11}$$

this has several desirable properties [169] to differentiate between an isotropic and a nematic system. It is both symmetric and traceless, with $\mathbf{Q} = \mathbf{0}$ in the isotropic phase, and

$$\mathbf{Q} = \begin{pmatrix} -1/2 & 0 & 0 \\ 0 & -1/2 & 0 \\ 0 & 0 & 1 \end{pmatrix},$$

in the case of perfect nematic ordering about the z-axis.

If we instead consider partial nematic order of angle θ around the z-axis by giving each molecular orientation in spherical co-ordinates, so that $\mathbf{u} = (\sin\theta\cos\phi, \sin\theta\sin\phi,$

$\cos\theta$), then the Q-tensor has component [169]

$$Q_{zz} = \left\langle \frac{3}{2}\cos^2\theta - \frac{1}{2} \right\rangle = \langle P_2(\cos\theta)\rangle\,, \tag{1.12}$$

where $P_2(x) = 3x^2/2 - 1/2$ is the second Legendre polynomial. This average

$$S = \langle P_2(\cos\theta)\rangle \tag{1.13}$$

gives the *scalar order parameter* S of the nematic phase. To generalize to nematic order along some arbitrary axis $\mathbf{n}$, the Q-tensor is given by

$$Q_{\alpha\beta} = S\left(\frac{3}{2}n_\alpha n_\beta - \frac{1}{2}\delta_{\alpha\beta}\right), \tag{1.14}$$

for $S = \langle P_2(\cos\theta)\rangle$ and θ is the angle away from $\mathbf{n}$.

The interpretation for these order parameters is that S describes the magnitude of nematic order, and lies between 0 (isotropic phase) and 1 (perfect nematic phase) while the vector $\mathbf{n}$ describes the direction of the nematic order.

One of the first models for liquid crystals and their phase transition comes from Onsager [126] and provides a background for microscopic theory for the nematic state. We will give it a very brief overview here, an interested reader can find out more from other sources on the subject [126,169,188]. We assume that the liquid crystal is made up of hard rod particles, with length L and diameter d such that $L \gg d$, with no forces between them other than EV repulsion, so that the interaction potential U_{ij} between rods i and j is given by

$$U_{ij} = \begin{cases} 0 & \text{if no overlap;} \\ \infty & \text{if overlap.} \end{cases} \tag{1.15}$$

If a rod makes an angle θ with a second rod, then given the placement of the first

rod there is an EV area which cannot be occupied by the centre of mass of the second rod of size $2dL^2|\sin\theta|$ to first order [169], so that the volume excluded by the first rod is smallest when the rods are parallel and largest when they are perpendicular. As rods in the nematic state have a tendency to be parallel to each other, the number of allowed configurations of each additional rod is larger, which results in an increase in entropy and a decrease in free energy.

One usually expects entropy to favour disorder, but if we split the entropy into two contributions, positional and orientational entropy, then we see that positional entropy favours an isotropic state, while orientational entropy favours a nematic state to minimize EV contributions. In situations with high concentrations of molecules, the orientational entropy wins out and we find a nematic state, while in lower concentrations we see an isotropic state. It is possible to derive numerical relationships between the concentration and rod dimensions in this model, but this is outside the scope of this thesis, and given in [126, 169, 188].

It is also possible to study NLC molecules using a continuum approach, for which there exist three main theories [102,116]. The simplest continuum theory is the Oseen-Frank theory [48], which considers NLC molecules with a single preferred direction with a constant degree of orientational order. More general is the Ericksen theory [40], which still considers crystals with a single preferred direction, but now allows the level of orientational order to vary throughout the domain. These are both important theories to the development of theory behind liquid crystals [102], however they lie outside the scope of this thesis. The third main theory, and the most general, is Landau-de Gennes (LdG) theory [29], which we shall introduce, but for a more in-depth look a reader is pointed towards [29, 116].

Unlike the two previously mentioned theories, LdG theory can account for biaxial phases [116] by considering the state of a liquid with the Q-tensor discussed above. The basic concept of the theory is to construct free energy as a function of the Q-

tensor [169]. To take the most simple LdG approach, if we suppose that free energy f can be written as a power series of the terms of the Q-tensor, then it can be shown with the use of basic algebra that the system can be rewritten as a power series in the scalar order parameter S of the form

$$f = f_0 + \frac{a}{2}S^2 + \frac{b}{3}S^3 + \frac{c}{4}S^4 + \dots, \tag{1.16}$$

where f_0, a, b and c are constants. We suppose a, b and c are smooth functions of the temperature of the system. If this power series is truncated at 4^{th} order, this forces $c > 0$ so that free energy does not go to $-\infty$ as S becomes large. We also suppose $b > 0$ to ensure the system is physically realistic, a decision which is explained in [169].

We study the behaviour of f as we vary a with b and c held constant. By considering $\partial f/\partial S = 0$, we see for values of $a > 2b^2/9c$ the global free-energy minimum is at $S > 0$ and for $a < 2b^2/9c$ it occurs at $S = 0$. This suggests as the temperature of the system increases through some threshold, we get a phase transition from the isotropic $S = 0$ state to the nematic $S > 0$ state. This is a brief introduction to the flavour of LdG theory, but there is a significantly larger field of study which looks at areas like functional analysis looking at areas of validity of the theory [115], as well as investigating other aspects of the Q-tensor [120].

In addition to the above continuum approaches to modelling NLC molecules, there are also discrete approaches; either microscopic models considering each liquid crystal molecule [2, 50] in a domain, or looking at clusters of molecules based at lattice sites [25,96]. The original on-lattice approach is the Lebwohl-Lasher model [96], which places long rods at on-lattice sites and considers pairwise interactions between neighbouring particles and finds phase transitions as a function of neighbouring particles' interaction energy.

One of the most used discrete approaches is the Gay-Berne (GB) model [50], an

Model	Type	Brief Description
Onsager [126]	Discrete	Models an NLC as a cylindrical rod and studies entropy contributions
Oseen-Frank [48]	Continuum	A NLC has a single preferred direction and constant degree of orientational order
Ericksen [40]	Continuum	A NLC has a single preferred direction and variable degree of orientational order
Landau-de Gennes [29]	Continuum	Accounts for biaxial phases and variable degree of orientational order for an NLC
Lebwohl-Lasher [96]	Discrete	On-lattice model
Gay-Berne [50]	Discrete	Off-lattice model for ellipsoidal NLC molecules

Table 1.1: *A brief summary of liquid crystal models discussed in the Introduction.*

off-lattice microscopic approach to modelling liquid crystals which is the model we use for calculations in Chapter 4. A precise mathematical definition of the model is given in Chapter 4, but we shall seek to give a brief introduction here. The GB model seeks to give a realistic potential acting between two ellipsoidal particles based upon the well-known LJ potential [79]. The weakness of using a pure LJ potential for NLC molecules comes from the ellipsoidal shape which would require multiple sites in each molecule to be considered to get accurate results, significantly increasing computational time. Therefore, a modified potential is derived, using an overlap shape parameter [14] which gives an approximate separation of ellipsoidal particles, as well as a new strength parameter which gives a correct ratio between energies at different orientations of two particles [50]. This potential has been shown to accurately depict behaviour between liquid crystals [11] and despite the original paper being published 27 years ago, it continues to be used in many studies today, for example [128,156,197].

A summary of all models discussed in the Section 1.6 is given in Table 1.1.

1.7 Confined Systems of Nematic Liquid Crystals

The particular system that we are looking at is concerned with modelling of severely confined systems of liquid crystals, which have applications in zenithal bistable devices [78]. These are similar to LCD screens, but with pixels on screen which only require power to change between two stable states [177], so that no power is required to hold an image, only to change the image shown. This means they can show images for several years, changing up to ten times per day, with only a single small battery [78]. They work by forming one of two stable states (twisted or hybrid aligned) for an arrangement of liquid crystals, which can then be seen as white or black when viewed between crossed polarizers [177].

In order to inform and validate modelling of confined systems of liquid crystals, experimentalists have been informing directions to be followed by modellers. This is interesting for applications to confined systems, as although continuum theories have shown their use in larger systems, it is not clear whether they hold for severely confined systems [156]. One key study of interest is looking at shallow square wells filled with NLC molecules by Tsakonas et al. [184], designed in such a way to get the NLC molecules forming in two dimensions. They managed to find two equilibria for a diagonal and a rotated solution, which agreed with LdG theory, shown in Figure 1.4. This has been followed up to find the same equilibria using Oseen-Frank theory and experiments on viruses in rectangular confined systems [100].

Other theoretical approaches have been made to study the confined systems problem. Luo et al. [110] found a bifurcation for the rotated solution as a function of the behaviour of anchoring, which suggested that the diagonal solution is more pervasive than the rotated solution. A new third solution, the well-order reconstruction solution (WORS) was found by Kralj and Majumdar [88] from a 3D LdG model under certain conditions for the size of the well, the material and the temperature. This was investigated further by Robinson et al. [156], who used discrete on- and off-lattice

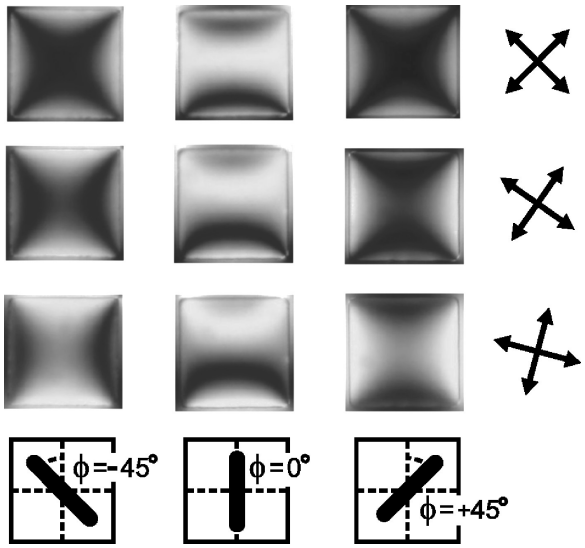


Figure 1.4: *Steady states of* NLC *molecules forming between crossed polarizers in confined square wells. Different rows show different rotations of the polarizers. Columns give different directions for the nematic director, ranging from one diagonal, to vertical, to the other diagonal. Reprinted from* [184]*, with the permission of* AIP Publishing.

approaches to model the wells, on top of the continuum LdG model in 2D, to study these stationary solutions. The off-lattice GB approaches only managed to find the diagonal solution, the on-lattice Lebwohl-Lasher approach found both diagonal and rotated solutions while the LdG modelling found the WORS solution as well as the diagonal and rotated solutions.

The LdG approach used by Robinson et al. [156] is to use Q-tensor theory in two dimensions to describe the state of the system. As it is both symmetric and traceless, in two dimensions the Q-tensor can be written as

$$\mathbf{Q} = \begin{pmatrix} Q_{11} & Q_{12} \\ \\ Q_{12} & -Q_{11} \end{pmatrix}, \tag{1.17}$$

and can be considered as a modified Ericksen approach [156]. Therefore the system can be fully described by director $\mathbf{n}$ and order parameter S. The LdG approach in

this context is a variational theory to look at equilibria under minimizers of some defined LdG energy [156, 187]. In their paper, Robinson et al. [156] define an LdG energy density [110], as the sum of an elastic energy density and a bulk potential. This gives local minimizers as solutions of the corresponding weak formulation. Distinct initial fields are introduced to solve these equations using a finite element methods package [4]. Under different parameter regimes, the diagonal, rotated and WORS solutions were found. This process is studied in more detail in Section 4.1.5.

1.8 Structure of this thesis

The novel research completed over the course of this DPhil is given in Chapters 2, 3 and 4 of this thesis; while Chapter 5 is a discussion of the work contained within.

The contents of Chapter 2 is based on my research paper [158] published in Multiscale Modelling and Simulation in 2017, with co-authors Radek Erban and Yuichi Togashi. In this chapter I introduce the multi-resolution Rouse model for a polymer and derive some results for statistics of the chain. This allows scaling laws to be found in order to create chains which maintain desired statistics. A BD technique is given to simulate the system, which is applied to a model for the binding of a protein to a DNA filament.

This work is extended to include HI in Chapter 3, which is based on the work from my second research paper [157] published in the Journal of Chemical Physics in 2018 with Radek Erban as co-author. In this chapter I begin by extending the static Gaussian chain (GC) model for a polymer into a multi-resolution framework. This forms the basis for a dynamical model for a polymer with HI included in the mobility tensor. Analytic approximations using the pre-averaging approximation and then the long chain limit for the diffusion of a chain are derived, which gives scaling laws for the construction of a polymer. This polymer is then modelled using BD by

extending the Ermak-McCammon algorithm [41], in order to compare statistics of the chain between analytic approximation and simulations.

The work in Chapter 4 looks at NLC molecules in a two-dimensional domain, considering steady-state behaviour with BD modelling undertaken in collaboration with Apala Majumdar. I begin by introducing our approach, which combines a BD approach with Dirichlet boundary conditions and a novel approach to generating initial conditions. This chapter is primarily looking at nematic equilibria suggested continuum LdG modelling, in particular through two research questions. Firstly, I look at starting a system with NLC molecules in random configurations and simulating to try and find the nematic equilibria forming in different parameter regimes. Then I look at beginning the system in the nematic equilibria and looking at whether this state is retained or lost as the temperature of the system increases.

Chapter 2

Varying the resolution of the Rouse model on temporal and spatial scales: application to multiscale modelling of DNA dynamics

The work from this chapter has been adapted from my first paper which was published in Multiscale Modelling and Simulation [158] in collaboration with Yuichi Togashi, which is work from the first year of my DPhil. The main differences between this work and the paper are that notation has been changed in order to be uniform with the work in the Chapter 3, and the introduction of the paper has been partly merged into Chapter 1 of this thesis.

The work in this chapter is primarily looking at developing a multi-resolution bead-spring model for polymer dynamics as a generalization of the Rouse model. I describe a polymer chain as beads of variable sizes connected by springs with variable spring constants. This leads to a numerical scheme which can use different timesteps to advance the positions of different beads to extend the Rouse model to a

multi-resolution model on both spatial and temporal scales. This allows simulations of localized regions of a polymer chain with high spatial and temporal resolution, while using a coarser modelling approach to describe the rest of the polymer chain. A method for changing the model resolution on-the-fly is also developed using the Metropolis-Hastings algorithm. It is shown that this multi-resolution bead-spring model maintains key global statistics of the end-to-end distance and diffusion of the polymer filament and makes computational savings when applied to a model for the binding of a protein to the DNA filament.

In this chapter I use the Rouse model as a starting point due to its mathematical tractability and small computational load. Such a model is applicable to modelling DNA dynamics for relatively macroscopic resolutions below the level of the entire chromosome, where hydrodynamic forces (discussed further in Chapter 3) are negligible and the experimental value for the persistence length of DNA [63] is significantly shorter than the Kuhn length of the model. Although the Rouse model has previously been used to explain properties of λ-phage DNA [73, 74], it is not intended in this thesis to be used to reproduce detailed DNA phenomena, for example chromosome organization, but instead to act as a simple coarse model which operates at low resolutions. It is hoped that through future work this could be combined with other models at finer levels of detail.

When taking this multiscale approach, it is necessary to understand the error from including the less accurate model in the hybrid model and how the accuracy of the method depends on its parameters, as well as the effect of coupling two models operating on different resolutions on the global statistics of the polymer. These are the main questions studied in this chapter.

This chapter is organized as follows. In Section 2.1, I introduce a multi-resolution bead-spring model which generalizes the Rouse model. I also introduce a discretized version of this model which enables the use of different timesteps in different spatial

regions. In Section 2.2, I analyze the main properties of the multi-resolution bead-spring model. I prove two lemmas giving formulas for the diffusion constant and the end-to-end distance. I also study the appropriate choice of timesteps for numerical simulations of the model and support my analysis with the results of illustrative computer simulations. The main application area is studied in Section 2.3 where I present and analyze a DNA binding model. I develop a method to increase the resolution in existing segments on-the-fly using the Metropolis-Hastings algorithm. In Section 2.4, I conclude this chapter by discussing possible extensions of the presented multi-resolution approach by including more detailed models of DNA dynamics and other multiscale methods developed in the literature, as well as recent developments in experimentally measuring properties of DNA.

2.1 Multi-resolution bead-spring model

We generalize the classical Rouse bead-spring polymer model [161] to include beads of variable sizes[1] and springs with variable spring constants. In Definition 2.1, we formulate the evolution equation for this model as a system of SDEs. We will also introduce a discretized version of this model in Algorithm 2.1, which will be used in Sections 2.2 and 2.3 where we use the multi-resolution bead-spring model to develop and analyze multiscale models for DNA dynamics.

Definition 2.1 *Let $N > 1$ be a positive integer. A multi-resolution bead-spring polymer of size N consists of a chain of N beads of radius σ_n, for $n = 1, 2, \ldots, N$, connected by $N - 1$ springs which are characterized by their spring constants k_n, for $n = 1, 2, \ldots, N - 1$. The positions $\mathbf{r}_n \equiv \mathbf{r}_n(t) = [r_{n,1}(t), r_{n,2}(t), r_{n,3}(t)]$ of beads evolve*

[1]The bead radius in the classical Rouse model or in Definition 2.1 is used as a parameter of the model to ensure global properties remain consistent as shall be shown later in Lemma 2.2 and Lemma 2.3, but it does not have any physical meaning for EV or similar interactions.

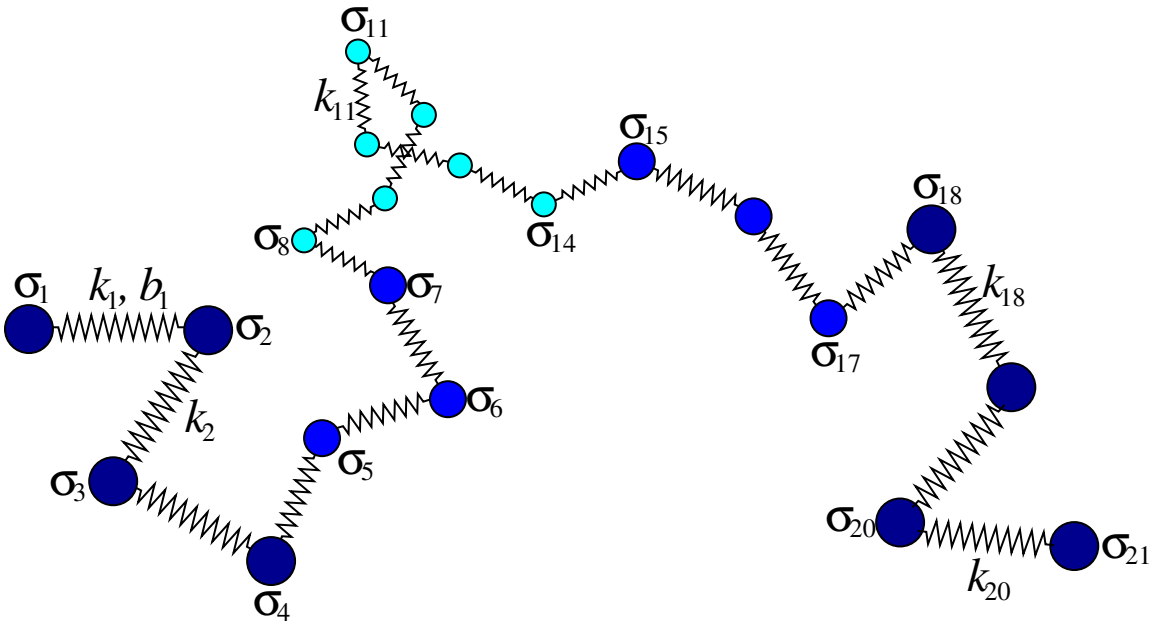


Figure 2.1: *A schematic of the multi-resolution bead-spring model for* $N = 21$.

according to the system of SDEs (for $n = 1, 2, \ldots, N$*)*

$$\zeta_n \, \mathrm{d}\mathbf{r}_n = \Big(k_{n-1}\mathbf{r}_{n-1}(t) - (k_{n-1} + k_n)\mathbf{r}_n(t) + k_n \mathbf{r}_{n+1}(t) \Big) \, \mathrm{d}t + \sqrt{2k_B T \zeta_n} \, \mathrm{d}\mathbf{W}_n, \quad (2.1)$$

where $\zeta_n = 6\pi\eta\sigma_n$ *is the frictional drag coefficient of the* n^{th} *bead given by Stokes' theorem,* η *is the solvent viscosity,* $\mathrm{d}\mathbf{W}_n \equiv [\mathrm{d}W_{n,1}, \mathrm{d}W_{n,2}, \mathrm{d}W_{n,3}]$ *is a Wiener process,* T *is absolute temperature,* k_B *is the Boltzmann constant and we assume that each spring constant* k_n *can be equivalently expressed in terms of the corresponding Kuhn length* b_n *by*

$$k_n = \frac{3k_B T}{b_n^2}, \qquad \textit{for} \quad n = 1, 2, \ldots, N-1,$$

to give a Hookean spring force. We assume that the behaviour of boundary beads (for $n = 1$ *and* $n = N$*) is also given by equation* (2.1) *simplified by postulating* $\mathbf{r}_0(t) = \mathbf{r}_1(t)$ *and* $\mathbf{r}_{N+1}(t) = \mathbf{r}_N(t)$.

In Figure 2.1, we schematically illustrate a multi-resolution bead-spring polymer for $N = 21$. The region between the 8-th and the 14-th bead is described with

the highest resolution by considering smaller beads and springs with larger spring constants (or equivalently with smaller Kuhn lengths).

The scalings of different parameters in Definition 2.1 are chosen so that we recover the classical Rouse model [161] if we assume $\sigma_1 = \sigma_2 = \cdots = \sigma_N = \sigma$ and $b_1 = b_2 = \cdots = b_{N-1} = b$. Then equation (2.1) simplifies to

$$\zeta \, \mathrm{d}\mathbf{r}_n = k \Big(\mathbf{r}_{n-1}(t) - 2\mathbf{r}_n(t) + \mathbf{r}_{n+1}(t) \Big) \, \mathrm{d}t + \sqrt{2k_B T \zeta} \, \mathrm{d}\mathbf{W}_n, \tag{2.2}$$

where $\zeta = 6\pi\eta\sigma$, $k = 3k_BT/b^2$ and we again define $\mathbf{r}_0(t) = \mathbf{r}_1(t)$ and $\mathbf{r}_{N+1}(t) = \mathbf{r}_N(t)$ in equations for boundary beads. In the polymer physics literature [33], the Rouse model (2.2) is equivalently written as

$$\zeta \frac{d\mathbf{r}_n}{dt}(t) = k \Big(\mathbf{r}_{n-1}(t) - 2\mathbf{r}_n(t) + \mathbf{r}_{n+1}(t) \Big) + \mathbf{f}_n(t), \tag{2.3}$$

where random thermal noises $\mathbf{f}_n(t)$ exerted on the beads from Brownian motion are characterized by the moments [33]

$$\langle \mathbf{f}_n(t) \rangle = \mathbf{0}, \qquad \langle f_{n,\alpha}(t) f_{m,\beta}(t') \rangle = 2\zeta k_B T \delta_{nm} \delta_{\alpha\beta} \delta(t - t'), \tag{2.4}$$

where $n, m = 1, 2, \ldots, N$ and $\alpha, \beta \in \{1, 2, 3\}$ and we define the functions

$$\delta_{nm} = \begin{cases} 1, & \text{for } n = m; \\ 0, & \text{otherwise,} \end{cases} \qquad \text{and} \quad \delta(x) = \begin{cases} 1, & \text{for } x = 0; \\ 0, & \text{otherwise.} \end{cases} \tag{2.5}$$

For the remainder of this chapter, we will use the SDE notation as given in (2.2), because we will often study numerical schemes for simulating polymer dynamics models. The simplest discretization of (2.2) is given by the Euler-Maruyama (EM) method [83], which uses the finite timestep Δt and calculates the position vector $\mathbf{r}_n^t$

of the n^{th} bead, $n = 1, 2, \ldots, N$; at discretized time $t = i\Delta t$, for $i = 0, 1, \ldots$ with

$$\mathbf{r}_n^{t+\Delta t} = \mathbf{r}_n^t + \frac{k}{\zeta}\left(\mathbf{r}_{n-1}^t - 2\,\mathbf{r}_n^t + \mathbf{r}_{n+1}^t\right)\Delta t + \sqrt{\frac{2k_BT}{\zeta}\Delta t}\;\boldsymbol{\xi}_n^t \tag{2.6}$$

for $\boldsymbol{\xi}_n^t = (\xi_{n,1}^t, \xi_{n,2}^t, \xi_{n,3}^t)$, where $\xi_{n,\alpha}^t$ is a normally distributed random variable with zero mean and unit variance (i.e. $\xi_{n,\alpha}^t \sim \mathcal{N}(0,1)$) for $\alpha = 1, 2, 3$. Other more complex integration schemes exist for BD models of polymers, which perform better than the EM integration scheme (2.6) in error bound and stability, and could be used with the presented multi-resolution methodology to design higher order methods [83, 176], but we use EM for simplicity and as a proof-of-concept. In order to discretize the multi-resolution bead-spring model, we allow for variable timesteps with the following definition.

Definition 2.2 *Let $\Delta t > 0$ and let j_n, $n = 1, 2, \ldots, N-1$, be positive integers such that $j_{n-1} \mid j_n$ or $j_n \mid j_{n-1}$ for $n = 2, 3, \ldots, N-1$. We use the divisibility symbol $a \mid b$ if there exists an integer n such that $an = b$, and the symbol $a \nmid b$ where no such integer n exists. Let us assume that at least one of the values of j_n is equal to 1. We define $\Delta t_n = j_n \Delta t$ for $n = 1, 2, \ldots, N-1$ and we call Δt_n a timestep associated with the n^{th} spring.*

Definition 2.2 specifies that all timesteps must be integer multiples of the smallest timestep Δt. The timesteps associated with two adjacent springs are also multiples of each other. The time evolution of the multi-resolution bead-spring model is computed at integer multiples of Δt. One iteration of the algorithm is shown in Algorithm 2.1. The position of the n^{th} bead is updated at integer multiples of $\min\{j_{n-1}, j_n\}\Delta t = \min\{\Delta t_{n-1}, \Delta t_n\}$ by calculating the random displacement due to Brownian motion, with displacement caused by springs attached to the bead also updated at integer multiples of the timesteps associated with each spring, i.e. Δt_{n-1} or Δt_n. Considering

the situation that all beads, springs and timesteps are the same, then one can easily deduce the following result.

Lemma 2.1 *Let $\sigma > 0$, $\zeta > 0$, $k > 0$ and $\Delta t > 0$ be positive constants and $N > 1$ be an integer. Consider a multi-resolution bead-spring polymer of size N with $\sigma_n = \sigma$, $\zeta_n = \zeta$, for $n = 1, 2, \ldots, N$, and $k_n = k$, for $n = 1, 2, \ldots, N-1$. Let the timesteps associated with each spring be equal to Δt, i.e. $j_1 = j_2 = \cdots = j_n = 1$ in Definition* 2.2. *Then Algorithm* 2.1 *is equivalent to the EM discretization of the Rouse model given as equation* (2.6).

Lemma 2.1 shows that the multi-resolution bead-spring model is a generalization of the Rouse model. In the next section, we will study properties of this model which will help us to select the appropriate parameter values for this model and use it in multiscale simulations of DNA dynamics.

2.2 Macroscopic properties and parameterizations of multi-resolution bead-spring models

We have formulated a multi-resolution Rouse model which varies the bead radii and Kuhn lengths throughout the filament, but we would like to keep statistics of the overall filament constant regardless of the resolution regime being considered for the filament. We consider a global statistic for the system to be *consistent* if the expected value of the statistic is invariant to the resolution regime being considered for the filament. We consider the *translational diffusion coefficient* defined in (2.7) and *root mean squared (rms) end-to-end distance* defined in (2.15) as two statistics we wish to be consistent in our system, which can be ensured by varying the bead radius and the number of beads respectively. The precise way to vary these properties will be explored in this section.

Update positions of internal beads which are connected to two springs:

for $n = 2, 3, \ldots, N-1$ **do**

  if $\min\{j_{n-1}, j_n\} \mid (i+1)$ **then**

    Put $\mathbf{r}_n^{(i+1)\Delta t} := \mathbf{r}_n^{i\Delta t} + \sqrt{\dfrac{2k_BT}{\zeta_n}\min\{j_{n-1}, j_n\}\Delta t}\,\boldsymbol{\xi}_n^i$ where $\boldsymbol{\xi}_n^i$ is a vector of random numbers sampled from $\boldsymbol{\xi}_n^i \sim [\mathcal{N}(0,1), \mathcal{N}(0,1), \mathcal{N}(0,1)]$.

    if $j_{n-1} \mid (i+1)$ **then**

      Put $\mathbf{r}_n^{(i+1)\Delta t} := \mathbf{r}_n^{(i+1)\Delta t} + \dfrac{k_{n-1}}{\zeta_n}\left(\mathbf{r}_{n-1}^{(i+1-j_{n-1})\Delta t} - \mathbf{r}_n^{(i+1-j_{n-1})\Delta t}\right)\Delta t_{n-1}$.

    end

    if $j_n \mid (i+1)$ **then**

      Put $\mathbf{r}_n^{(i+1)\Delta t} := \mathbf{r}_n^{(i+1)\Delta t} + \dfrac{k_n}{\zeta_n}\left(\mathbf{r}_{n+1}^{(i+1-j_n)\Delta t} - \mathbf{r}_n^{(i+1-j_n)\Delta t}\right)\Delta t_n$.

    end

  else

    Put $\mathbf{r}_n^{(i+1)\Delta t} := \mathbf{r}_n^{i\Delta t}$.

  end

end

Update of the first bead:

if $j_1 \mid (i+1)$ **then**

  Put $\mathbf{r}_1^{(i+1)\Delta t} := \mathbf{r}_1^{i\Delta t} + \dfrac{k_1}{\zeta_1}\left(\mathbf{r}_2^{(i+1-j_1)\Delta t} - \mathbf{r}_1^{(i+1-j_1)\Delta t}\right)\Delta t_1 + \sqrt{\dfrac{2k_BT}{\zeta_1}\Delta t_1}\,\boldsymbol{\xi}_1^i$ where $\boldsymbol{\xi}_1^i \sim [\mathcal{N}(0,1), \mathcal{N}(0,1), \mathcal{N}(0,1)]$.

else

  Put $\mathbf{r}_1^{(i+1)\Delta t} := \mathbf{r}_1^{i\Delta t}$.

end

Update of the last bead:

if $j_{N-1} \mid (i+1)$ **then**

  Put $\mathbf{r}_N^{(i+1)\Delta t} := \mathbf{r}_N^{i\Delta t} + \dfrac{k_{N-1}}{\zeta_N}\left(\mathbf{r}_{N-1}^{(i+1-j_{N-1})\Delta t} - \mathbf{r}_N^{(i+1-j_{N-1})\Delta t}\right)\Delta t_{N-1}$
  $+ \sqrt{\dfrac{2k_BT}{\zeta_N}\Delta t_{N-1}}\,\boldsymbol{\xi}_N^i$ where $\boldsymbol{\xi}_N^i \sim [\mathcal{N}(0,1), \mathcal{N}(0,1), \mathcal{N}(0,1)]$.

else

  Put $\mathbf{r}_N^{(i+1)\Delta t} := \mathbf{r}_N^{i\Delta t}$.

end

Algorithm 2.1: *One iteration of the numerical algorithm for simulating the multi-resolution bead-spring model introduced in Definition* 2.1. *We update positions of beads at time* $t = i\Delta t$ *where* i *is a positive integer and each spring is simulated using its associated timestep given in Definition* 2.2.

2.2.1 Translational diffusion coefficient

The *translational diffusion coefficient* is defined as

$$D_G = \lim_{t\to\infty} \frac{1}{6t} \left\langle (\mathbf{r}_G^t - \mathbf{r}_G^0)^2 \right\rangle = \lim_{t\to\infty} \frac{1}{6t} \sum_{i=1}^{3} \left\langle (r_{G,i}^t - r_{G,i}^0)^2 \right\rangle, \tag{2.7}$$

where $\mathbf{r}_G^t$ is the *centre of mass* of the polymer chain at time t, which is defined by

$$\mathbf{r}_G^t = \frac{1}{\Omega} \sum_{n=1}^{N} \sigma_n \mathbf{r}_n^t, \qquad \text{where} \qquad \Omega = \sum_{n=1}^{N} \sigma_n. \tag{2.8}$$

Definition (2.8) is an extension to the definition given by Doi and Edwards [33] for the centre of mass of a continuous chain on only one scale. If all beads have the same radius σ (i.e. if $\sigma_n = \sigma$ for $n = 1, 2, \ldots, N$), then equation (2.8) simplifies to the centre of mass definition for the classical Rouse model. In this case, the translational diffusion coefficient is given by [33]

$$D_G = \frac{k_B T}{6\pi\eta\sigma N}, \tag{2.9}$$

where N is the number of beads. This result explains the, on the face of it, counter-intuitive scaling of equation (2.8) with σ_n. If we suppose that each bead had the same density, then the mass of each bead would be proportional to its volume, i.e. to σ_n^3. However, in the definition (2.8), we have used weights σ_n instead of σ_n^3, because, as discussed in Section 1.3, beads do not represent physical bead objects like nucleosomes, but representations of the filament around it, so the 'bead radius' is an arbitrary value which is chosen in this case to ensure that $\Omega = \sigma N$ in the single-scale model.

This linear scaling with σ_n can also be confirmed using (2.9) for the classical Rouse model. If we describe the same polymer using a more detailed model consisting of twice as many beads (i.e. if we change N to $2N$), then we have to halve the bead radius

(i.e. change σ to $\sigma/2$) to get a polymer model with the same diffusion constant (2.9). In particular, the mass of a bead scales with σ (and not with σ^3). In the next lemma, we extend result (2.9) to a general multi-resolution bead-spring model.

Lemma 2.2 *Let us consider a multi-resolution bead-spring polymer of size N and a set of timesteps associated with each spring satisfying the assumptions of Definitions* 2.1 *and* 2.2*. Then the translational diffusion coefficient of the polymer evolution described by Algorithm* 2.1 *is given by*

$$D_G = \frac{k_B T}{6\pi\eta\,\Omega}. \tag{2.10}$$

Proof. Algorithm 2.1 describes one iteration of our numerical scheme. Multiplying the steps corresponding to the n^{th} bead by σ_n and summing over all beads, we obtain how $\Omega\,\mathbf{r}_G^{i\Delta t}$ changes during one timestep Δt. Since $\zeta_n = 6\pi\eta\sigma_n$, tension terms cancel after summation and the evolution rule for $\Omega\,\mathbf{r}_G^{i\Delta t}$ simplifies to

$$\begin{aligned}
\Omega\,\mathbf{r}_G^{(i+1)\Delta t} &= \Omega\,\mathbf{r}_G^{i\Delta t} + Q(j_1, i+1)\sqrt{\frac{k_B T\sigma_1}{3\pi\eta}\Delta t_1}\,\boldsymbol{\xi}_1^i \\
&+ Q(j_{N-1}, i+1)\sqrt{\frac{k_B T\sigma_N}{3\pi\eta}\Delta t_{N-1}}\,\boldsymbol{\xi}_N^i \\
&+ \sum_{n=2}^{N-1} Q(\min\{j_{n-1}, j_n\}, i+1)\sqrt{\frac{k_B T\sigma_n}{3\pi\eta}\min\{j_{n-1}, j_n\}\Delta t}\,\boldsymbol{\xi}_n^i,
\end{aligned} \tag{2.11}$$

where $\boldsymbol{\xi}_n^i \sim [\mathcal{N}(0,1), \mathcal{N}(0,1), \mathcal{N}(0,1)]$ and function $Q(j,i)$ is defined for positive integers j and i by

$$Q(j,i) = \begin{cases} 1, & \text{if } j \mid i; \\ 0, & \text{if } j \nmid i. \end{cases} \tag{2.12}$$

Let us denote by L the least common multiple of $\{j_1, j_2, \ldots, j_n\}$. Every bead is updated in Algorithm 2.1 at integer multiples of $L\Delta t$. We can eliminate function Q

from equation (2.11) if we consider the evolution of $\Omega\,\mathbf{r}_G^t$ when time t is evaluated at integer multiples of $L\Delta t$. We obtain the evolution rule

$$\Omega\,\mathbf{r}_G^{(i+1)L\Delta t} = \Omega\,\mathbf{r}_G^{iL\Delta t} + \sqrt{\frac{k_B T\Omega}{3\pi\eta} L\Delta t}\,\boldsymbol{\xi}, \tag{2.13}$$

for $\boldsymbol{\xi} \sim [\mathcal{N}(0,1), \mathcal{N}(0,1), \mathcal{N}(0,1)]$, where we used the fact that the sum of normally distributed random variables is again normally distributed. Dividing equation (2.13) by Ω, we obtain

$$\mathbf{r}_G^{iL\Delta t} = \mathbf{r}_G^0 + \sqrt{\frac{k_B T}{3\pi\eta\,\Omega} iL\Delta t}\,\boldsymbol{\xi}, \qquad \text{for} \quad \boldsymbol{\xi} \sim [\mathcal{N}(0,1), \mathcal{N}(0,1), \mathcal{N}(0,1)]. \tag{2.14}$$

Using definition (2.7), we obtain (2.10). □

The formula (2.10) is a generalization of equation (2.9) obtained for the Rouse model. It is invariant to the resolution scheme for the polymer provided that the mass of the filament Ω remains constant through selection of the number of beads and bead radius. The translational diffusion coefficient is therefore consistent.

2.2.2 End-to-end distance

We define the *end-to-end vector* $\mathbf{R} = \mathbf{r}_N - \mathbf{r}_1$ from one end of the filament to the other [33]. An important statistic to consider related to this is the *rms end-to-end distance* of the filament

$$\mu = \langle \mathbf{R}^2 \rangle^{1/2}. \tag{2.15}$$

The expected value of the long-time limit of the rms end-to-end distance, denoted μ_∞, for the classical Rouse model is given by [33]

$$\mu_\infty = \lim_{t\to\infty} \langle \mathbf{R}^2 \rangle^{1/2} = b\sqrt{N-1}. \tag{2.16}$$

We generalize this result in the following lemma.

Lemma 2.3 *Let us consider a multi-resolution bead-spring polymer of size N satisfying the assumptions of Definition* 2.1*. Then*

$$\lim_{t\to\infty}\langle(\mathbf{r}_{n+1}(t)-\mathbf{r}_n(t))^2\rangle = b_n^2, \qquad \textit{for} \quad n=1,2,3,\ldots,N-1, \tag{2.17}$$

and the long-time limit of the rms end-to-end distance is given by

$$\mu_\infty = \lim_{t\to\infty}\langle\mathbf{R}^2\rangle^{1/2} = \sqrt{\sum_{n=1}^{N-1} b_n^2}. \tag{2.18}$$

Proof. Equations (2.1) describe a system of $3N$ linear SDEs. However, the SDEs corresponding to different spatial dimensions are not coupled. We therefore restrict our investigation to the behaviour of the first coordinates of each vector in (2.17). Let us arrange the differences of the first coordinates of subsequent beads into the $(N-1)$-dimensional vector

$$\mathbf{y}(t) = [r_{2,1}(t)-r_{1,1}(t), r_{3,1}(t)-r_{2,1}(t), r_{4,1}(t)-r_{3,1}(t), \ldots, r_{N,1}(t)-r_{N-1,1}(t)]^{\mathrm{T}}.$$

Then SDEs (2.1) can be rewritten to the system of SDEs for $\mathbf{y}(t)$ in the matrix form $\mathrm{d}\mathbf{y} = \mathbf{A}\,\mathbf{y}\,\mathrm{d}t + \mathbf{B}\,\mathrm{d}\mathbf{W}$, where $\mathbf{A}\in\mathbb{R}^{(N-1)\times(N-1)}$ is a three-diagonal matrix given by

$$\mathbf{A} = \begin{pmatrix} -\left(\frac{k_1}{\zeta_1}+\frac{k_1}{\zeta_2}\right) & \frac{k_2}{\zeta_2} & 0 & 0 & \dots & 0 \\ \frac{k_1}{\zeta_2} & -\left(\frac{k_2}{\zeta_2}+\frac{k_2}{\zeta_3}\right) & \frac{k_3}{\zeta_3} & 0 & \dots & 0 \\ 0 & \frac{k_2}{\zeta_3} & -\left(\frac{k_3}{\zeta_3}+\frac{k_3}{\zeta_4}\right) & \frac{k_4}{\zeta_4} & \dots & 0 \\ \vdots & \vdots & \vdots & \vdots & \ddots & \vdots \\ 0 & 0 & 0 & 0 & \dots & -\left(\frac{k_{N-1}}{\zeta_{N-1}}+\frac{k_{N-1}}{\zeta_N}\right) \end{pmatrix},$$

$\mathbf{B} \in \mathbb{R}^{(N-1)\times N}$ is a two-diagonal matrix given by

$$\mathbf{B} = \begin{pmatrix} -\sqrt{\frac{2k_BT}{\zeta_1}} & \sqrt{\frac{2k_BT}{\zeta_2}} & 0 & 0 & \dots & 0 & 0 \\ 0 & -\sqrt{\frac{2k_BT}{\zeta_2}} & \sqrt{\frac{2k_BT}{\zeta_3}} & 0 & \dots & 0 & 0 \\ 0 & 0 & -\sqrt{\frac{2k_BT}{\zeta_3}} & \sqrt{\frac{2k_BT}{\zeta_4}} & \dots & 0 & 0 \\ \vdots & \vdots & \vdots & \vdots & \ddots & \vdots & \vdots \\ 0 & 0 & 0 & 0 & \dots & -\sqrt{\frac{2k_BT}{\zeta_{N-1}}} & \sqrt{\frac{2k_BT}{\zeta_N}} \end{pmatrix}$$

and $\mathrm{d}\mathbf{W}$ is N-dimensional noise vector $\mathrm{d}\mathbf{W} = [\mathrm{d}W_{1,1}, \mathrm{d}W_{2,1}, \mathrm{d}W_{3,1}, \dots, \mathrm{d}W_{N,1}]^{\mathrm{T}}$. The stationary covariance matrix, defined by

$$\mathbf{C} = \lim_{t\to\infty} \langle \mathbf{y}\, \mathbf{y}^{\mathrm{T}} \rangle,$$

is the solution of Lyapunov equation [71] $\mathbf{AC} + \mathbf{CA}^{\mathrm{T}} + \mathbf{BB}^{\mathrm{T}} = 0$. It can be easily verified that the unique solution of this equation is diagonal matrix $\mathbf{C} \in \mathbb{R}^{(N-1)\times(N-1)}$ with diagonal elements $b_i^2/3$, $i = 1, 2, 3, \dots, N-1$. Multiplying this result by 3 (the

number of coordinates), we obtain (2.17). The end-to-end distance can be rewritten as $\mathbf{R} = \mathbf{r}_N - \mathbf{r}_1 = \sum_{n=2}^{N} (\mathbf{r}_n - \mathbf{r}_{n-1})$. Substituting into (2.18), using (2.17) and the fact that the stationary covariance matrix $\mathbf{C}$ is diagonal, we obtain (2.18). □

2.2.3 Optimal model refinement in time and space

Lemmas 2.2 and 2.3 describe theoretical results which have been derived under slightly different assumptions. Lemma 2.2 is formulated as a property of Algorithm 2.1, but the same result, equation (2.10), also holds when we calculate the translational diffusion coefficient of the SDE formulation of the multi-resolution bead-spring model (2.1). Algorithm 2.1 is designed in such a way that all force terms corresponding to springs cancel when the evolution equation for $\mathbf{r}_G^{i\Delta t}$ is derived (see equation (2.11)). In particular, Lemma 2.2 holds for any choices of the lengths of timesteps associated with different springs.

On the other hand, Lemma 2.3 describes the property of the SDE formulation (2.1). If we use a discretized version of (2.1), then we introduce a discretization error. This error can be made smaller by choosing smaller timesteps. In this section, we show that the smallest timesteps are only required in the regions with the highest spatial resolution. We define a family of optimal multi-resolution (OMR) models designed to have macroscopic properties invariant to resolution regime.

In the remainder of this chapter and in Chapter 3, we shall use lower case Greek subscripts α (resp. β and γ) to denote regions, while n (resp. m and k) are indices referring to numbers of individual beads and springs along the polymer chain.

Definition 2.3 *Let us consider a bead-spring polymer consisting of N beads of radius σ connected by $(N-1)$ springs with the Kuhn length b and simulated by* (2.6) *with timestep Δt. This provides the highest resolution model as a base from which we coarse grain for the multi-resolution model. Let us divide the polymer into $R > 1$*

regions containing N_α, $\alpha = 1, 2, \ldots, R$, *consecutive springs, i.e.*

$$\sum_{\alpha=1}^{R} N_\alpha = N - 1. \tag{2.19}$$

The first region contains springs indexed by $\{1, 2, \ldots, N_1\}$ *and the* α^{th} *region,* $\alpha = 2, 3, \ldots, R$, *contains springs indexed by* $\{\sum_{k=1}^{\alpha-1} N_k + 1, \sum_{k=1}^{\alpha-1} N_k + 2, \ldots, \sum_{k=1}^{\alpha} N_k\}$. *Let us associate with each region an integer resolution* s_α, *where* $s_\alpha \mid s_{\alpha-1}$ *or* $s_{\alpha-1} \mid s_\alpha$, *for* $\alpha = 2, 3, \ldots, R$, *and* $s_\alpha^2 \mid N_\alpha$ *for* $\alpha = 1, 2, 3, \ldots, R$, *with at least one region in resolution* $s_\alpha = 1$ *which is the same level of resolution as the underlying highest-resolution model. Larger values of* s_α *represent coarser representations of the filament. We define the* OMR *model as the multi-resolution bead-spring model which consists of* R *regions of consecutive beads and springs. In the* α^{th} *region, we have* $\widetilde{N}_\alpha$ *springs with Kuhn length* $\widetilde{b}_\alpha$ *and associated time steps* $\widetilde{\Delta t}_\alpha$ *given by*

$$\widetilde{N}_\alpha = \frac{N_\alpha}{s_\alpha^2}, \qquad \widetilde{b}_\alpha = s_\alpha b, \qquad \widetilde{\Delta t}_\alpha = s_\alpha^4 \Delta t, \qquad \widetilde{\sigma}_\alpha = s_\alpha^2 \sigma, \tag{2.20}$$

where $\widetilde{\sigma}_\alpha$ *is the radius of beads which are connected to two springs which have the same Kuhn length* $\widetilde{b}_\alpha$. *We assume that the bead radius of beads on region boundaries sharing springs with Kuhn lengths* $\widetilde{b}_{\alpha-1}$ *and* $\widetilde{b}_\alpha$ *is* $(\widetilde{\sigma}_{\alpha-1} + \widetilde{\sigma}_\alpha)/2$, *for* $\alpha = 2, 3, \ldots, R$. *Moreover, we assume that the bead radius of the first and last bead of the polymer chain are equal to* $(\sigma + \widetilde{\sigma}_1)/2$ *and* $(\sigma + \widetilde{\sigma}_R)/2$, *respectively.*

Substituting scalings (2.20) into (2.8), and using (2.19), we obtain that the OMR model satisfies

$$\Omega = \sigma + \sum_{\alpha=1}^{R} \widetilde{\sigma}_\alpha \widetilde{N}_\alpha = \sigma N,$$

Substituting into (2.10), we deduce that the OMR model has the same translational diffusion coefficient as the original detailed model (given by (2.9)). Considering the limit $t \to \infty$, we can use Lemma 2.3 and scalings (2.20) to derive the expected rms

end-to-end distance for the filament:

$$\mu_\infty = \sqrt{\sum_{\alpha=1}^{R} \widetilde{N}_\alpha \widetilde{b}_\alpha^2} = \sqrt{(N-1)b^2},$$

which is again independent of the choice of resolutions s_α, $\alpha = 1, 2, \ldots, R$. As the Kuhn length and bead radius vary across resolutions, it is important to consider the numerical stability of the model [164]. We choose timesteps to be sufficiently small so that solutions do not grow exponentially large in the highest resolution model. In discretized equations of Algorithm 2.1, drift terms appear in the form $(k_n/\zeta_n)(\mathbf{r}_{n+1} - \mathbf{r}_n)\Delta t_n$. If we suppose beads n and $n+1$ lie in the α^{th} region, then the drift term is proportional to

$$\frac{1}{\widetilde{b}_\alpha^2 \widetilde{\sigma}_\alpha} \big(\mathbf{r}_{n+1} - \mathbf{r}_n\big) \widetilde{\Delta t}_\alpha. \tag{2.21}$$

Using scalings (2.20) and assuming that $(\mathbf{r}_{n+1} - \mathbf{r}_n)$ is of the same order as the Kuhn length $\widetilde{b}_\alpha$, we obtain that the size of (2.21) scales with s_α. Assuming that Δt is chosen in the original fine scale model so that $(k/\zeta)(\mathbf{r}_{n+1} - \mathbf{r}_n)\Delta t$ is small compared to the Kuhn length b, then the drift term of the OMR model, given by (2.21) is also small compared to $\widetilde{b}_\alpha$, the characteristic lengthscale of the OMR model in the α^{th} region, $\alpha = 1, 2, \ldots, R$.

We also wish to compare the number of calculations made by the original detailed single-scale Rouse model with the OMR model. The α^{th} region has $\widetilde{N}_\alpha$ springs simulated with timestep $\widetilde{\Delta t}_\alpha$. Using scalings (2.20), we obtain that we use s_α^6-times fewer calculations in the α^{th} region by advancing fewer beads over larger timesteps. Assuming that the computational intensity of the simulation of the detailed model in each region is proportional to the size of the region, $N_\alpha/(N-1)$, we can quantify the fraction of computational time which is spent by the OMR model (as compared

to the detailed model) by

$$\sum_{\alpha=1}^{R} \frac{N_\alpha}{N-1} \frac{1}{s_\alpha^6}. \tag{2.22}$$

For example, if we coarse-grained the detailed model everywhere using the integer resolution $s_1 = 2$, then (2.19) and (2.22) implies that we speed up our simulations by the factor of 2^6.

2.2.4 Simulation results

In this section we show that simulations of the OMR method outlined in Algorithm 2.1 using scalings (2.20) match the original single-scale Rouse model. We also compare this to analytic results predicted from equations (2.10) and (2.16) for the rms end-to-end distance and the translational diffusion coefficient of a filament in an equilibrium state. For the detailed model, we choose the parameters:

$$\Delta t = 0.8\,\mu\text{s}, \qquad \text{b} = 60\,\text{nm}, \qquad \sigma = 1.2\,\text{nm}, \tag{2.23}$$

where the Kuhn length is chosen to be longer than the persistence length of DNA, which has been found to be less than 60 nm [63]; timestep is chosen in order to give stable simulations, and σ is arbitrary, but could be chosen to give a desired diffusion. For the remainder of this chapter, we shall use $k_B = 1.4 \times 10^{-23}\,\text{J}\,\text{K}^{-1}$, $T = 300\,\text{K}$ and $\eta = 1\,\text{mPa}\cdot\text{s}$, the viscosity of water.

2.2.4.1 Comparison at equilibrium

We compare two resolution regimes for the same system, with the single scale model considering the full system in high resolution and a multi-resolution model considering the middle 10% of the filament in high resolution and the remainder in low resolution. The corresponding parameters of the OMR model are given in Table 2.1. The OMR model contains 69 beads connected by 68 springs, while the original detailed model

Region	$\alpha = 1$	$\alpha = 2$	$\alpha = 3$
N_α	225	50	225
s_α	5	1	5
$\widetilde{N}_\alpha$	9	50	9
$\widetilde{b}_\alpha$	300 nm	60 nm	300 nm
$\widetilde{\Delta t}_\alpha$	500 μs	0.8 μs	500 μs
$\widetilde{\sigma}_\alpha$	30 nm	1.2 nm	30 nm

Table 2.1: *Parameters of the* OMR *model system used to demonstrate consistency.*

is given by 501 beads connected by 500 springs.

We generate the initial configuration of the polymer filament using a generalization of the FJC model [62, 91] to multiple resolutions. The chain is generated iteratively, with the $(n+1)^{\text{th}}$ bead in the chain placed uniformly at random on the surface of the sphere with radius b_n centred on the n^{th} bead, so that a chain is produced with unconstrained random angles [7]. We run the model for 1s and estimate both the rms end-to-end distance and the translational diffusion coefficient of a filament in an equilibrium state. The results are given in Table 2.2. From the results we can see that the OMR model accurately maintains macroscopic properties at a fraction of the number of calculations of the detailed model, where 99.94% of the calculations are used to update beads in the fine resolution region.

The length of the simulated DNA was chosen to be short enough for easy computation, but long enough to be comparable to real simulations of the DNA behaviour [154]. Those simulations showed the diffusion of DNA to be a thousand times larger than our simulations, this is due in part to neglecting hydrodynamic forces, which gives a different form of the expected translational diffusion coefficient [33] compared to (2.10).

Model	Translational diffusion coefficient[$\mu m^2 s^{-1}$]	rms end-to-end distance [μm]	Number of calculations
Analytic results	3.66×10^{-4}	1.34	N/A
Detailed model	3.55×10^{-4}	1.36	100%
Multiscale	3.67×10^{-4}	1.34	10.006%

Table 2.2: *Comparison of results between the original Rouse model, the multi-resolution Rouse model and analytic results* [33]. *The number of calculations is given by* (2.22). *Estimated from simulations run for* 1s *for each system. Analytic results given by equations* (2.10) *and* (2.16).

2.2.4.2 Compacting the filament

We have shown that the dynamics of some multiple resolution systems match the analytic results at equilibrium predicted by equations (2.10) and (2.16). It is also important to show that non-equilibrium dynamics of the detailed system can be replicated by the multiple resolution systems. We consider a filament shrunk so that all beads begin at the origin and compare how the models expand towards equilibrium. We compare four systems (C1, C2, C3 and C4) given in Table 2.3 which, by construction, have the same rms end-to-end distance, but which vary in their level of detail and the number of resolutions considered.

Model C2 in Table 2.3 is the most detailed model which uses the same parameters as in (2.23). We compare the time evolution of rms end-to-end distance of the considered polymer chain models. The results (averaged over 10^3 realizations) are shown in Figure 2.2.

Scheme	C1	C2	C3		C4		
Region	$\alpha = 1$	$\alpha = 1$	$\alpha = 1$	$\alpha = 2$	$\alpha = 1$	$\alpha = 2$	$\alpha = 3$
N_α	250	250	125	125	100	50	100
s_α	5	1	1	5	1	5	1
$\widetilde{N}_\alpha$	10	250	5	125	4	50	4
$\widetilde{b}_\alpha$	300 nm	60 nm	300 nm	60 nm	300 nm	60 nm	300 nm
$\widetilde{\Delta t}_\alpha$	500 μs	0.8 μs	500 μs	0.8 μs	500 μs	0.8 μs	500 μs
$\widetilde{\sigma}_\alpha$	30 nm	1.2 nm	30 nm	1.2 nm	30 nm	1.2 nm	30 nm

Table 2.3: *The* OMR *systems used for testing the multi-resolution formulation outside of equilibrium in a compacted state.*

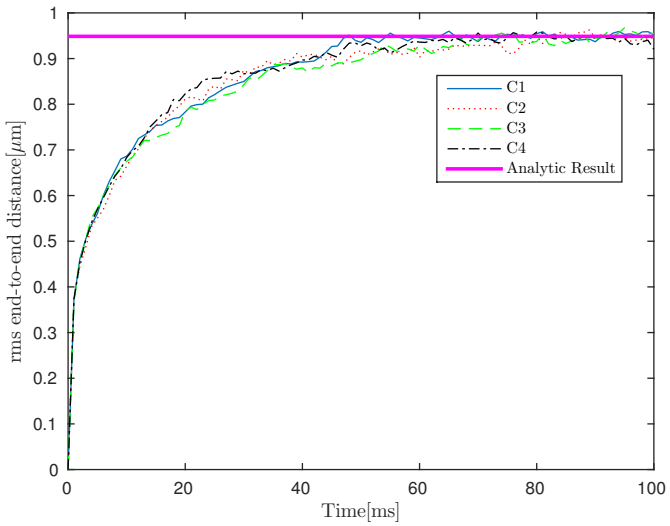


Figure 2.2: *The rms end-to-end distance for a compacted filament to re-extending towards the analytic (equilibrium) rms end-to-end distance in magenta for systems* C1–C4 *given in Table* 2.3 *averaged over* 10^3 *realizations.*

2.3 DNA binding model

To show the usefulness of the OMR model, we have devised an illustrative model for the relationship between a DNA binding protein and a segment of DNA. There is a large variety of different binding proteins, for example transcription factors or polymerases. In general, binding protein dynamics are not fully understood and vary greatly depending on the function of the protein [66]. In many BD models, a protein binds to DNA with a given probability if it comes within a certain distance of the binding site on the DNA filament [39]. We will use a simple version of this approach and assume that a protein binds to DNA if it comes within a 'binding radius' of a bead in the bead-spring polymer chain.

We apply the multi-resolution aspect of the model by adjusting the resolution regime of the filament dynamically, so that as the binding protein moves close to the filament, nearby filament sections increase in resolution. To increase the resolution on-the-fly, we develop a Markov chain Monte Carlo (MCMC) scheme, as well as the ability to decrease the resolution on-the-fly when the protein moves away from the filament. The model is presented as a two-resolution model for simplicity, but it can easily be extended to more resolution levels. We denote by s the ratio in resolution between high and low regions. Using the notation introduced in Definition 2.3, we consider filaments which include regions with higher resolution (where $s_\alpha = 1$ in Definition 2.3) and regions with lower resolution (where $s_\alpha = s$).

A similar approach has previously been used for models which utilize multiple resolutions, where elements within the system can freely move between different resolutions, usually between atomistic and coarse-grained MD. An overview of this adaptive resolution scheme is given in [143].

2.3.1 Resolution increase with MCMC

We first present a framework for increasing the resolution between adjacent beads. If we wish to increase the resolution in a region of low resolution between adjacent beads $\mathbf{r}_A$ and $\mathbf{r}_B$ which lie a distance d apart, then by Definition 2.3 we introduce s^2-1 new springs with Kuhn length b. We place the new beads between $\mathbf{r}_A$ and $\mathbf{r}_B$ to lie a distance of d' apart, which is in general not equal to b, because d is in general not equal to sb. We select d' so that the rms end-to-end distance for the new chain formed between $\mathbf{r}_A$ and $\mathbf{r}_B$ is equal to d at the time of its creation. Using equation (2.16), we require $d' = d/s$ to be the distance between each bead. It should be noted that we are generating beads by the FJC model, such that the initial distance between each new bead is the same. This is for simplicity as when we apply the dynamics there is a fast transition for these bond lengths to revert to the equilibrium distribution given by the GC model [33].

In order to apply MCMC, we seek the probability function ϕ of a chain $C = \{\mathbf{r}_n \,|\, n = 1, 2, \ldots, M\}$ of $M = s^2 - 1$ beads a distance d' apart between $\mathbf{r}_A$ and $\mathbf{r}_B$. We first consider the probability function for the first $M-1$ beads $\{\mathbf{r}_{n<M}\} = \{\mathbf{r}_n \,|\, n = 1, 2, \ldots, M-1\}$, which is proportional to the circumference of the circle of points on which the last bead $\mathbf{r}_M$ can be placed, which we call the *circle of allowable points* Γ. This is given as the set

$$\Gamma = \{\mathbf{r} : |\mathbf{r}_{M-1} - \mathbf{r}| = d' \text{ and } |\mathbf{r}_B - \mathbf{r}| = d'\},$$

or the set of all points a distance d' from both $\mathbf{r}_{M-1}$ and $\mathbf{r}_B$. Note that in many cases $|\mathbf{r}_{M-1} - \mathbf{r}_B| > 2d'$, which gives $\Gamma = \emptyset$ and that $\phi(\{\mathbf{r}_{n<M}\})$ is proportional to the circumference of circle Γ and therefore it is also proportional to its radius.

Provided $\Gamma \neq \emptyset$, to find the radius of Γ we consider the triangle with points $\mathbf{r}_{M-1}$, $\mathbf{u}$, which is an arbitrary point on Γ, and $\mathbf{v}$, which is the midpoint between $\mathbf{r}_{M-1}$

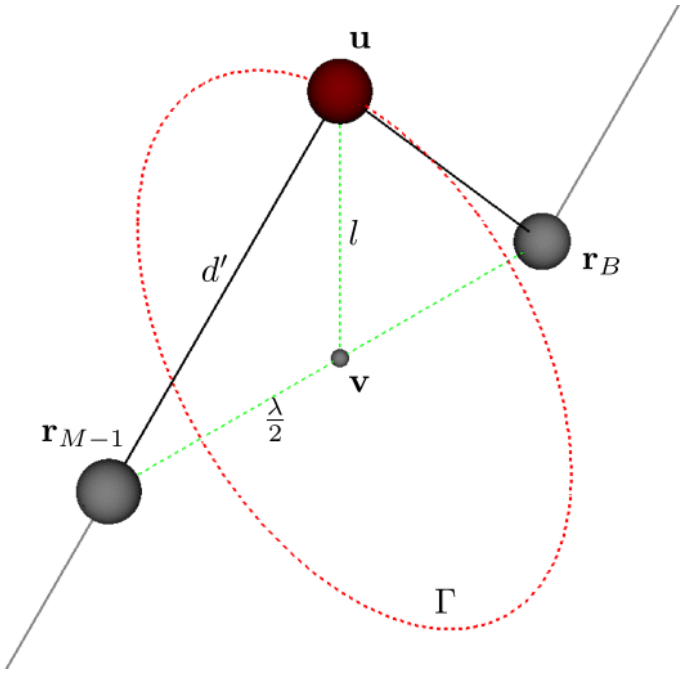


Figure 2.3: *Schematic of the calculation of the probability density ϕ in the resolution increase* MCMC *model. The circle Γ is defined such that every point is a distance d' from both $\mathbf{r}_B$ and $\mathbf{r}_{M-1}$, with centre $\mathbf{v}$, the midpoint of $\mathbf{r}_B$ and $\mathbf{r}_{M-1}$, and $\mathbf{u}$ is an arbitrary point on this circle.*

and $\mathbf{r}_B$. By construction there is a right angle at $\mathbf{v}$. The radius of Γ is given by the distance between $\mathbf{u}$ and $\mathbf{v}$, which is $l = \sqrt{d'^2 - (\lambda/2)^2}$, where λ is the distance between $\mathbf{r}_{M-1}$ and $\mathbf{r}_B$. These points are all shown in Figure 2.3. We therefore find the probability density function for the chain:

$$\phi(C) = \begin{cases} K\sqrt{d'^2 - (\lambda/2)^2} \prod_{n=1}^{M-1} \delta\Big(|\mathbf{r}_n - \mathbf{r}_{n-1}| - d'\Big), & \text{if } \Gamma \neq \emptyset; \\ 0, & \text{if } \Gamma = \emptyset; \end{cases}$$

with normalization constant K, $\mathbf{r}_0 = \mathbf{r}_A$ and $\delta(x)$ is defined in (2.5). To select from the probability distribution ϕ, we apply the Metropolis-Hastings algorithm [24] as outlined in Algorithm 2.2. Given the first $M-1$ beads, and provided $\Gamma \neq \emptyset$, the

Generate a proposal chain $\hat{C} = \{\hat{\mathbf{r}}_n \,|\, n = 1, 2, \ldots, M-1\}$ with each spring length d' starting at $\mathbf{r}_A$ from the FJC model.
if $|\hat{\mathbf{r}}_{M-1} - \mathbf{r}_B| < 2d'$ **then**
  Generate ν uniformly at random in $[0, 1]$.
  Let $\alpha = \min(\phi(\hat{C})/\phi(C^i), 1)$.
  if $\nu < \alpha$ **then**
    Pick $\hat{\mathbf{r}}_M$ uniformly at random on the circle of points distance d' from both $\hat{\mathbf{r}}_{M-1}$ and $\mathbf{r}_B$.
    Select $C^{i+1} = \hat{C}$.
  else
    Select $C^{i+1} = C^i$.
  end
else
  Repeat and generate a new proposal chain.
end

Algorithm 2.2: *The algorithm for picking the next chain C^{i+1} in the Metropolis-Hastings algorithm given the previous chain C^i.*

density function for the final bead is given by

$$\frac{1}{\sqrt{d'^2 - (\lambda/2)^2}}\, \delta(|\mathbf{r}_M - \mathbf{r}_{M-1}| - d')\, \delta(|\mathbf{r}_B - \mathbf{r}_M| - d').$$

Algorithm 2.2 is a Metropolis-Hastings algorithm with a candidate-generating distribution which uses rejection sampling [123] to keep selecting chains $\hat{C} = \{\hat{\mathbf{r}}_n \,|\, n = 1, 2, \ldots, M-1\}$ with distance d' between each bead until we find a chain where the second last bead $\hat{\mathbf{r}}_{M-1}$ is within a distance $2d'$ from the endpoint $\mathbf{r}_B$, which is then used as the candidate. Based on 10^4 simulations we see approximately a 77.5% acceptance of the candidate for $M \geq 3$ beads generated between beads a distance b apart, invariant to the number of beads for $M \geq 3$. To ensure the Markov chain is sufficiently well mixed and that we have 'lost memory' of the initial chain, we choose the 10^{th} filament in the sequence generated from Algorithm 2.2; in 10^3 simulations with a resolution difference of 3, we see only one case where the initial distribution is the same as the 10^{th}.

2.3.2 Model description

On top of our multi-resolution Rouse model, we introduce a binding protein, modelled as a diffusing particle with diffusion constant D_P. The position of the binding protein at time t is denoted $\mathbf{a}(t) \in \mathbb{R}^3$. We assume that it evolves according to the discretized Brownian motion

$$\mathbf{a}(t + \Delta t) = \mathbf{a}(t) + \sqrt{2D_P \Delta t}\, \boldsymbol{\xi}, \tag{2.24}$$

where $\boldsymbol{\xi} \sim [\mathcal{N}(0,1), \mathcal{N}(0,1), \mathcal{N}(0,1)]$ and Δt is the time step of the highest resolution of the polymer. Associated with the binding protein is a binding radius d_B, such that if any bead along the filament comes within a distance d_B from the binding protein then the protein 'binds' to the filament and the simulation finishes. We also consider the protein to have drifted to infinity and therefore fail to bind if it gets a distance d_∞ from all beads which exist in the lowest resolution of the OMR model.

The binding protein has a resolution increase radius r_I (where $r_I > d_B$), so that if the protein is within a distance r_I from a bead with an adjacent spring in low resolution then we change the spring to be high resolution and introduce new beads as described in Section 2.3.1, and reformulate bead radius, timestep and Kuhn length according to the OMR model in Definition 2.3. See Figure 2.4 for an example of the resolution increasing as the filament comes within range of the protein.

As well as zooming in to specific areas of the filament, we include a provision that if the protein moves away far enough from the zoomed in filament section that it will not be interacting with the filament, then we zoom out. This is implemented as a *zoom out factor* Z, so that if the protein moves $Z\, r_I$ away from both beads on the boundary of a region in high resolution, then we 'zoom out' by changing the resolution of the region to the lower resolution and removing all beads inside.

To initialize the simulation, we generate the filament using the FJC model, with R regions each containing one spring and the beads on the region boundaries denoted

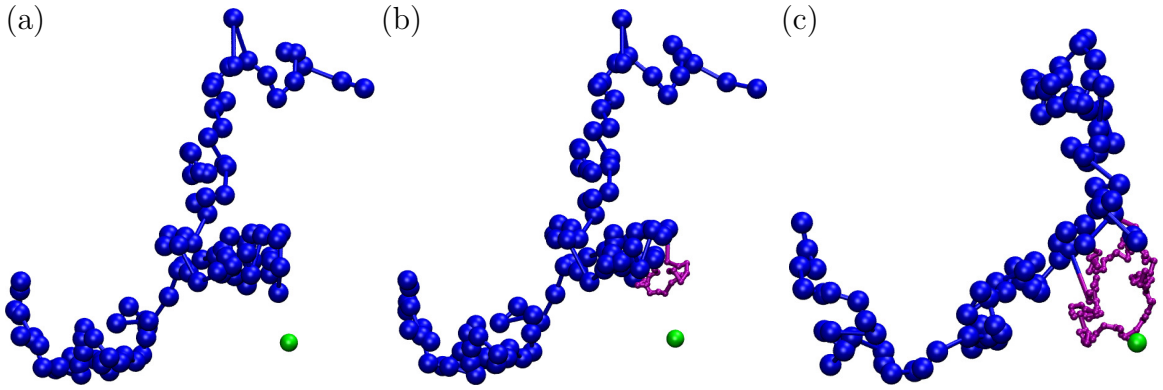


Figure 2.4: *Snapshots of the DNA binding model, taken from an illustrative OMR simulation. In* (a) *the filament is represented by blue in its lowest resolution with the binding protein in green. This is a snapshot from just before the protein comes within resolution increase radius r_I. In* (b) *the protein has moved closer than this radius, so we increase the resolution in this region. The higher resolution region is shown in purple. We continue the simulation until either the protein drifts away from the filament or binds to it, as we see in* (c).

$\mathbf{q}_\alpha^0$, $\alpha = 1, 2, \ldots, R+1$. Since all regions are in low resolution at time $t = 0$, the initial scalings from (2.20) are given by

$$\widetilde{N}_\alpha = 1, \qquad \widetilde{b}_\alpha = s\, b, \qquad \widetilde{\Delta t}_\alpha = s^4 \Delta t, \qquad \widetilde{\sigma}_\alpha = s^2 \sigma, \tag{2.25}$$

for all regions $\alpha = 1, 2, \ldots, R$; where s is the resolution ratio between the high and low resolution regions. We use $R = 100$ in our illustrative simulations. We then place the protein uniformly at random on the sphere with radius d_0 centred at the middle bead of the chain (i.e. at the $(1 + R/2)$-th bead). Once the initial configuration has been generated, we compute the time evolution of the filament and the protein iteratively using Algorithm 2.3, which describes one timestep of the method. At each time step, the multi-resolution bead-spring polymer is described as in Definition 2.1 by the positions of $N \equiv N(t)$ beads at $\mathbf{r}_n \equiv \mathbf{r}_n^t = [r_{n,1}^t, r_{n,2}^t, r_{n,3}^t]$, $n = 1, 2, \ldots, N(t)$. We initially have $N(0) = R+1$ beads at positions $\mathbf{r}_n^0 = \mathbf{q}_n^0$, for $n = 1, 2, \ldots, N(0)$. As time progresses, some regions are refined, so the value of $N(t)$ changes and indices of some beads are relabeled. To simplify the presentation of Algorithm 2.3, we denote

Calculate the position of the filament at time $t + \Delta t$ by Algorithm 2.1.
Update both $\mathbf{r}_n^{t+\Delta t}$ for $n = 1, 2, \ldots, N(t)$ and $\mathbf{q}_\alpha^{t+\Delta t}$ for $\alpha = 1, 2, \ldots, R+1$.
Calculate the protein position $\mathbf{a}$ at time $t + \Delta t$ by equation (2.24).
if $\min_{1 \le n \le N(t)}(|\mathbf{r}_n^{t+\Delta t} - \mathbf{a}|) < d_B$ **then**
  The protein binds to the filament. **STOP** the simulation.
else if $\min_{1 \le \alpha \le R+1}(|\mathbf{q}_\alpha^{t+\Delta t} - \mathbf{a}|) > d_\infty$ **then**
  The protein drifts to infinity. **STOP** the simulation.
else
  for $\big(\alpha = 1, 2, \ldots, R\big)$ **do**
    if (the α^{th} region is in the low resolution) **then**
      if $\big(|\mathbf{q}_\alpha^{t+\Delta t} - \mathbf{a}| < r_I \quad \textbf{OR} \quad |\mathbf{q}_{\alpha+1}^{t+\Delta t} - \mathbf{a}| < r_I\big)$ **then**
        Introduce new beads according to Algorithm 2.2.
        Adjust bead radius, timestep and Kuhn length in the α^{th} region using Definition 2.3, i.e. use σ, Δt and b, respectively.
      end
    else
      (the α^{th} region is in the high resolution)
      if $\big(|\mathbf{q}_\alpha^{t+\Delta t} - \mathbf{a}| > Z\, r_I \quad \textbf{AND} \quad |\mathbf{q}_{\alpha+1}^{t+\Delta t} - \mathbf{a}| > Z\, r_I\big)$ **then**
        Remove all beads inside the α^{th} region.
        Adjust bead radii $\widetilde{\sigma}_\alpha$, timestep $\widetilde{\Delta t}_\alpha$ and Kuhn length $\widetilde{b}_\alpha$ in the α^{th} region by (2.25).
      end
    end
  end
end
Set $t = t + \Delta t$.

Algorithm 2.3: *One iteration of the algorithm for the DNA binding model.*

by $\mathbf{q}_\alpha \equiv \mathbf{q}_\alpha^t$, $\alpha = 1, 2, \ldots, R+1$, the positions of boundary beads of each region at time t, independently of the fact whether the chain was refined or not in the corresponding region. Note that under this formulation we are able to have two (or more) regions of increased resolution which are far away from each other along the polymer chain, if both increased resolution regions lie close (in the physical space) to the binding protein. The polymer chain between these two sections will be described by the coarser model.

We have confirmed the consistency of the model where resolutions are changed dynamically against analytic results. It performs well with a rms end-to-end distance of $2.997\,\mu$m and diffusion of $7.49 \cdot 10^{-5}\,\mu\text{m}^2\text{s}^{-1}$ compared to expected results from (2.10) and (2.18) of $3\,\mu$m and $7.34 \cdot 10^{-5}\,\mu\text{m}^2\text{s}^{-1}$, respectively, after 10^3 simulations, with parameters given in (2.23) and Table 2.4.

2.3.3 Results of the Binding Model

We compare the results between the OMR model with the classical Rouse model, with the entire filament in the highest resolution. We run Algorithm 2.3 with the parameters given in (2.23) and Table 2.4. At different initial starting distances the model runs until the protein is either bound or has escaped the filament. In Figure 2.5, we present the probability of binding of the protein to the filament, $P_B(d_0)$, as a function of the initial distance $d_0 \in [d_B, 10\,d_\infty]$ of the protein from the middle bead of the filament. We estimate $P_B(d_0)$ as a fraction of simulations which end up with the protein bound to DNA. Each data point in Figure 2.5 represents the value of $P_B(d_0)$ estimated from 10^3 independent realizations of the process. If $d_0 < d_B$, then the protein is immediately bound to DNA, i.e. $P_B(d_0) = 1$ for $d_0 < d_B$. If $d_0 = d_\infty$, then the probability of binding is non-zero, because the initial placement, d_0, is the distance of the protein from the centre of the filament. In particular, the minimum distance from protein to filament is less than or equal to the initial

Symbol	Name	Value	Justification
r_I	Resolution increase radius	$0.5\,\mu$m	Chosen to ensure no instant binding of protein to filament after resolution increase
s	Resolution difference	3	Arbitrary
D_P	Protein diffusion constant parameter	$2 \times 10^{-5}\mu\text{m}^2\text{s}^{-1}$	Approx. the diffusion constant for the filament
d_B	Binding radius	$0.01\,\mu$m	Arbitrary
d_∞	Drift to infinity distance	$1\,\mu$m	Arbitrary
Z	Zoom factor	5	Arbitrary
R	Number of regions	100	Initial number of beads

Table 2.4: *Parameter selection for the binding model, with the remaining parameters identical to those given in* (2.23).

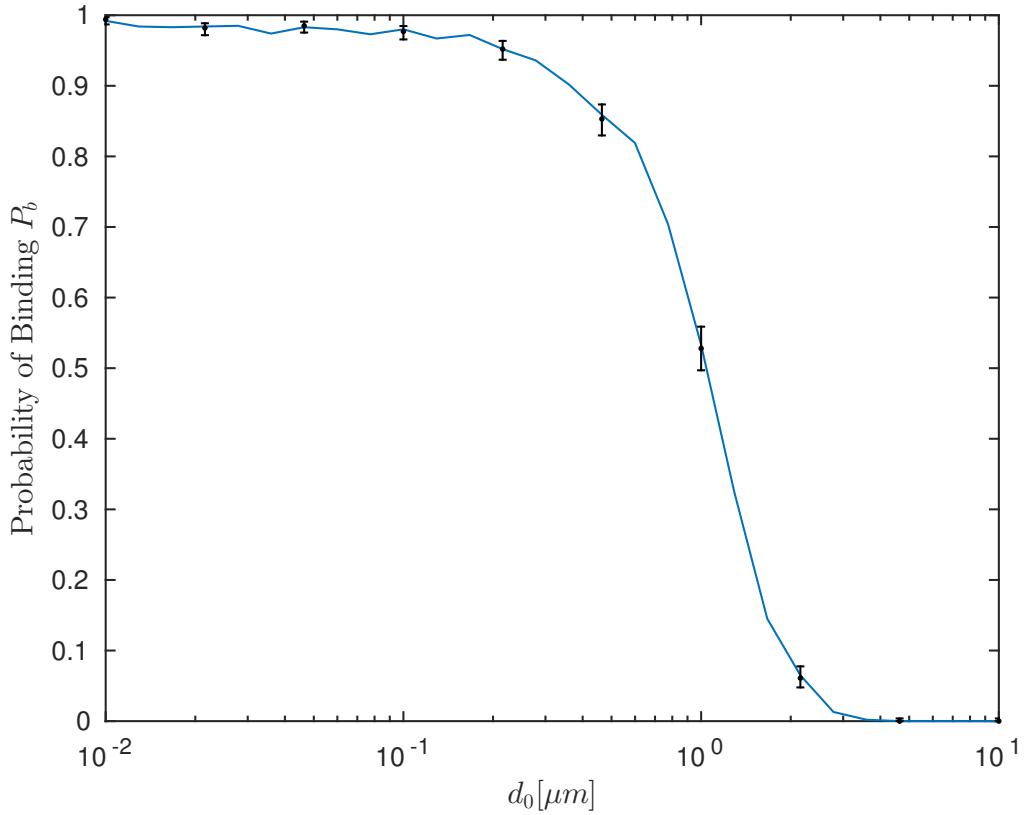


Figure 2.5: *A comparison between the probability of binding of the protein to the DNA filament, $P_B(d_0)$, depending on starting distance, d_0, from the filament for the single-scale (black points) and OMR (blue line) models. Error bars give a 95% confidence interval based on the Wilson score interval for binomial distributions* [193].

placement distance, d_0, and the simulations (with the possibility of binding) take place even if $d_0 = d_\infty$. Due to computational constraints of the single-scale model we consider a selection of initial distances at points $d_0 = 10^{-2+\ell/3}\,\mu$m, $\ell = 0, 1, \ldots, 9$ (black points), where error bars give a 95% confidence interval based on the Wilson score interval for binomial distributions [193]. We run simulations for more initial distances, $d_0 = 10^{-2+\ell/9}\,\mu$m, $\ell = 0, 1, \ldots, 27$ (blue line), using the computationally efficient OMR model and present our results as the blue line in Figure 2.5. We see that $P_N(d_0)$ is very similar between the single-scale and OMR models. The model also succeeds in reducing computational time. For 10^3 simulations with the protein starting $1\,\mu$m from the middle bead, with parameters given in Table 2.4, the OMR

model represented a 3.2-times speed-up compared to the detailed model, with only a 3-times resolution difference. We expect for larger resolution differences to see greater improvements in speed.

2.4 Discussion

In this chapter we have extended basic filament modelling techniques to multiple scales by developing OMR methods. We have presented an MCMC approach for increasing the resolution along a static filament segment, as well as an extension to the Rouse model to dynamically model a filament which considers multiple scales. The bead radius, as well as the number of beads associated with each resolution, is altered to maintain consistency with the end-to-end distance and diffusion of a filament across multiple scales, as well as the timestep to ensure numerical convergence.

We have then illustrated the OMR methodology using a simple model of protein binding to a DNA filament, in which the OMR model gave similar results to the single-scale model. We have also observed a 3.2-times speed-up in computational time on a model which considers only a 3-times increase in resolution, which illustrates the use of the OMR approach as a method to speed up simulations whilst maintaining the same degree of accuracy as the more computationally intensive single-scale model. The speed-up in computational time could be, in some situations, further increased by replacing fixed time step discretization (2.24) by event-based algorithms such as the FPKMC (First passage kinetic Monte Carlo) [127] and GFRD (Green's function reaction dynamics) methods [181].

The OMR method could be applied to modern simulations of DNA and other biological polymers which use the Rouse model [74] in situations where certain regions of the polymer require higher resolutions than other regions. The model considered in this chapter uses Rouse dynamics, which is moderately accurate given its simplicity,

but as we zoom in further towards a binding site, then we will need to start to consider hydrodynamic forces, like in Chapter 3, and EV effects acting between beads [7, 61], which are explored in Chapter 4 for NLC molecules. It could also be of interest to consider some form of a hybrid model which uses the Rouse model in low resolutions and the Zimm model in high resolutions. The combination of different dynamical models might give interesting results regarding hierarchical structures forming as we move between resolutions.

In order to develop more realism in the modelling of the DNA binding model, albeit at a cost of computational efficiency and mathematical tractability, there are many other modelling approaches which could be investigated, many of which are discussed in greater depth in Section 1.3. Some of the themes for increasing realism of the BD modelling would be to apply more complex spring potentials [15,54,167], to look at introducing constraints to angles between beads, for example in the wormlike chain model [3, 64, 89], or look at more microscopic scales where we begin to consider forces between individual histones [84, 159]. There are also MD approaches which could be introduced, either through coarse-grained modelling approaches [121, 175, 180], or atomistic models [136, 200]. On top of this, models for the target searching process by proteins such as transcription factors could be improved, for example, by incorporating facilitated diffusion under crowded environments [17].

This work is limited by the maximum spatial resolution through which the DNA can be modelled. Future work could involve taking a hybrid approach which would use a coarse bead-spring model together with a more detailed modelling approach in a small region of DNA next to the binding protein. Such a hybrid model, with a carefully engineered parameter set, could be used to study microscopic effects contained within the more detailed model while maintaining the consistency of system-level properties.

The need for developing and analyzing multiscale models of DNA which use one

of the above detailed simulation approaches for small parts of the DNA filament is further stimulated by recent experimental results, many of which are outlined in Section 1.2 [10, 51, 125, 125, 183, 195]. To develop more realistic models, site-specific mechanical properties as well as the behaviour of the DNA binding proteins may be utilized when we increase the resolution in our scheme.

When considering the zooming out of the DNA binding model, note that it is generally possible to zoom in and out repetitively, as long as the dynamics are such that we can generate a high resolution structure independent from the previous one (i.e., once we zoom out, the microscopic structure is completely forgotten). However, particularly in the case of chromatin, histone modification and some DNA-binding proteins may act as long-term memory at a microscopic scale below the scales currently considered. To reflect the effect of the memory, some properties of the microscopic structure should be maintained even after zooming out. Fractal dimension may serve as a candidate of indices [118], which can be also estimated in living cells by single-molecule tracking experiments [173]. Topological constraints through the EV and inhibition of chain crossing may play important roles, for example, in chromosome segregation and formation of chromosome territories [59, 60, 80, 159]. To incorporate these effects into the present framework, it will be crucial to design an effective zoom-in operation that keeps the constraints, while existing multiscale modelling methods are useful for construction of the zoom-out operation.

Chapter 3

Multi-resolution polymer Brownian dynamics with hydrodynamic interactions

The work which makes up Chapter 3 of this thesis is from the second year and the beginning of the third year of my DPhil. The work contained is based on my paper co-authored with Radek Erban which has been published in the Journal of Chemical Physics [157], with a few minor changes. These include modified notation and structure in order to be consistent with the other chapters of this thesis as well as much of the paper's introduction has been merged with Chapter 1 of this thesis. Some elements also have been removed to avoid repetition with the previous chapter.

The work in this chapter seeks to build upon the work of Chapter 2 by introducing HI to the multi-resolution polymer model with Hookean springs. I start from a statistical physics description and use the Boltzmann distribution to form a mechanical model, similar to how the single-scale model is built by Doi and Edwards [33]. By using a mobility matrix from Zuk et al. [204], a generalization of the Rotne-Prager-Yamakawa (RPY) tensor [160, 196], to allow for different bead sizes this gives

a diffusive displacement equation. I form analytic expressions for the rms end-to-end distance as well as two approximations for the translational diffusion coefficient: one as a solution to a matrix inversion problem and another in closed form in the long chain limit. Scalings are given for the number of beads, statistical segment length and bead radius in order to maintain macro-scale properties of the polymer filament. The Ermak-McCammon algorithm [41] is extended to allow for multi-resolution modelling on both spatial and temporal scales, and the expressions for end-to-end distance and diffusion are confirmed with illustrative simulations.

This chapter is arranged as follows. In Section 3.1 I formulate the model for the multi-resolution Hookean bead-spring model for a polymer, as well as expressions for the distribution of inter-bead distances. From this description, in Section 3.2 I find approximations for the translational diffusion coefficient. The simulation method is given in Section 3.3 for the multi-resolution model. The scaling laws are shown to maintain the diffusion and end-to-end statistics through simulations in Section 3.4. In Section 3.5 there is a discussion of future directions that this work could take.

3.1 Multi-resolution bead-spring model

The model that we wish to generalize to multiple resolutions is again a bead-spring model for N beads connected by $N-1$ Hookean springs, similar to Definition 2.1, but we now include HI into this model [33], which occur where the movement of one bead exerts a fluid motion on surrounding beads, causing them to move.

To form the multi-resolution model, we start with a static description of the chain as an extension of the GC model, where much of the analysis is similar to the treatment given by Doi and Edwards [33], but with the introduction of varying bond lengths. We use this to derive a potential for spring constants using the Boltzmann distribution. This is a general formulation which can also be used with the work in

Chapter 2. In this case, we use it to form the dynamic model with HI given from a multi-resolution extension of the RPY tensor [160, 196, 204].

3.1.1 Static Description

In order to form a static description of the multi-resolution bead-spring model which we go on to define in Section 3.1.2, we first define a distribution of the bond vector as a Gaussian in Definition 3.1, and seek to derive properties of the chain from this description. This is a different approach to the one taken in Chapter 2 where we started from Definition 2.1 of a diffusive displacement equation and sought to derive properties from it; here we start from a static description of the chain and build up towards a dynamic model.

Definition 3.1 *We consider a static bead-spring polymer model with N beads, where the positions of the beads of the chain are given by $\mathbf{r}_n$, so that $\mathbf{R}_n = \mathbf{r}_{n+1} - \mathbf{r}_n$, for $n = 1, 2, \ldots N-1$, are the corresponding bond vectors. In the multi-resolution GC model, the distribution ψ_n for the n^{th} bond vector $\mathbf{R}_n$, $n = 1, 2, \ldots, N-1$, is defined such that the distribution varies along the chain:*

$$\psi_n(\mathbf{R}_n) = \left(\frac{3}{2\pi b_n^2}\right)^{3/2} \exp\left(-\frac{3\mathbf{R}_n^2}{2b_n^2}\right), \tag{3.1}$$

with statistical segment length $\langle \mathbf{R}_n^2 \rangle = b_n^2$ for the n^{th} bond vector.

In the special case $b = b_n$ for all $n = 1, 2, \ldots, N-1$, equation (3.1) reduces to the standard GC model given by equation (2.37) in [33]. Using (3.1), the distribution of $\mathbf{r}_{mn} = \mathbf{r}_n - \mathbf{r}_m$, for $n \neq m$, is given by

$$\Phi(\mathbf{r}_{mn}) = \left(\frac{3}{2\pi \mu_{mn}^2}\right)^{3/2} \exp\left(-\frac{3(\mathbf{r}_n - \mathbf{r}_m)^2}{2\mu_{mn}^2}\right), \tag{3.2}$$

where we define

$$\mu_{mn}^2 = \sum_{k=\min\{m,n\}}^{\max\{m,n\}-1} b_k^2.$$

If we define the rms end-to-end distance $\mu = \langle \mathbf{R}^2 \rangle^{1/2}$, where $\mathbf{R} = \mathbf{r}_{N1}$ is the vector from the first to the last bead, then we find

$$\mu = \sqrt{\langle (\mathbf{r}_N - \mathbf{r}_1)^2 \rangle} = \mu_{1N} = \sqrt{\sum_{k=1}^{N-1} b_k^2}, \tag{3.3}$$

which is the same as (2.18) for the rms end-to-end distance for the multi-resolution model explored in Chapter 2.

Using (3.1), the conformational distribution function of the chain is given by:

$$\begin{aligned} \Psi(\{\mathbf{r}_n\}) &= \prod_{n=1}^{N-1} \psi_n(\mathbf{R}_n) \\ &= \left(\frac{3}{2\pi \prod_{n=1}^{N-1} b_n^2} \right)^{3/2} \exp\left(- \sum_{n=1}^{N-1} \frac{3\mathbf{R}_n^2}{2b_n^2} \right). \end{aligned} \tag{3.4}$$

If we consider a mechanical model of such a polymer chain, this model would have potential energy

$$U(\{\mathbf{r}_n\}) = \frac{3k_B T}{2} \sum_{n=1}^{N-1} \frac{(\mathbf{r}_{n+1} - \mathbf{r}_n)^2}{b_n^2}, \tag{3.5}$$

to give an identical Boltzmann distribution to equation (3.4).

3.1.2 Dynamic Model Description

Using potential (3.5), we form a diffusive displacement equation for the dynamic model [131] for the n^{th} bead at time t

$$\mathrm{d}\mathbf{r}_n = \left(- \sum_{m=1}^{N} \mathbf{H}_{nm} \frac{\partial U}{\partial \mathbf{r}_m} + \nabla_m \cdot \mathbf{H}_{nm} \right) \mathrm{d}t + \sum_{m=1}^{N} \mathbf{B}_{nm} \, \mathrm{d}\mathbf{W}_m, \tag{3.6}$$

where $\mathbf{H}_{mn} \in \mathbb{R}^{3\times3}$ is a positive-definite symmetric mobility matrix which relates bead velocities to the hydrodynamic forces acting on them, $\mathrm{d}\mathbf{W}_m \in \mathbb{R}^3$ is a Wiener process and we define $\mathbf{B}_{mn} \in \mathbb{R}^{3\times3}$ so that

$$\mathbf{H}_{mn} = \frac{1}{2k_BT}\sum_{k=1}^{N}\mathbf{B}_{mk}\,\mathbf{B}_{nk}^{\mathrm{T}}, \tag{3.7}$$

where T is the absolute temperature, superscript T (Roman font) denotes the transpose of a matrix and k_B is the Boltzmann constant. The matrix $\mathbf{B}_{mk}$ exists due to the positive-definiteness of $\mathbf{H}_{mn}$, and can be found by performing a matrix decomposition (for example the Cholesky decomposition [41]). In choosing the mobility matrix, we would like to vary the bead sizes along the filament, which can be used to ensure that macroscopic properties of the polymer remain constant. Therefore, the bead size σ_n becomes a parameter of n^{th} bead.

Chapter 2 uses a diagonal mobility tensor which is a specific example of this, which works as an extension of the Rouse model:

$$\mathbf{H}_{mn} = \begin{cases} \dfrac{1}{6\pi\eta\sigma_n}\mathbf{I}, & \text{if } m = n; \\ \mathbf{0}, & \text{if } m \neq n; \end{cases} \tag{3.8}$$

where η is the solvent viscosity; $\mathbf{I} \in \mathbb{R}^{3\times3}$ is the identity matrix and $\mathbf{0} \in \mathbb{R}^{3\times3}$ is the zero matrix. One of the purposes of this chapter is to extend the modelling and analysis of the Chapter 2 to include HI. Many models which include HI where beads are of equal sizes use the RPY [160, 196] tensor, which is an extension of the Oseen tensor to allow for overlapping beads. This has been extended by Zuk et al. [204] to allow for beads of different sizes by considering fluid dynamical flows around overlapping and non-overlapping spheres of different sizes. To formulate it,

we denote for beads m and n:

$$\sigma_{mn} = |\sigma_n - \sigma_m|, \quad \text{and} \quad r_{mn} = |\mathbf{r}_n - \mathbf{r}_m|,$$

where σ_m (resp. σ_n) is the radius of bead m (resp. n) and $r_{mn} = |\mathbf{r}_m - \mathbf{r}_n|$ is the distance between beads m and n using the Euclidean norm. We also denote by $\widehat{\mathbf{r}}_{mn}$ the unit vector between beads m and n, i.e.

$$\widehat{\mathbf{r}}_{mn} = \frac{\mathbf{r}_n - \mathbf{r}_m}{r_{mn}}.$$

Then the RPY-type mobility tensor is given by [204]

$$\mathbf{H}_{mn} = \begin{cases} \frac{1}{6\pi\eta\sigma_n}\,\mathbf{I}, & \text{if } m = n; \\ \frac{1}{8\pi\eta r_{mn}}\left[\left(1 + \frac{\sigma_n^2+\sigma_m^2}{3r_{mn}^2}\right)\mathbf{I}\right. & \\ \qquad \left. + \left(1 - \frac{\sigma_n^2+\sigma_m^2}{r_{mn}^2}\right)\widehat{\mathbf{r}}_{mn}\otimes\widehat{\mathbf{r}}_{mn}\right], & \text{if } \sigma_n + \sigma_m < r_{mn}; \\ \frac{1}{6\pi\eta\sigma_n\sigma_m}\left[\frac{16r_{mn}^3(\sigma_n+\sigma_m) - (\sigma_{mn}^2+3r_{mn}^2)^2}{32r_{mn}^3}\,\mathbf{I}\right. & \\ \qquad \left. + \frac{3(\sigma_{mn}^2-r_{mn}^2)^2}{32r_{mn}^3}\widehat{\mathbf{r}}_{mn}\otimes\widehat{\mathbf{r}}_{mn}\right], & \text{if } \sigma_{mn} < r_{mn} \le \sigma_n + \sigma_m; \\ \frac{1}{6\pi\eta\max\{\sigma_n,\sigma_m\}}\,\mathbf{I}, & \text{if } r_{mn} \le \sigma_{mn}; \end{cases} \tag{3.9}$$

which is positive-definite, symmetric and continuous for sufficiently small σ_n for all n. As we are dealing with an unconfined system, this gives $\nabla_m \cdot \mathbf{H}_{nm} = 0$, which simplifies the diffusive displacement equation (3.6) to

$$\mathrm{d}\mathbf{r}_n = \left(\sum_{m=1}^{N} \mathbf{H}_{nm}\,\mathbf{F}_m\right)\mathrm{d}t + \sum_{m=1}^{N} \mathbf{B}_{nm}\,\mathrm{d}\mathbf{W}_m, \tag{3.10}$$

where $\mathbf{B}_{mn} \in \mathbb{R}^{3\times 3}$ are given by (3.7) which exists by the positive-definite symmetric property of $\mathbf{H}_{mn}$ and inter-bead force $\mathbf{F}_m$ is found by differentiating the potential (3.5)

to get

$$\mathbf{F}_m = k_{m-1}\left(\mathbf{r}_{m-1} - \mathbf{r}_m\right) + k_m\left(\mathbf{r}_{m+1} - \mathbf{r}_m\right), \tag{3.11}$$

for $m = 2, 3, \ldots, N-1$ where we reintroduce the Hookean spring constant $k_m = 3k_BT/b_m^2$ from Chapter 2. We treat the end beads $\mathbf{r}_1$ and $\mathbf{r}_N$ by (3.11) as well, where we consider auxiliary beads $\mathbf{r}_0$ and $\mathbf{r}_{N+1}$ defined such that $\mathbf{r}_0 = \mathbf{r}_1$ and $\mathbf{r}_N = \mathbf{r}_{N+1}$. For a schematic of the multi-resolution modelling of beads, Figure 2.1 on page 29 from Chapter 2 is still valid.

3.2 Approximation of the Diffusion Coefficient and Ideal Parameterization

We take a similar approach to Öttinger [130] to find an approximation for the diffusion of the multi-resolution model with HI. This is then used in conjunction with knowledge of the distribution of the rms end-to-end vector from Section 3.1.1 to inform the scaling for a multiscale simulation, so that properties of interest match up to the high-resolution model.

3.2.1 Diffusion Approximation

To find an approximation to the diffusion for the mobility tensor with hydrodynamic terms included, we use the pre-averaging approximation [33], introduced by Zimm [203]. Considering near-equilibrium dynamics, we replace the mobility tensor $\mathbf{H}_{mn}$ with its equilibrium average $\langle \mathbf{H}_{mn} \rangle_{\text{eq}}$, using Ψ from equation (3.4):

$$\mathbf{H}_{mn} \to \langle \mathbf{H}_{mn} \rangle_{\text{eq}} = \int_{\mathbb{R}^{3N}} \mathbf{H}_{mn} \Psi\left(\{\mathbf{r}_n\}\right) \mathrm{d}\{\mathbf{r}_n\}. \tag{3.12}$$

If we assume that $\sigma_n + \sigma_{n+1} < b_n$ for all $n \leq N-1$, then our equilibrium distribution $\langle \mathbf{H}_{mn} \rangle_{\text{eq}}$ for off-diagonal entries $m \neq n$ becomes

$$\langle \mathbf{H}_{mn} \rangle_{\text{eq}} = \frac{1}{8\pi\eta} \left[\left\langle \frac{1}{r_{mn}} \right\rangle_{\text{eq}} \langle \mathbf{I} + \widehat{\mathbf{r}}_{mn} \otimes \widehat{\mathbf{r}}_{mn} \rangle_{\text{eq}} \right. \\ \left. + (\sigma_n^2 + \sigma_m^2) \left\langle \frac{1}{r_{mn}^3} \right\rangle_{\text{eq}} \left\langle \frac{\mathbf{I}}{3} - \widehat{\mathbf{r}}_{mn} \otimes \widehat{\mathbf{r}}_{mn} \right\rangle_{\text{eq}} \right],$$

where we have used that the distribution of $\widehat{\mathbf{r}}_{mn}$ is independent of r_{mn}. Using $\langle \widehat{\mathbf{r}}_{mn} \otimes \widehat{\mathbf{r}}_{mn} \rangle_{\text{eq}} = \mathbf{I}/3$, the second term cancels and we obtain $\langle \mathbf{H}_{mn} \rangle_{\text{eq}} = \widehat{H}_{mn} \mathbf{I}$, where

$$\widehat{H}_{mn} = \begin{cases} \dfrac{1}{6\pi\eta\sigma_n}, & \text{for } m = n; \\ \dfrac{1}{6\pi\eta} \left\langle \dfrac{1}{r_{mn}} \right\rangle_{\text{eq}}, & \text{for } m \neq n. \end{cases}$$

Using (3.2), we obtain

$$\widehat{H}_{mn} = \begin{cases} \dfrac{1}{6\pi\eta\sigma_n}, & \text{for } m = n; \\ \dfrac{1}{\mu_{mn}\, \eta\, \pi \sqrt{6\pi}}, & \text{for } m \neq n. \end{cases} \tag{3.13}$$

In the single-scale model where $b_n = b$ and $\sigma_n = \sigma$ for all n, equation (3.13) generalizes to equation (4.49) from Doi and Edwards [33, 203] for the pre-averaged tensor. Consequently, by pre-averaging equation (3.10), we find

$$\mathrm{d}\mathbf{r}_n = \left(\sum_{m=1}^{N} \widehat{H}_{nm}\, \mathbf{F}_m \right) \mathrm{d}t + \sum_{m=1}^{N} \widehat{B}_{nm}\, \mathrm{d}\mathbf{W}_m, \tag{3.14}$$

where

$$\widehat{H}_{mn} = \frac{1}{2k_B T} \sum_{k=1}^{N} \widehat{B}_{mk} \widehat{B}_{nk}, \tag{3.15}$$

where $\widehat{B}_{nk}$ exists by the positive-definiteness of $\widehat{H}_{mn}$. Following Öttinger [131], we define the hydrodynamic centre of resistance $\mathbf{r}_h$ by

$$\mathbf{r}_h = \sum_{n=1}^{N} l_n \mathbf{r}_n, \qquad \text{where} \qquad l_n = \frac{\sum_{m=1}^{N} \widehat{H}_{nm}^{-1}}{\sum_{m,k=1}^{N} \widehat{H}_{km}^{-1}}.$$

Multiplying equation (3.14) through by l_n and summing over all n, we get

$$\mathrm{d}\mathbf{r}_h = \left(\sum_{m,n=1}^{N} l_n \widehat{H}_{nm} \, \mathbf{F}_m \right) \mathrm{d}t + \sum_{m=1}^{N} \left(\sum_{n=1}^{N} l_n \widehat{B}_{nm} \right) \mathrm{d}\mathbf{W}_m.$$

Using (3.11), the first term on the right hand side is zero and the second term is a linear combination of Wiener processes, which is itself a Wiener process with translational diffusion coefficient

$$D_h = \frac{1}{2} \sum_{m=1}^{N} \left(\sum_{n=1}^{N} l_n \widehat{B}_{nm} \right)^2.$$

Using (3.15) and the definition of l_n, we obtain

$$D_h = k_B T \left(\sum_{m,n=1}^{N} \widehat{H}_{mn}^{-1} \right)^{-1}. \tag{3.16}$$

This forms a matrix equation to provide the pre-averaged approximation for the translational diffusion coefficient.

Our analysis in this section used a general multi-resolution model consisting of N beads with sizes σ_n, $n = 1, 2, \ldots, N$, connected by $N - 1$ springs with statistical segment lengths b_n, $n = 1, 2, \ldots, N - 1$. In applications to multiscale computations, we are mostly interested in chains which are split into R regions (where $R \ll N$) of constant statistical segment length.

We again use the convention that Greek subscripts refer to regions along the polymer, whilst indices n, m, k refer to individual beads.

By generalizing the approach of Öttinger [131] and Fixman [44], we can form a

first-order approximation of this matrix equation in the long chain limit in closed form as the number of beads $N \to \infty$, which is given in the following lemma.

Lemma 3.1 *Suppose we have a multi-resolution chain of R regions such that the α^{th} region contains N_α springs, so that*

$$\sum_{\alpha=1}^{R} N_\alpha = N - 1. \tag{3.17}$$

We take the long chain limit as $N \to \infty$ in such a way that the fraction of springs in each region, $N_\alpha/(N-1)$, remains a constant. In this limit, the pre-averaged approximation to the translational diffusion coefficient (3.16) *can be expressed in closed form to first order approximation by the equation*

$$D_h = \frac{\Gamma^2(1/4)}{4\pi^2\sqrt{3}} \frac{k_B T}{\eta\, \mu} \;\approx\; 0.1922 \frac{k_B T}{\eta\, \mu}, \tag{3.18}$$

where $\Gamma(x)$ is the gamma function.

Proof. Equation (3.13) defines a function of two integer variables m and n. We will map the discrete function $\widehat{H}_{mn}$ into a continuous function $H(x, y)$ by generalizing the approach of Öttinger [131] and Fixman [44] to multiple resolutions. Assuming that bead m lies in region α, its continuous approximation in interval $[-1, 1]$ will be defined by

$$\frac{2b_\alpha^2}{\mu^2}\, m - 1 + \frac{2}{\mu^2} \sum_{\gamma=1}^{\alpha-1} N_\gamma (b_\gamma^2 - b_\alpha^2) \;\longrightarrow\; x, \tag{3.19}$$

where $\mu^2 = \sum_{\gamma=1}^{R} N_\gamma b_\gamma^2$. The continuous analogue of a summation of arbitrary function f_n over all beads will then be a weighted integral

$$\sum_{n=1}^{N} f_n \;\longrightarrow\; \int_{-1}^{1} f(x)\, b(x)\, \mathrm{d}x, \tag{3.20}$$

where we define $b(x)$ as a piecewise constant function given by $b(x) = \mu^2 b_\alpha^{-2}/2$ in

interval

$$x \in \left(\frac{2}{\mu^2} \sum_{\gamma=1}^{\alpha-1} N_\gamma b_\gamma^2 - 1, \frac{2}{\mu^2} \sum_{\gamma=1}^{\alpha} N_\gamma b_\gamma^2 - 1 \right].$$

In addition to (3.19), we also write for bead n in region β

$$\frac{2b_\beta^2}{\mu^2}\, n - 1 + \frac{2}{\mu^2} \sum_{\gamma=1}^{\beta-1} N_\gamma (b_\gamma^2 - b_\beta^2) \;\longrightarrow\; y.$$

This leads to a transformation $(m, n) \to (x, y)$, which gives the continuous approximation of $\widehat{H}_{mn}$ in $[-1, 1] \times [-1, 1]$ as

$$H(x, y) = \sqrt{\frac{2}{\mu^2}} \frac{1}{\eta\pi\sqrt{6\pi|x - y|}}. \tag{3.21}$$

The definition of the inverse of the matrix $\widehat{H}_{mn}$ (given as $\sum_{k=1}^{N} \widehat{H}_{mk}\widehat{H}_{kn}^{-1} = \delta_{mn}$), is rewritten in continuous variables as

$$\int_{-1}^{1} H(x, z)\, H^{-1}(z, y)\, b(z)\, \mathrm{d}z = \frac{\delta(x - y)}{b(x)}, \tag{3.22}$$

where we retain the definition of $\delta(x)$ and δ_{mn} from (2.5). Multiplying both sides by $b(y)$, integrating over y and using (3.21), we obtain

$$\int_{-1}^{1} \frac{\phi(z)}{\sqrt{|x - z|}}\, \mathrm{d}z = \eta\, \mu\, \pi\, \sqrt{3\pi}, \tag{3.23}$$

where

$$\phi(z) = \int_{-1}^{1} b(y)\, b(z)\, H^{-1}(z, y)\, \mathrm{d}y.$$

We use the the method of Auer and Gardner [9, 44] to solve (3.23) for $\phi(z)$ by introducing the Gegenbauer polynomials defined on $[-1, 1]$ as:

$$G_n^{(\nu)}(x) = \frac{(-1)^n \Gamma(\nu + 1)}{2^n \Gamma(n + \nu + 1)} \left(1 - x^2\right)^{-\nu} \frac{\mathrm{d}^n}{\mathrm{d}x^n} \left(1 - x^2\right)^{n+\nu}. \tag{3.24}$$

We use the result from Auer [9] that we may rewrite $|x-z|^{-1/2}$ as

$$|x-z|^{-1/2} = \sum_{n=0}^{\infty} a_n(1/4) G_n^{(1/4)}(x) G_n^{(1/4)}(z), \tag{3.25}$$

for constants $a_n(\nu)$ given in [9]. If we substitute (3.25) into (3.23) and write $\phi(z)$ as an infinite sum of these polynomials

$$\phi(z) = \sum_{m=0}^{\infty} c_m G_m^{(1/4)}(z) \left(1-z^2\right)^{-1/4}, \tag{3.26}$$

this gives the equation

$$\sum_{n,m=0}^{\infty} a_n(1/4) c_m G_n^{(1/4)}(x) \int_{-1}^{1} G_n^{(1/4)}(z) G_m^{(1/4)}(z) \left(1-z^2\right)^{-1/4} \mathrm{d}z = \eta\,\mu\,\pi\sqrt{3\pi}. \tag{3.27}$$

To solve (3.27) we note that the right hand side of the equation is not a function of x and use the orthogonality property of the Gegenbauer polynomials to give $c_m = 0$ for $m > 0$. We therefore obtain an equation for c_0:

$$c_0 = \frac{\eta\,\mu\,\pi\sqrt{3\pi}}{a_0(1/4) \displaystyle\int_{-1}^{1} \left(G_0^{(1/4)}(z)\right)^2 (1-z^2)^{-1/4} \mathrm{d}z} \tag{3.28}$$

which can be solved to give the closed form equation for $\phi(z)$:

$$\phi(z) = \frac{\eta\,\mu\,\sqrt{3\pi}}{\sqrt{2}\,(1-z^2)^{1/4}}. \tag{3.29}$$

To return to the quantity of interest, $\sum\sum \widehat{H}_{nm}^{-1}$, we apply the mapping from

equation (3.20) to give

$$\sum_{n=1}^{N}\sum_{m=1}^{N}\widehat{H}^{-1}_{nm} = \int_{-1}^{1}\int_{-1}^{1} b(x)b(y)H^{-1}(x,y)\,\mathrm{d}y\,\mathrm{d}x$$
$$= \int_{-1}^{1}\phi(x)\,\mathrm{d}x = \frac{\eta\,\mu\,4\pi^2\sqrt{3}}{\Gamma^2(1/4)}. \tag{3.30}$$

Substituting (3.30) into (3.16), we obtain the diffusion coefficient in the long chain limit given by equation (3.18). □

There are also other formulations of the diffusion coefficient in the long-chain limit for the single-scale model, for example the Kirkwood-Riseman formulation [15,82] has the constant multiplier 0.1955 in front of the expression in (3.18). This was calculated by using equilibrium averages for internal configurations to find an approximation for the diffusion coefficient [130, 152].

3.2.2 Scaling of Parameters

As the use of a bead-spring model is to give a coarse-grained representation of a filament, statistical segment length and bead radius are not physical qualities so we allow these parameters of the model to vary in order to achieve desired statistics of interest for the polymer. In Chapter 2, the whole-system statistics of interest are the rms end-to-end distance μ and translational diffusion coefficient D_h of a polymer chain. In this chapter, we also seek to hold μ and D_h constant, but now with the introduction of HI we would like to hold the strength of HI [95] constant, defined in terms of the parameter h^* by

$$h^* = \sqrt{\frac{3}{\pi}}\frac{\sigma}{b},$$

where b is the statistical segment length and σ is the bead radius. From a theoretical standpoint, a value for $h^* \approx 0.25$ minimizes the effect of chain length [129]. Similar values can also match experimental results for viscoelastic properties, for example

the Flory-Fox parameter can match experimental values for $h^* \approx 0.267$ [95]. In the multi-resolution model, in order to maintain a consistent value for the strength of HI, we therefore scale parameters in order to keep h^* constant throughout simulations.

The multi-resolution polymer simulations will be compared to the 'highest resolution model', which will be the single-scale model of the polymer in the maximum detail required. In single-scale models, we can modify the whole-system statistics by varying the statistical segment length b, the bead radius σ and the total number of beads N. In single-scale models, we need to select a level of detail for the entire chain as an additional constraint, but by modelling on multiple scales, we instead get to select the resolution of different regions of the polymer, so that only regions of particular interest need to be in the highest level of detail. To parameterize the highest resolution model, we select b to give the desired value for the rms end-to-end distance μ, from equation (3.3), i.e. $b = \mu(N-1)^{-1/2}$. Selecting a value for σ is a bit more subtle than the model without HI in the last chapter, as the inclusion of the HI mean the leading order long chain diffusion approximation in equation (3.18) is independent of σ. We instead use the strength of hydrodynamic interaction h^* to select an appropriate value of σ. For all simulations in this chapter, we use $\sigma = b/4$ to ensure that $h^* = 0.25$.

Once we have defined the highest resolution model, with statistical segment length b, bead radius σ and total beads N, we can seek to define the scalings for the multi-resolution model, where different regions coarse-grain the original model to differing extents. This multi-resolution model should be seen as a reduction in the degrees of freedom of the highest resolution model, which is itself a coarse-grained description of physical reality. We take a similar approach to the one given in Definition 2.3 and divide the highest-resolution polymer into R regions each containing N_α springs for $\alpha = 1, 2, \ldots, R$ such that $\sum_{\alpha=1}^{R} N_\alpha = N - 1$. Each region of the multi-resolution model has an associated (integer-valued) resolution s_α such that $s_\alpha^2 | N_\alpha$. Larger values

of s_α represent coarser regions, and $s_\alpha = 1$ gives the highest resolution model. In the α^{th} region of the multi-resolution model, we have $\widetilde{N}_\alpha$ springs with statistical segment length $\widetilde{b}_\alpha$ given by

$$\widetilde{N}_\alpha = \frac{N_\alpha}{s_\alpha^2}, \qquad \widetilde{b}_\alpha = s_\alpha b, \qquad \widetilde{\sigma}_\alpha = s_\alpha \sigma, \tag{3.31}$$

where the definition of the bead radius, $\widetilde{\sigma}_\alpha$, is slightly modified for the boundary beads; scalings (3.31) apply to beads where both adjacent springs have the same statistical segment length $\widetilde{b}_\alpha$. On the boundaries between regions α and $\alpha + 1$, for $\alpha = 1, 2, \ldots, R-1$, we take the bead radius to be $((\widetilde{\sigma}_\alpha^2 + \widetilde{\sigma}_{\alpha+1}^2)/2)^{1/2}$, and for end beads at the start and end of the polymer we take $\widetilde{\sigma}_1/\sqrt{2}$ and $\widetilde{\sigma}_R/\sqrt{2}$, respectively. By applying scalings (3.31), equation (3.3) gives the expected rms end-to-end distance for the filament at equilibrium to be $\mu = b(N-1)^{1/2}$, i.e. it is equal to the highest resolution model. The translational diffusion coefficient for the polymer in the long chain limit (3.18) is also invariant to the number of regions, as well as the size and resolution of each region, and the strength of HI is constant along the filament.

Note that the scalings (3.31) differ to the ones given in Chapter 2 in (2.20) for the bead radius. This is because in the Rouse model, the equation for diffusion is given by (2.9), so that we wish to keep σN constant. However in the model with HI, in the long chain limit (3.18) there is no dependence on bead radius, so we need to keep σ/b constant in order to keep the strength of HI constant. It would be possible to combine these two definitions by writing them both as $\widetilde{\sigma}_\alpha = s_\alpha^l \sigma$ where $l = 1$ in the model with HI and $l = 2$ in the model without.

3.3 Simulation Method

We simulate the diffusive displacement equation for the polymer (3.10) by using a modified version of the Ermak-McCammon algorithm [41], for which different regions

have different timestep sizes. The key idea for the modified algorithm is to keep track of the behaviour of beads modelled with a higher resolution (and with smaller timesteps) to give an average of the hydrodynamic forces exerted on the coarsely modelled beads between the larger timesteps on which they are modelled.

A number of algorithms have been proposed for efficient BD simulations with HI for the single-scale polymer model in the literature [6, 45, 52, 117], however we choose to adapt the Ermak-McCammon algorithm due to its lack of approximations and simplicity, which can act as a stepping stone for modellers to build upon in future work.

If the highest resolution model uses timestep Δt, then with the notation of Section 3.2.2 we define the timestep associated with the α^{th} region as

$$\widetilde{\Delta t}_\alpha = s_\alpha^3 \Delta t,$$

where s_α is the (integer-valued) resolution of the α^{th} region, $\alpha = 1, 2, \ldots, R$. It is required for any two regions α, β that either $s_\alpha | s_\beta$ or $s_\beta | s_\alpha$, to ensure the timesteps of the coarser regions are multiples to those for the finer regions. We choose this scaling to ensure numerical stability of simulations so that the size of the tension term for a bead is much smaller than the statistical segment length with adjacent beads. This differs slightly to the scalings (2.20) in Chapter 2 because the scalings for the bead radius are different. In the case of a bead lying between two regions, we take the timestep to be the minimum value of the timesteps given by each region.

To define the simulation method , we denote by α_n (resp. β_n) the resolution region for the n^{th} bead (resp. spring). Note that for beads with both adjacent springs in the same region we will see $\alpha_n = \beta_n$, however between regions a bead takes the smaller timestep of the adjacent regions, so we may see $\alpha_n \neq \beta_n$.

The highest resolution model updates time at integer multiples of Δt, i.e. we

	0	$\widetilde{\Delta t}_1$	$2\widetilde{\Delta t}_1$	$3\widetilde{\Delta t}_1$	$4\widetilde{\Delta t}_1$	$5\widetilde{\Delta t}_1$	$6\widetilde{\Delta t}_1$	$7\widetilde{\Delta t}_1$	$8\widetilde{\Delta t}_1$
s_1	•	•	•	•	•	•	•	•	•
s_2	○								○

Table 3.1: *An explanation of the model running on multiple timesteps with region s_1 in twice finer resolution than s_2, giving timesteps 8-times smaller. We run a timestep using equation* (3.32) *for each bead, so that for every timestep we simulate the beads in s_1 and every 8 timesteps for s_2. The force terms $\overline{\boldsymbol{F}}_m^{i\Delta t}$ where bead m is in s_1 is summed over the small timesteps to give $\widetilde{\boldsymbol{F}}_{mn}^{i\Delta t}$ on the larger timesteps using* (3.34)*. We use the same concept to find noise terms $\widetilde{X}_{mn}^{i\Delta t}$.*

compute the polymer state at times $t = i\Delta t$, where $i = 0, 1, 2, 3, \ldots$. Considering the multi-resolution model, we can formally write the update rule (from time $i\Delta t$ to time $(i+1)\Delta t$) for the n^{th} bead, for $n = 1, 2, \ldots, N$, in region α_n as

$$\mathbf{r}_n^{(i+1)\Delta t} = \mathbf{r}_n^{i\Delta t} + Q(s^3_{\alpha_n}, i+1)\left(\widetilde{\boldsymbol{\rho}}_n^{i\Delta t} + \sum_{m=1}^{N} Q(s^3_{\alpha_m}, i+1)\,\mathbf{H}_{nm}\widetilde{\mathbf{F}}_{mn}^{i\Delta t}\right), \tag{3.32}$$

where $\mathbf{H}_{nm}$ is the mobility tensor given in equation (3.9), $\widetilde{\mathbf{F}}_{mn}^{i\Delta t}$ and $\widetilde{\boldsymbol{\rho}}_n^{i\Delta t}$ are discretized force and noise terms given below, and we retain the definition of Q from (2.12). In the update rule (3.32), the timestep is incorporated in the force term. We define the force multiplied by the time step for the m^{th} bead by

$$\overline{\mathbf{F}}_m^{i\Delta t} = \frac{3k_BT}{b_{m-1}^2}\left(\mathbf{r}_{m-1}^{i\Delta t} - \mathbf{r}_m^{i\Delta t}\right)\widetilde{\Delta t}_{\beta_{m-1}} + \frac{3k_BT}{b_m^2}\left(\mathbf{r}_{m+1}^{i\Delta t} - \mathbf{r}_m^{i\Delta t}\right)\widetilde{\Delta t}_{\beta_m}. \tag{3.33}$$

This force term is used as a part of a tension term which includes a memory component for larger timesteps, as explained in Table 3.1:

$$\widetilde{\mathbf{F}}_{mn}^{i\Delta t} = \begin{cases} \overline{\mathbf{F}}_m^{i\Delta t}, & \text{if } s_{\alpha_n} < s_{\alpha_m}, \\ \displaystyle\sum_{p=0}^{(s_{\alpha_n}/s_{\alpha_m})^3-1} \overline{\mathbf{F}}_m^{(i-p)\Delta t}, & \text{otherwise.} \end{cases} \tag{3.34}$$

The random displacement term $\widetilde{\boldsymbol{\rho}}_n$ has a multivariate Gaussian distribution de-

fined by the moments

$$\langle \widetilde{\boldsymbol{\rho}}_n \rangle = 0$$
$$\langle \widetilde{\boldsymbol{\rho}}_m \otimes \widetilde{\boldsymbol{\rho}}_n \rangle = 2k_B T\, \mathbf{H}_{mn} \max(\widetilde{\Delta t}_{\alpha_m}, \widetilde{\Delta t}_{\alpha_n}),$$

where we use the maximum as this term is only expressed on the larger of the two timesteps associated with the beads, as laid out below. To calculate the $\widetilde{\boldsymbol{\rho}}_n$ terms, we use an adapted version of the Ermak-McCammon algorithm [41], so that when we flatten the tensor $\mathbf{H}_{mn}$ into a matrix $\mathbf{H}$, we do so by re-ordering the beads so that beads with smaller timesteps have a smaller index than beads with larger timesteps. Having made this adjustment, we can reduce the computational load of the Cholesky decomposition done by the Ermak-McCammon algorithm (an $\mathcal{O}(N^3)$ calculation [162]), by only calculating the submatrix made up of the rows and columns of the matrix corresponding to beads which are being calculated on that particular timestep. Therefore, if there are N_0 beads which move on a given timestep, then this gives a $3N_0 \times 3N_0$ submatrix.

We use the Cholesky decomposition outlined by Ermak and McCammon [41] to get the lower triagonal matrix $\boldsymbol{B}$, such that $\mathbf{H} = \mathbf{B}\mathbf{B}^{\mathbf{T}}$ with elements given by, for $n = 1, 2, \ldots, 3N_0$,

$$B_{nn} = \left(H_{nn} - \sum_{k=1}^{n-1} B_{nk}^2 \right)^{1/2};$$
$$B_{mn} = \frac{\left(H_{mn} - \sum_{k=1}^{n} B_{mk} B_{nk} \right)}{B_{mm}} \qquad \text{for } m < n, \tag{3.35}$$

to give noise terms $\widetilde{\boldsymbol{\rho}}_n$ with the calculation

$$\widetilde{\rho}_n^{i\Delta t} = \sum_{m=1}^{n} B_{nm} \widetilde{X}_{mn}^{i\Delta t}, \tag{3.36}$$

which are then reordered and formatted to give $\widetilde{\boldsymbol{\rho}}_n$ in a $N_0 \times 3$ matrix. The random terms $\widetilde{X}_{mn}$ now include a 'memory' similar to the tension terms so that

$$\widetilde{X}_{mn}^{i\Delta t} = \begin{cases} X_m^{i\Delta t}, & \text{if } s_{\alpha_n} < s_{\alpha_m}, \\ \sum_{p=0}^{(s_{\alpha_n}/s_{\alpha_m})^3-1} X_m^{(t-p)\Delta t}, & \text{otherwise,} \end{cases} \tag{3.37}$$

for the terms X_m^t drawn from a Gaussian normal distribution such that

$$\begin{aligned} \langle X_m^t \rangle &= 0, \qquad \text{and} \\ \langle X_m^{t_1} X_n^{t_2} \rangle &= 2k_B T \delta_{mn} \Delta t_{\alpha_n} \delta(t_1 - t_2). \end{aligned} \tag{3.38}$$

The approach in this section has been summarized in Algorithm 3.1, which is the method used to conduct the simulations in the next section.

3.4 Simulations

We compare the full BD modelling with the dynamics using the pre-averaged tensor $\langle \mathbf{H}_{mn} \rangle_{\text{eq}}$ from equation (3.13) in place of $\mathbf{H}_{mn}$ in the Ermak-McCammon algorithm given above. Similar to previous papers simulating bead-spring models [103], we choose to simulate with unit parameters, which in our case has $k_B T = 1$ and $\eta = 1$. We shall also hold the rms end-to-end distance constant with $\mu = 1$, which we shall maintain by varying the statistical segment length b as a function of the bead number N as appropriate given the scalings explained in Section 3.2.2. To ensure numerical stability of simulations, we found $\Delta t = 10^{-2} b^3 \eta / k_B T$ to be a good value to use.

In order to study the translational diffusion coefficient in simulations, we need to extend its definition for the simulations of the multi-resolution model. We define the

Calculate the tension forces acting on beads due to move in this timestep:
for $n = 1, 2, \ldots, N$ **do**
  if $s^3_{\alpha_n}|(i+1)$ **then**
    Calculate $\overline{\mathbf{F}}_n^{i\Delta t}$ from (3.33).
  end
end
Calculate the mobility matrix and force contributions on beads due to move in this timestep:
for $n = 1, 2, \ldots, N$ **do**
  for $m = 1, 2, \ldots, N$ **do**
    if $s^3_{\alpha_n}|(i+1)$ and $s^3_{\alpha_m}|(i+1)$ **then**
      Calculate $\mathbf{H}_{nm}$ from (3.9).
      Calculate $\widetilde{\mathbf{F}}_{mn}^{i\Delta t}$ from (3.34).
    end
  end
end
Flatten the tensor $\mathbf{H}$ into a $3N_0 \times 3N_0$ matrix $\widetilde{\mathbf{H}}$.
Calculate the noise contributions on beads due to move in this timestep:
for $n = 1, 2, \ldots, 3N_0$ **do**
  Perform the decomposition (3.35) to form $\mathbf{B}_{nm}$ for $m = 1, 2, \ldots, n$.
  Calculate $X_n^{i\Delta t}$ from (3.38).
  Calculate $\widetilde{X}_{mn}^{i\Delta t}$ from (3.37) for $m = 1, 2, \ldots, n$.
  Calculate $\widetilde{\rho}_n^{i\Delta t}$ from (3.36).
end
Reformulate $\widetilde{\boldsymbol{\rho}}$ in an $N_0 \times 3$ matrix.
Move the beads:
for $n = 1, 2, \ldots, N$ **do**
  Put $\mathbf{r}_n^{(i+1)\Delta t} := \mathbf{r}_n^{i\Delta t}$.
  if $s^3_{\alpha_n}|(i+1)$ **then**
    Put $\mathbf{r}_n^{(i+1)\Delta t} := \mathbf{r}_n^{(i+1)\Delta t} + \widetilde{\boldsymbol{\rho}}_n$.
    for $m = 1, 2, \ldots, N$ **do**
      if $s^3_{\alpha_m}|(i+1)$ **then**
        Put $\mathbf{r}_n^{(i+1)\Delta t} := \mathbf{r}_n^{(i+1)\Delta t} + \mathbf{H}_{nm}\widetilde{\mathbf{F}}_{mn}^{i\Delta t}$.
      end
    end
  end
end

Algorithm 3.1: *One iteration of the numerical algorithm for simulating the multi-resolution bead-spring model from Section* 3.3. *We update positions of beads at time* $t = i\Delta t$ *where* i *is a positive integer. We suppose on this timestep there are* N_0 *beads with the property* $s^3_{\alpha_n}|(i+1)$.

mass of the polymer Ω as

$$\Omega = \sum_{n=1}^{N} \sigma_n^2,$$

where σ_n is the radius of the n^{th} bead, $n = 1, 2, \ldots, N$. Using scalings (3.31), we observe that Ω is invariant to our choice of resolutions in the multi-resolution scheme. This allows us to define the centre of mass of a polymer $\mathbf{r}_G^t$ at time t as

$$\mathbf{r}_G^t = \frac{1}{\Omega} \sum_{n=1}^{N} \mathbf{r}_n^t \sigma_n^2,$$

where $\mathbf{r}_n^t$ is the position of the n^{th} bead at time t. With this we retain the definition of the translational diffusion coefficient from Chapter 2 as (2.7), i.e.

$$D_h = \lim_{t\to\infty} \frac{1}{6t} \langle (\mathbf{r}_G^t - \mathbf{r}_G^0)^2 \rangle. \tag{3.39}$$

For the single scale simulation this reduces to the standard definition for the translational diffusion coefficient.

Note that different definitions for the mass of polymer and the centre of mass are given in (2.8) for the multi-resolution Rouse model. The reason for the selection of the definition for the mass Ω in both chapters is to ensure that is remains constant with the different scalings for σ as discussed in Section 3.2.2. We see in the single-scale modelling that for Rouse dynamics $D_h \sim N^{-1}$ and for Zimm dynamics $D_h \sim N^{-1/2}$ [33] and we choose σ accordingly. We are able to be flexible in how to define the mass of the polymer because the bead radius is not a physically significant quantity, so the interpretation for how this contributes to the overall mass can differ.

In this section we compare the translational diffusion coefficient approximations given in the form of an inverse matrix in equation (3.16) as well as the long chain limit approximation in equation (3.18) to BD simulations for both the full mobility matrix as well as the pre-averaged approximation, as well as the rms end-to-end

N	D_{MF}	D_{PA}	μ_{PA}	$CI_{\mu_{\mathrm{PA}}}$	D_{NPA}	μ_{NPA}	$CI_{\mu_{\mathrm{NPA}}}$
5	0.178	0.187 ± 0.013	0.99	$[0.96, 1.01]$	0.180 ± 0.013	1.00	$[0.96, 1.03]$
10	0.184	0.195 ± 0.015	0.99	$[0.96, 1.03]$	0.185 ± 0.014	1.00	$[0.97, 1.04]$
30	0.189	0.192 ± 0.013	1.00	$[0.97, 1.04]$	0.186 ± 0.013	1.00	$[0.96, 1.03]$
50	0.191	0.202 ± 0.014	1.01	$[0.98, 1.05]$	0.180 ± 0.013	1.01	$[0.97, 1.04]$
100	0.191	0.188 ± 0.013	1.01	$[0.98, 1.05]$	0.174 ± 0.012	1.01	$[0.98, 1.05]$
200	0.192	0.184 ± 0.013	0.99	$[0.96, 1.03]$	0.193 ± 0.014	1.00	$[0.96, 1.04]$

Table 3.2: *Results for diffusion and the rms end-to-end distance in single-scale simulations. The subscript* MF *represents the matrix formulation,* PA *is for pre-averaged and* NPA *is non-pre-averaged. The* 95% *confidence intervals for* μ_{PA} *and* μ_{NPA} *are given by* $CI_{\mu_{\mathrm{PA}}}$ *and* $CI_{\mu_{\mathrm{NPA}}}$*, respectively.*

distance, which has expected value 1 in all simulations by design. We run the BD simulations using both a pre-averaged and a non-pre-averaged mobility tensor for a total of 10^4 timesteps (in the case of multi-resolution simulations, this refers to timesteps associated with the higher resolution beads), where each result is given as an average over 500 runs, and contrast this to the diffusion approximations.

In Tables 3.2 and 3.3 of the results, we include 95% confidence intervals for the translational diffusion coefficient and the rms end-to-end distances. For the end-to-end distance we calculate the 95% confidence interval for $\langle \mathbf{R}^2 \rangle$ and take the square root for both lower and upper bounds to give a range (note that this is not symmetric about the rms value).

We consider three illustrative examples. The first one is a single-scale system, so that $R = 1$ and $s_1 = 1$. We use it as a control to compare the other simulations to. Our results are presented in Figure 3.1 and Table 3.2. As we can see in the table, the matrix formulation D_{MF} is covered within the 95% confidence interval all *except one* of the pre-averaged and non-pre-averaged values of N. The analytic value of $\mu = 1$ fits in the confidence interval for all simulations.

The next system to consider is one in which the middle 25% of the polymer is in

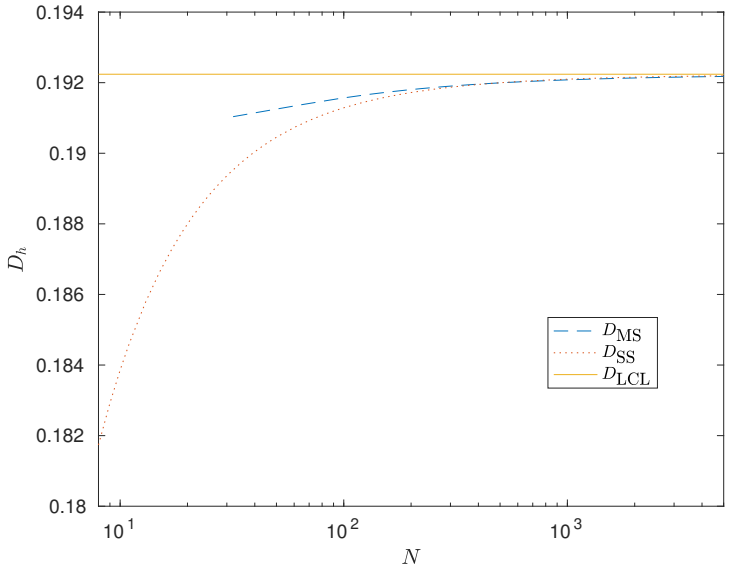


Figure 3.1: *The difference between the matrix formulation for the diffusion coefficient* (3.16) *and the long chain limit* (3.18) *as N gets large, for both the single scale-system (red dotted line) and the multiscale simulation, which has the middle 25% of the polymer in high resolution (blue dashed line). Parameters are given in Section* 3.4. *Note that the multi-scale system needs $N \geq 32$ by construction for the coarse grained particles to be placed.*

high resolution, while the remainder is coarse-grained by a factor of 2. Therefore we define $R = 3$ with $s_1 = 2$, $s_2 = 1$, $s_3 = 2$, and $N_1 = 3N/8$, $N_2 = N/4$, $N_3 = 3N/8$. The diffusion and the rms end-to-end distance of this polymer is given in Table 3.3. The matrix formulation for the diffusion D_{MF} is contained in the confidence intervals for all values of N, and the value of $\mu = 1$ is contained in the confidence interval for all values of N. The convergence of matrix formulation to the long chain limit is shown in Figure 3.1.

The final system considered had an 8-times resolution increase in the middle 10% of the the polymer. This uses $R = 3$ with $s_1 = 8$, $s_2 = 1$, $s_3 = 8$, and $N_1 = 9N/20$, $N_2 = N/10$, $N_3 = 9N/20$. We perform the simulation for $N = 1280$, from which we can report $D = 0.189$, $\mu = 1.04$ for the pre-averaged case and $D = 0.180$, $\mu = 1.01$ where we do not use pre-averaging. The matrix formulation for the translational diffusion coefficient gives a value $D_{\mathrm{MF}} = 0.190$. The end-to-end distance in the pre-

averaged case falls outside of the 95% confidence interval, but the other three statistics lie within this range.

As can be seen from the simulations, there is good agreement both between the pre-averaged and non pre-averaged tensors, as well as between the diffusion approximations and the results from the simulations. In total out of 44 observations, we had two falling outside of the 95% confidence interval. The overall goal of doing this coarse-graining is to improve the speed of simulations. In Figure 3.2, we compared the timings between the single-scale and multi-scale models for identical parameters as were used to produce Table 3.3. There is a pronounced difference between the multi-scale model and single-scale model without pre-averaging, most of which comes from having to use the Cholesky decomposition on smaller matrices, while the smaller difference in the model with pre-averaging comes from updating fewer beads in each timestep.

There are different situations in which it would be useful to use the pre-averaging approach for simulations and other situations where it would be better to use the full multiscale method. It has been long known that pre-averaging the mobility matrix results in a miscalculation in intrinsic viscosity and other rheological properties due to a non-vanishing second normal stress difference [145, 203]. Therefore, for simulations where these properties of the polymer are important, and computational efficiency is less of an issue, then using the full hydrodynamic interaction tensor would be more appropriate. However, if speed is more important then there can be significant gains from taking the pre-averaged approximation. More study would be needed on the effect of multi-resolution modelling on the errors introduced by taking the pre-averaging approach.

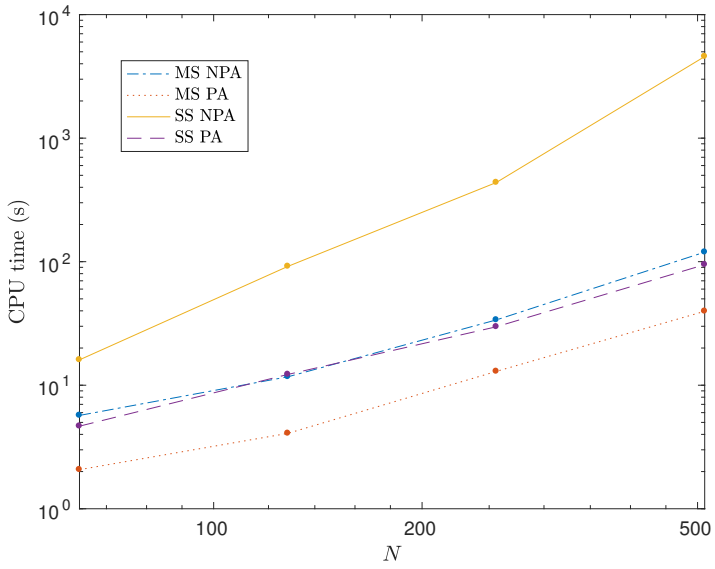


Figure 3.2: *The* CPU *times to simulate identical systems using four different algorithms: the multi-scale model using pre-averaging (red dotted line), the single-scale model with pre-averaging (purple dashed line), the multi-scale model without pre-averaging (blue dot-dashed line) and the single-scale model without pre-averaging (yellow solid line).*

N	D_{MF}	D_{PA}	μ_{PA}	$CI_{\mu_{\mathrm{PA}}}$	D_{NPA}	μ_{NPA}	$CI_{\mu_{\mathrm{NPA}}}$
32	0.191	0.183 ± 0.013	0.99	$[0.95, 1.02]$	0.189 ± 0.013	1.02	$[0.98, 1.05]$
64	0.191	0.195 ± 0.013	0.99	$[0.95, 1.02]$	0.186 ± 0.014	0.99	$[0.96, 1.03]$
128	0.192	0.185 ± 0.014	1.00	$[0.96, 1.04]$	0.192 ± 0.013	1.00	$[0.97, 1.04]$
256	0.192	0.186 ± 0.013	1.00	$[0.96, 1.03]$	0.184 ± 0.014	0.98	$[0.94, 1.01]$

Table 3.3: *Results for diffusion and the rms end-to-end distance in multi-resolution simulations, which have the middle* 25% *of the polymer in high resolution. Subscripts are the same as in Table* 3.2. *Simulations run for* 10^4 *timesteps for beads at the highest resolution.*

3.5 Discussion

In this chapter we have extended the bead-spring model for a polymer including HI to a multi-resolution model in order to gain computational efficiency for BD modelling. By considering a multi-resolution GC model, we have utilized the Boltzmann distribution in order to form a diffusive displacement equation for the multi-resolution model. From this we used a similar approach to Öttinger [130] in order to derive an integral equation for the diffusion of the polymer using the pre-averaging approximation, which was then manipulated to find a closed form equation for the diffusion in the long chain limit. This gave scaling laws (3.31) for key parameters of the polymer at different scales. The developed multi-resolution approach keeps the rms end-to-end distance and the translational diffusion coefficient invariant to the choices of how we split the polymer up into different resolutions. These scaling laws have then been supported by illustrative simulations, which used an adapted version of the Ermak-McCammon algorithm [41].

The intention the work contained in this chapter is to act as a stepping stone towards a more full multi-resolution approach to be applied to BD models for polymers, incorporating more detailed and accurate models for a polymer as well as faster algorithms, both of which have seen a large volume of research in the past 30 years as discussed in Section 1.3. We have used the Hookean potential (3.11) between beads due to its mathematical tractability, and the numerical method as it was one of the first presented. Both of these approaches could be improved upon in future work.

The use of a Hookean potential between beads allows us to describe the inter-bead distances in terms of a Gaussian, which makes it much mathematically easier to analyze. This can introduce unrealistic features, for example the linear force as the length of the spring gets very long, which can be addressed by extending the model to the FENE spring [15]. There are also more elaborate potentials introduced for specific modelling of DNA on mesoscopic scales in the literature as discussed in

Chapter 1 [54, 84, 159, 167]. A further extension of this work could be to extend these models to a corresponding multi-resolution approach, similar to the multi-resolved polymer chain of Pasquale-Carbone [32], or even to introduce a hybrid model where different models are combined between regions. Due to the intractability of these more advanced potentials, in order to maintain macro-scale quantities a numerical approach would be necessary. We believe that our approach could also be extended to include EV interactions which were discussed in Section 1.3.

It is imagined that in order to include either more advanced potentials or EV interactions would involve a computer-assisted parameter search for each region of the polymer to investigate how properties of interest scale. Computational explorations of multi-region polymer models would then be used to select an appropriate mechanism to glue the different regions of the polymer together in one dynamical multi-resolution simulation.

There have also been many developments in the algorithms which are used to study polymers with hydrodynamic interactions [6, 45, 52, 117]. Many of these algorithms operate with approximations allowing them to run in $\mathcal{O}(N)$ time [35,67] which would decrease computational gains from the multi-resolution concept, but as an approach, the multi-resolution bead-spring model would still be important for reducing computation time, particularly in situations where there are large differences in the temporal and spatial scales of the system. It is hoped that these could, in theory, be extended to multi-resolution modelling using a similar approach to the one taken in this chapter.

Chapter 4

Investigating Steady States of Confined Nematic Liquid Crystal Systems in Two Dimensions

The work contained in Chapter 4 was conducted in the final two terms of the DPhil beginning in January 2018 in collaboration with Apala Majumdar and supervised by Radek Erban. This work may provide a foundation to a future paper to be submitted to Physical Review E.

As discussed in Section 1.7, there has been much work on modelling confined systems of NLC molecules following discoveries of multiple steady states in experiments [100, 184], which was followed up with various modelling approaches [88, 110, 156]. This chapter looks to build upon this work by using a BD approach using the GB potential. This results in stochastic equations of motion similar to those seen in Chapter 2 and Chapter 3, solved using the EM numerical scheme with Dirichlet boundary conditions. In this chapter, a method is developed to generate both random and LdG suggested equilibria. A scalar comparison parameter is proposed to compare the steady states suggested from LdG modelling by Robinson et al. [156] to

simulations.

Simulations are used to study two key questions. Firstly, whether it is possible to equilibriate to the LdG suggested steady states from a random initial configuration under different parameter regimes. Secondly, if we start a system in a particular equilibrium suggested by LdG modelling, whether this state is stable under different parameters when we run the BD modelling.

This chapter is arranged with the methods used to run the simulations described in Section 4.1, with the results given in Section 4.2 and a discussion about what the results show as well as future directions in Section 4.3.

4.1 Methods

The following simulations have been developed using the potential originally developed by Gay and Berne [50], coupled with the equations of motion outlined in [119, 197, 198], which have been adapted from three-dimensions for our simulations which are in two dimensions. We have adapted the Metropolis Hastings MCMC off-lattice approach for Dirichlet boundary conditions from Robinson et al. [156] to BD simulations. We also use similar parameters for the GB potential and domain size in order to aid comparisons. Normalization of the unit orientation vector and forms for the differential equations of the potential were adapted from [109]. The simulations are made using the Aboria library [155] in C++, which is a package for efficient neighborhood searching queries in particle simulations. This significantly speeds up the pairwise interaction calculations made with the GB potential.

In these simulations we have N NLC molecules of uniform width σ_s and length σ_e held inside a square with side length K. We define the molecular aspect ratio $\kappa = \sigma_e/\sigma_s$. In all simulations, we take $\sigma_s = 0.5\,\text{nm}$, the same as [156], and calculate the number of molecules inside the domain to be a function of the average dimensionless

density ρ, so that $N = K^2\sigma_s^{-2}\rho$.

Each particle has associated with it a position $\mathbf{r}_n$ and a unit orientation vector $\mathbf{u}_n$, which is notation that shall be used throughout this section. In this work we are only concerned with two dimensions, so that $\mathbf{r}_n \in \mathbb{R}^2$ and $\mathbf{u}_n \in \mathbb{S}^1$, where $\mathbb{S}^1$ is the unit circle.

4.1.1 Gay-Berne Potential

The GB potential used for pairwise interactions between NLC molecules is identical to the one proposed by Gay and Berne [50]. Let us suppose that $\mathbf{r}_{mn}$ denotes the vector between particles n and m, so that $\mathbf{r}_{mn} = \mathbf{r}_n - \mathbf{r}_m$ with distance between particles $r_{mn} = |\mathbf{r}_{mn}|$ and unit vector $\hat{\mathbf{r}}_{mn} = \mathbf{r}_{mn}/r_{mn}$. Then we introduce the shape parameter σ as

$$\sigma(\mathbf{u}_n, \mathbf{u}_m, \hat{\mathbf{r}}_{mn}) = \sigma_s \left\{ 1 - \frac{\chi}{2} \left[\frac{(\mathbf{u}_n \cdot \hat{\mathbf{r}}_{mn} + \mathbf{u}_m \cdot \hat{\mathbf{r}}_{mn})^2}{1 + \chi(\mathbf{u}_n \cdot \mathbf{u}_m)} + \frac{(\mathbf{u}_n \cdot \hat{\mathbf{r}}_{mn} - \mathbf{u}_m \cdot \hat{\mathbf{r}}_{mn})^2}{1 - \chi(\mathbf{u}_n \cdot \mathbf{u}_m)} \right] \right\}^{-1/2}, \tag{4.1}$$

where χ is a constant related to the molecular aspect ratio by

$$\chi = \frac{\kappa^2 - 1}{\kappa^2 + 1}. \tag{4.2}$$

We can then introduce the GB potential between particles n and m as

$$U_{GB}(\mathbf{u}_n, \mathbf{u}_m, \hat{\mathbf{r}}_{mn}) = 4\mathcal{E}(\mathbf{u}_n, \mathbf{u}_m, \hat{\mathbf{r}}_{mn}) \left[q^{12}(\mathbf{u}_n, \mathbf{u}_m, \hat{\mathbf{r}}_{mn}) - q^6(\mathbf{u}_n, \mathbf{u}_m, \hat{\mathbf{r}}_{mn}) \right], \tag{4.3}$$

where $\mathcal{E}(\mathbf{u}_n, \mathbf{u}_m, \hat{\mathbf{r}}_{mn})$ gives an energetic contribution and the $q(\mathbf{u}_n, \mathbf{u}_m, \hat{\mathbf{r}}_{mn})$ terms give a LJ type contribution where

$$q(\mathbf{u}_n, \mathbf{u}_m, \hat{\mathbf{r}}_{mn}) = \frac{\sigma_s}{r_{mn} - \sigma(\mathbf{u}_n, \mathbf{u}_m, \hat{\mathbf{r}}_{mn}) + \sigma_s}. \tag{4.4}$$

The energy term written as

$$\mathcal{E}(\mathbf{u}_n, \mathbf{u}_m, \hat{\mathbf{r}}_{mn}) = \mathcal{E}^{\nu}(\mathbf{u}_n, \mathbf{u}_m)\mathcal{E}'^{\mu}(\mathbf{u}_n, \mathbf{u}_m, \hat{\mathbf{r}}_{mn}), \tag{4.5}$$

where μ and ν are constants and

$$\mathcal{E}(\mathbf{u}_n, \mathbf{u}_m) = (1 - \chi^2(\mathbf{u}_n \cdot \mathbf{u}_m)^2)^{-1/2}, \tag{4.6}$$

$$\mathcal{E}'(\mathbf{u}_n, \mathbf{u}_m, \hat{\mathbf{r}}_{mn}) = 1 - \frac{\chi'}{2}\left[\frac{(\mathbf{u}_n \cdot \hat{\mathbf{r}}_{mn} + \mathbf{u}_m \cdot \hat{\mathbf{r}}_{mn})^2}{1 + \chi'(\mathbf{u}_n \cdot \mathbf{u}_m)} + \frac{(\mathbf{u}_n \cdot \hat{\mathbf{r}}_{mn} - \mathbf{u}_m \cdot \hat{\mathbf{r}}_{mn})^2}{1 - \chi'(\mathbf{u}_n \cdot \mathbf{u}_m)}\right], \tag{4.7}$$

where χ' is a constant given in terms of the well-depth ratio κ' for end-to-end and side-by-side configurations:

$$\chi' = \frac{\kappa'^{1/\mu} - 1}{\kappa'^{1/\mu} + 1}. \tag{4.8}$$

This gives four parameters $\kappa, \kappa', \mu, \nu$ to tune the GB potential. In all simulations, these shall take the values $(\kappa, \kappa', \mu, \nu) = (3, 5, 1, 3)$, which is commonly used in the literature [156] as they have been used to replicate phase transitions observed in liquid crystal experiments [12]. A schematic of the behaviour of the GB potential for different configurations of two particles approaching each other is given in Figure 4.1.

4.1.2 Equations of Motion

In order to derive equations of motion, we follow the approach of using non-equilibrium Brownian dynamics (NEBD) similar to [119]. These give the following equations for translational and rotational motion with respect to the centre of mass for particle n:

$$\mathbf{F}_n^{GB} - \mathbf{F}_n^{V} + \mathbf{F}_n^{B} = \mathbf{0} \tag{4.9}$$

$$\mathbf{T}_n^{GB} - \mathbf{T}_n^{V} + \mathbf{T}_n^{B} = \mathbf{0}, \tag{4.10}$$

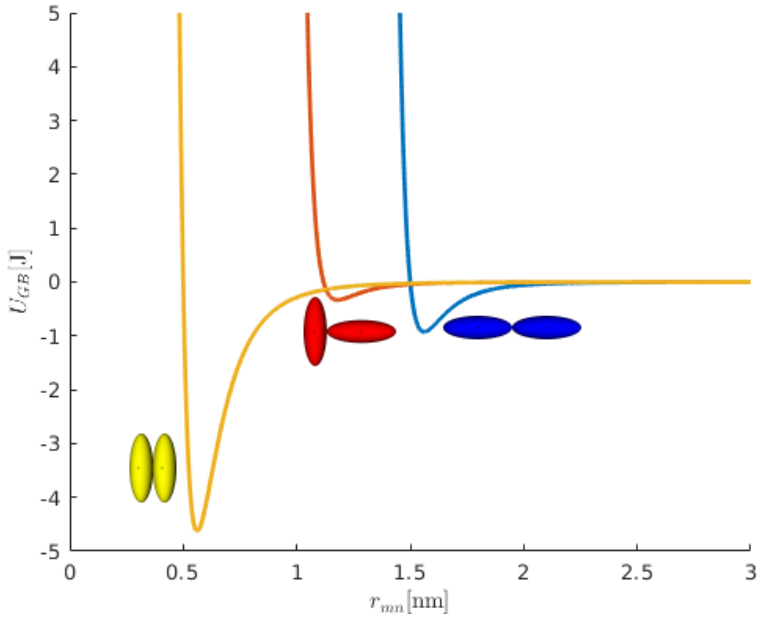


Figure 4.1: *For three different two-molecule configurations we plot the behaviour of the* GB *potential as a function of the distance between the two molecules. Yellow gives the two molecules in a side-by-side configuration, red for a front-to-side configuration and blue for a front-to-front configuration. Parameters used are* $\sigma_s = 0.5\,\text{nm}$ *and* $(\kappa, \kappa', \mu, \nu) = (3, 5, 1, 3)$. *Figure made using* VTK [168].

where the superscripts GB, V and B give contributions from GB inter-particle interactions, viscous drag and Brownian motion respectively, affecting force $\mathbf{F}$ and torque $\mathbf{T}$.

The GB contribution to the force $\mathbf{F}_n^{GB}$ and torque $\mathbf{T}_n^{GB}$ is found by summing over the pairwise interactions of all neighbouring particles within a certain cutoff radius r_c in the interests of computational efficiency as the contribution tends to zero as inter-particle distance gets large as seen in Figure 4.1. In our simulations we let this cutoff radius be given by $r_c = 6\sigma_e$, so that

$$\begin{aligned} \mathbf{F}_n^{GB} &= \sum_{\substack{m \neq n \\ r_{mn} < r_c}} \mathbf{F}_{mn}^{GB}; \\ \mathbf{T}_n^{GB} &= \sum_{\substack{m \neq n \\ r_{mn} < r_c}} \mathbf{T}_{mn}^{GB}, \end{aligned} \tag{4.11}$$

where the pairwise interaction terms are given by [109]

$$\begin{aligned}\mathbf{F}_{mn}^{GB} &= -\frac{\partial U_{GB}}{\partial \hat{\mathbf{r}}_n}(\mathbf{u}_n, \mathbf{u}_m, \hat{\mathbf{r}}_{mn});\\ \mathbf{T}_{mn}^{GB} &= -\mathbf{u}_n \times \frac{\partial U_{GB}}{\partial \hat{\mathbf{u}}_n}(\mathbf{u}_n, \mathbf{u}_m, \hat{\mathbf{r}}_{mn}).\end{aligned} \tag{4.12}$$

The Brownian forces are assumed to be Gaussian and are given with respect to the primary axis. We use the superscript $||$ to denote action parallel to the major axis and $\perp$ for perpendicular. These are found from Gaussian distributions defined by the moments [198]

$$\begin{aligned}\langle \mathbf{F}^{B||} \rangle = 0 \quad &, \quad \langle \mathbf{F}^{B||} \cdot \mathbf{F}^{B||} \rangle = \frac{2\zeta_t^{||} k_B T}{\Delta t},\\ \langle \mathbf{F}^{B\perp} \rangle = 0 \quad &, \quad \langle \mathbf{F}^{B\perp} \cdot \mathbf{F}^{B\perp} \rangle = \frac{2\zeta_t^{\perp} k_B T}{\Delta t},\\ \langle \mathbf{T}^{B||} \rangle = 0 \quad &, \quad \langle \mathbf{T}^{B||} \cdot \mathbf{T}^{B||} \rangle = \frac{2\zeta_r^{||} k_B T}{\Delta t},\\ \langle \mathbf{T}^{B\perp} \rangle = 0 \quad &, \quad \langle \mathbf{T}^{B\perp} \cdot \mathbf{T}^{B\perp} \rangle = \frac{2\zeta_r^{\perp} k_B T}{\Delta t};\end{aligned} \tag{4.13}$$

where k_B is Boltzmann's constant and T is the absolute temperature. Translational and angular friction constants are given by [76]

$$\begin{aligned}\zeta_t^{||} &= 3\pi\eta_s\sigma_e X^A;\\ \zeta_t^{\perp} &= 3\pi\eta_s\sigma_e Y^A;\\ \zeta_r^{||} &= \pi\eta_s\sigma_e^3 X^C;\\ \zeta_r^{\perp} &= \pi\eta_s\sigma_e^3 Y^C,\end{aligned} \tag{4.14}$$

where η_s is the solvent viscosity, and the resistance functions X^A, Y^A, X^C and Y^C are functions of the eccentricity of the NLC molecules $s = \sqrt{1-\kappa^{-2}}$. These are given

by [166]

$$
\begin{aligned}
X^A &= \frac{4s^3}{3\left(\left(2s^2-1\right)Q + s\sqrt{1-s^2}\right)};\\
Y^A &= \frac{8s^3}{3\left(\left(2s^2+1\right)Q - s\sqrt{1-s^2}\right)};\\
X^C &= \frac{2s^3}{3\left(Q - s\sqrt{1-s^2}\right)};\\
Y^C &= -\frac{2s^3(2-s^2)}{3\left(s\sqrt{1-s^2} - \left(1-2s^2\right)Q\right)},
\end{aligned}
\tag{4.15}
$$

for

$$
Q = \cot^{-1}\frac{\sqrt{1-s^2}}{s}. \tag{4.16}
$$

The shear force $\mathbf{F}_n^V$ and torque $\mathbf{T}_n^V$ are given by [76, 119]

$$
\mathbf{F}_n^V = 3\pi\sigma_e\eta_s\left\{X^A(\mathbf{u}_n(t)\otimes\mathbf{u}_n(t)) + Y^A\left[\mathbf{I} - (\mathbf{u}_n(t)\otimes\mathbf{u}_n(t))\right]\right\}\cdot\mathbf{v}_n \tag{4.17}
$$

$$
\mathbf{T}_n^V = \pi\sigma_e^3\eta_s\left\{X^C(\mathbf{u}_n(t)\otimes\mathbf{u}_n(t)) + Y^C\left[\mathbf{I} - (\mathbf{u}_n(t)\otimes\mathbf{u}_n(t))\right]\right\}\cdot\boldsymbol{\omega}_n, \tag{4.18}
$$

where $\mathbf{v}_n$ and $\boldsymbol{\omega}_n$ are the translational and angular velocity vectors for the n^{th} particle respectively, and we have assumed that the translational velocity and angular velocity vectors for the background fluid are equal to zero, as well as a zero rate of deformation tensor.

4.1.3 Numerical Scheme

In order to solve for position $\mathbf{r}_n$ and orientation $\mathbf{u}_n$, we apply the EM numerical scheme [83]. Here we discretize the time points to be multiples of some timestep Δt, and make the approximations for translational and angular velocity for small

timesteps at time t:

$$\mathbf{v}_n(t) \approx \frac{\mathbf{r}_n(t+\Delta t) - \mathbf{r}_n(t)}{\Delta t};$$
$$\boldsymbol{\omega}_n(t) \approx \frac{\mathbf{u}_n(t+\Delta t) - \mathbf{u}_n(t)}{\Delta t}.$$

If we let

$$\mathbf{M}_n^{tr}(t) = 3\pi\sigma_e\eta_s \left\{X^A(\mathbf{u}_n(t)\otimes\mathbf{u}_n(t)) + Y^A\left[\mathbf{I} - (\mathbf{u}_n(t)\otimes\mathbf{u}_n(t))\right]\right\};$$
$$\mathbf{M}_n^{ang}(t) = \pi\sigma_e^3\eta_s \left\{X^C(\mathbf{u}_n(t)\otimes\mathbf{u}_n(t)) + Y^C\left[\mathbf{I} - (\mathbf{u}_n(t)\otimes\mathbf{u}_n(t))\right]\right\}, \tag{4.19}$$

then we can rearrange (4.9) and (4.10) to form the matrix equation for the system at $t+\Delta t$ given the state at t from the EM algorithm:

$$\mathbf{M}_n^{tr}(t)\cdot\mathbf{r}_n(t+\Delta t) = \mathbf{M}_n^{tr}(t)\cdot\mathbf{r}_n(t) + \Delta t\left(\mathbf{F}_n^{GB}(t) + \mathbf{F}_n^{B}(t)\right); \tag{4.20}$$
$$\mathbf{M}_n^{ang}(t)\cdot\mathbf{u}_n(t+\Delta t) = \mathbf{M}_n^{ang}(t)\cdot\mathbf{u}_n(t) + \Delta t\left(\mathbf{T}_n^{GB}(t) + \mathbf{T}_n^{B}(t)\right). \tag{4.21}$$

We calculate the Brownian motion terms $\mathbf{F}_n^B$ and $\mathbf{T}_n^B$ at time t with timestep Δt with the equations

$$\mathbf{F}_n^B = \mathbf{F}_n^{B\parallel} + \mathbf{F}_n^{B\perp}, \qquad \mathbf{T}_n^B = \mathbf{T}_n^{B\parallel} + \mathbf{T}_n^{B\perp};$$
$$\text{where}\quad \mathbf{F}_n^{B\parallel} = \sqrt{\frac{2\zeta_t^{\parallel}k_BT}{\Delta t}}\xi_t^{\parallel}\mathbf{u}_n, \qquad \mathbf{F}_n^{B\perp} = \sqrt{\frac{2\zeta_t^{\perp}k_BT}{\Delta t}}\xi_t^{\perp}\hat{\mathbf{n}}_n;$$
$$\text{and}\quad \mathbf{T}_n^{B\parallel} = \sqrt{\frac{2\zeta_r^{\parallel}k_BT}{\Delta t}}\xi_r^{\parallel}\mathbf{n}_n, \qquad \mathbf{F}_n^{B\perp} = \sqrt{\frac{2\zeta_r^{\perp}k_BT}{\Delta t}}\xi_r^{\perp}\hat{\mathbf{n}}_n, \tag{4.22}$$

where $\hat{\mathbf{n}}_n$ is the unit normal to the orientation vector and $\xi_r^{\parallel}$, $\xi_r^{\perp}$, $\xi_t^{\parallel}$, $\xi_t^{\perp}$ are separately drawn from the standard normal distribution.

We also need to maintain orientation vectors $\mathbf{u}_n$ as unit vectors by adding a 'corrector' step at the end of each timestep to each particle, identical to the one used

by Luckhurst et al [109].

We suppose that the orientation vector at time t, $\hat{\mathbf{u}}_n(t)$, is a unit vector, which gives a vector $\mathbf{u}_n(t+\Delta t)$ following the numerical scheme in (4.21), which is in general not a unit vector. We apply a force of magnitude λ to the n^{th} particle orientation at time t parallel to the major axes such that the new orientation vector $\hat{\mathbf{u}}_n(t+\Delta t)$ given by

$$\hat{\mathbf{u}}_n(t+\Delta t) = \mathbf{u}_n(t+\Delta t) + \hat{\mathbf{u}}_n(t)\frac{\lambda}{2\omega}\Delta t^2 \tag{4.23}$$

is a unit vector [109]. Here, ω is an arbitrary constant mass on which the force acts, so we can write a new dimensionless constant for the force given by λ' to give the equation for orientation vector

$$\hat{\mathbf{u}}_n(t+\Delta t) = \mathbf{u}_n(t+\Delta t) + \lambda'\hat{\mathbf{u}}_n(t). \tag{4.24}$$

To find λ', we take the scalar product of each side of (4.24) with itself to give a quadratic in λ'

$$1 = \mathbf{u}_n(t+\Delta t)\cdot\mathbf{u}_n(t+\Delta t) + 2\lambda'\hat{\mathbf{u}}_n(t)\cdot\mathbf{u}_n(t+\Delta t) + \lambda'^2, \tag{4.25}$$

using the property that $\hat{\mathbf{u}}_n(t)$ is a unit vector.

This quadratic has solution:

$$\lambda' = -\hat{\mathbf{u}}_n(t)\cdot\mathbf{u}_n(t+\Delta t) + \sqrt{(\hat{\mathbf{u}}_n(t)\cdot\mathbf{u}_n(t+\Delta t))^2 - (\mathbf{u}_n(t+\Delta t)\cdot\mathbf{u}_n(t+\Delta t)) + 1}, \tag{4.26}$$

where we have taken the positive sign in the quadratic formula to get a smaller value for $|\lambda'|$. If this process is followed for sufficiently small timesteps, then we ensure that the orientation vector remains a unit vector.

4.1.4 Boundary Conditions

We take a similar approach to the one taken in Robinson et al. [156] for off-lattice models to prescribe the boundary conditions for the system, where a molecular version of Dirichlet boundary conditions are imposed. This is modelled by a line of static NLC molecules laid end-to-end along their major axes to form a boundary, with position and orientation fixed in time. The number of particles N_{BDY} along each co-ordinate axis is given by the equation

$$N_{\mathrm{BDY}} = \left\lfloor \frac{K}{\sigma_e} \right\rfloor, \tag{4.27}$$

where the symbol $\lfloor x \rfloor$ indicates the floor function, rounding down to the greatest integer less than or equal to x.

These particles do not count towards the overall particle count, and do not move or rotate, but are included in the GB contributions to forces applied to the internal particles. In all simulations, no particles were able to break through this chain of particles which form the boundary.

4.1.5 Nematic Equilibria

To both generate an NLC system with LdG-suggested nematic equilibria initial conditions, as well as to have a quantitative measure comparing these simulations to LdG equilibria computed in [156], we need to generate ideal versions of each of the nematic equilibria. The three states studied are the rotated solution and the diagonal solution, both first reported by Tsakonas et al. [184], as well as the WORS steady state first found by Kralj and Majumdar [88]. The method to generate these three steady states will be identical to the LdG approach provided by Robinson et al. [156], using an adapted version of the code provided for the paper from Github (`https://github.com/martinjrobins/liquid_crystals`). Here we will give an overview of the method used by Robinson et al. [156], but for a more rigorous and

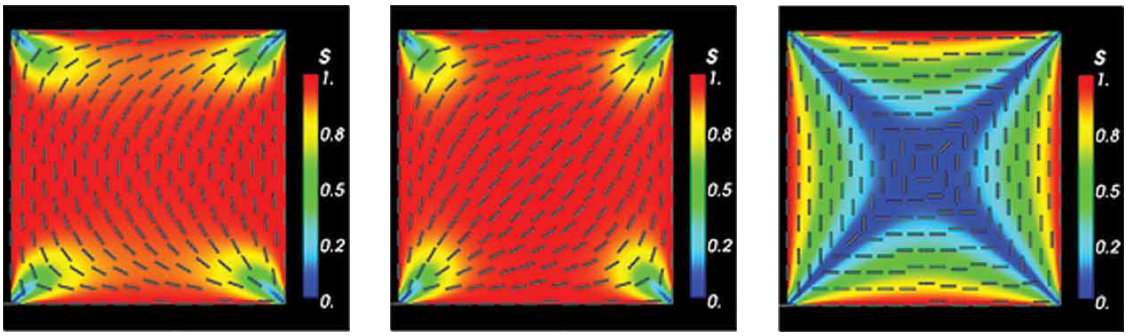
detailed treatment this can be found in their paper.

This work uses a variational method to compute equilibria corresponding to minimizers of a simple form of the LdG energy [156, 187] given by

$$\mathcal{E}_{\mathrm{LDG}}\left[\mathbf{Q}\right] = \int\limits_{(x,y)\in[0,K]^2} w_e\left(\nabla\mathbf{Q}\right) + w_b\left(\mathbf{Q}\right)\mathrm{dA}, \tag{4.28}$$

for $w_e\left(\nabla\mathbf{Q}\right)$ the one-constant elastic energy density and $w_b\left(\mathbf{Q}\right)$ a non-convex bulk potential where $\mathbf{Q}$ is the two-dimensional Q-tensor, which is introduced in (1.17). There is a more extensive study by Luo et al. [110] for different forms that the energy and potential terms can take. We then fix constants associated with these two terms and vary the domain size K to give the steady states. Dirichlet boundary conditions are given with suitable initial conditions [110]. Using the FEniCS package [4, 108], we can generate six solutions on a mesh of size 100×100 for each value of K. These solutions are named D1, D2, R1, R2, R3 and R4. For a value of $K = 1.2\mu$m, D1–D2 are associated with the diagonal solution, with D2 a rotated version of D1, and R2–R4 are rotated versions of R1, which is associated with the rotated solution. For a value of $K = 0.1\mu$m we find all six solutions are the WORS solution. These solutions are shown in Figure 4.2. Note that results between the variational method and the BD simulations are not directly comparable for the same values of K as the parameters of the variational model are not equivalent to the parameters used in the BD modelling.

From the 100×100 grid this gives the orientation of the LdG solution at discrete points on a fine scale. This forms a *reference grid* which will be used to generate initial conditions for specified equilibria in Section 4.1.6, as well as to enable us to compare states of the system to equilibria during simulations in Section 4.1.7.



(a) Diagonal solution D1 (b) Rotated solution R1 (c) WORS solution

Figure 4.2: *The three different nematic equilibria studied in* Chapter 4*, found using domain size* $K = 1.2\mu$m *for the rotated and diagonal solutions, and* $K = 0.1\mu$m *for the WORS solution. Each plot shows the nematic director at each point on a grid and the scalar order parameter* S*. Adapted from* [156] *under the Creative Commons Attribution License.*

4.1.6 Initial Conditions

To form initial conditions for the system, we need to devise a mechanism such that there are not significant overlaps between particles at the beginning of simulations, as this is outside the scope of what the GB potential is designed to model. To start naively in random initial conditions, we would certainly see significant overlaps. To create a system in one of the LdG equilibria, it might be possible to manually create a system similar to the desired form, but this would require a significant amount of effort to stack molecules without overlaps due to their ellipsoidal shape, and would not be a systematic approach. It would also be likely to result in large spikes in GB contributions when the real simulation starts as it would still lie away from equilibrium.

We instead take an approach where we start with all particles small, and gradually increase their size during an initial phase of the BD simulation, so that we do not see large overlaps occurring as these are prevented by the GB potential. This process is described as *growing* the system. This initial phase is done in a deterministic system without Gaussian noise, so we set temperature $k_BT = 0\,\mathrm{J}$, while keeping the domain size constant. As the aspect ratio κ is held constant, we gradually increase the particle

width σ_s of the internal particles which results in the particle length σ_e growing at the same rate.

To grow the system over the course of time t_{grow}, if we denote the current particle width with $\bar{\sigma}_s$, growing to a size of σ_s then we set the width with

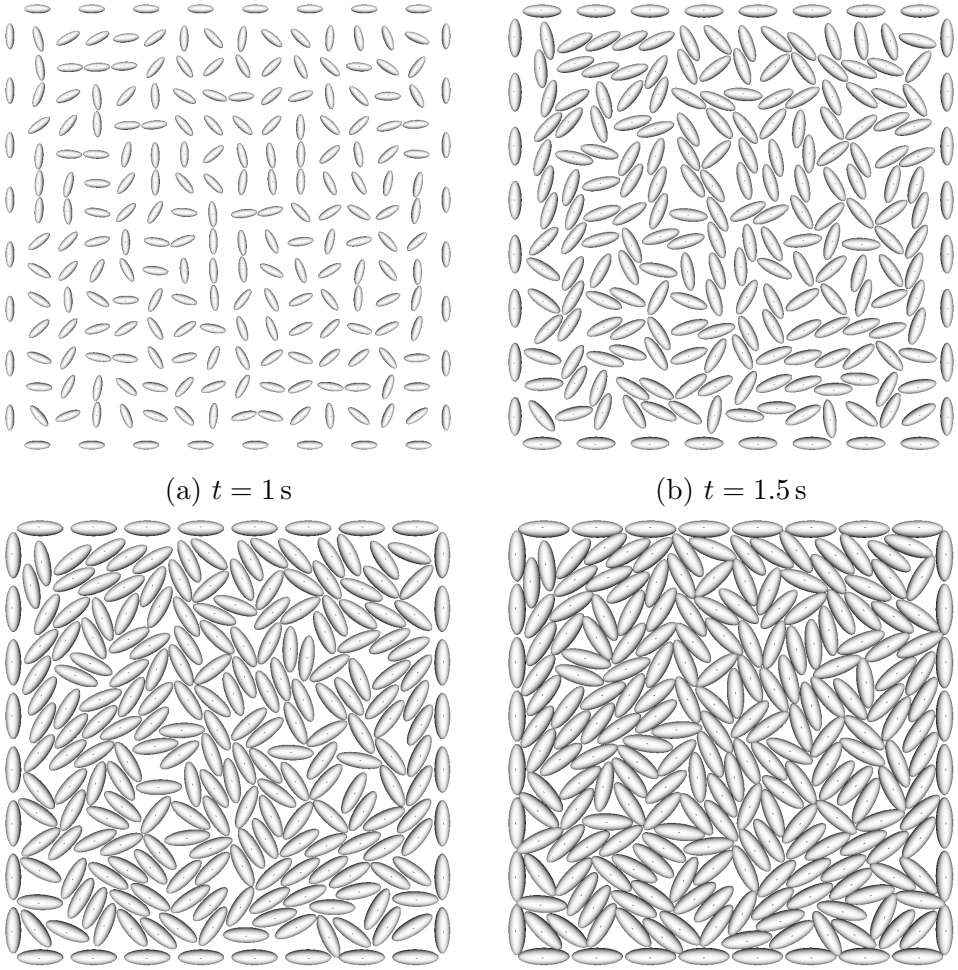
$$\bar{\sigma}_s = 0.001\sigma_s + 0.999\sigma_s \frac{t}{t_{grow}}, \tag{4.29}$$

where t is the current time for the simulation. We choose the width in such a way to ensure a non-zero particle size at $t = 0\,\mathrm{s}$. We then run the system with (4.20) and (4.21) as before, but using the value $\bar{\sigma}_s$ for the width of a particle and $\bar{\sigma}_e = \kappa\bar{\sigma}_s$ as the particle length. An illustrative example for the method of growing a system is given in Figure 4.3. As can be seen in Figure 4.3, the boundary beads also start small and grow which results in boundary gaps during the growth process, but in the absence of noise and the GB repulsion occurring only at small inter-particle distances, we do not see particles exiting the domain, which has been confirmed by our simulations.

To place the molecules in their initial configurations, we form an evenly spaced grid inside the domain with N_K molecules in each row and column. In most simulations, we have chosen domain size K and density ρ to be such that the $N_K^2 = N$, the total number of molecules in the system, but where $N_K^2 > N$, we remove uniformly at random the required number of molecules to give N total.

In this work we study four initial configurations for the system: a random initial configuration and the three nematic equilibria discussed in Section 4.1.5. To generate the random configuration, each molecule is placed on the $N_K \times N_K$ grid and given an angle uniformly at random on the unit circle, which is converted into an orientation vector.

To generate in a nematic equilibrium, for each molecule we look at the reference grid for the steady state and find the nearest point on the grid to the molecule in



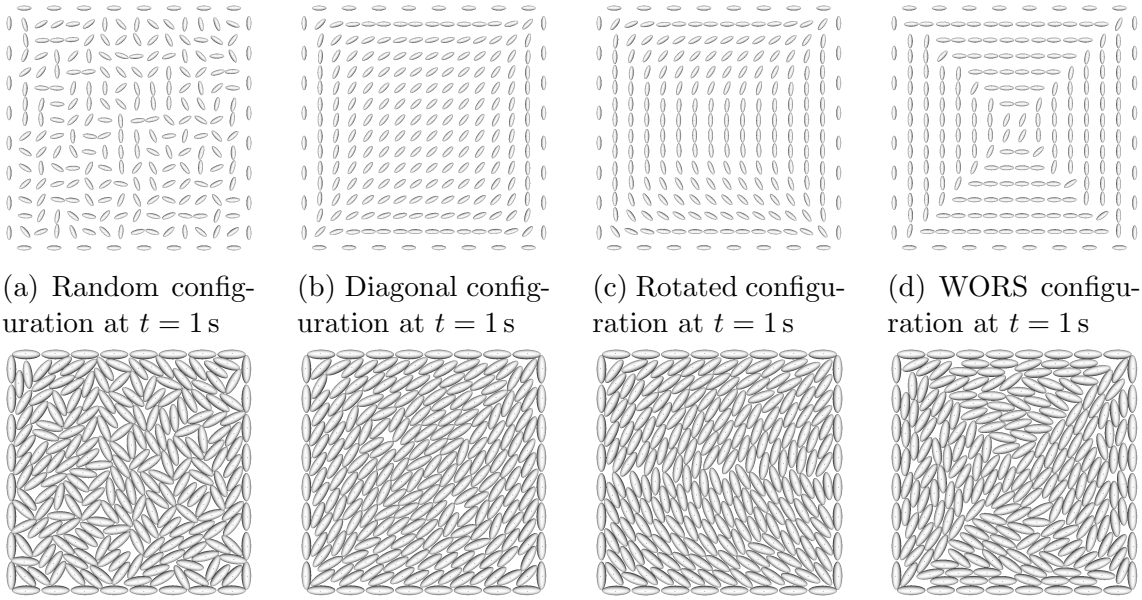
(a) $t = 1\,\mathrm{s}$ (b) $t = 1.5\,\mathrm{s}$

(c) $t = 1.8\,\mathrm{s}$ (d) $t = 2\,\mathrm{s}$

Figure 4.3: *A schematic of the growth of a system of beads into a 'random' configuration. We use* $K = 25\sigma_s$, $\Delta t = 2 \cdot 10^{-3}\,\mathrm{s}$, $t_{grow} = 2\,\mathrm{s}$ *and* $\rho = 0.3136$ *to get the above images, with GB potential parameters* $(\kappa, \kappa', \mu, \nu) = (3, 5, 1, 3)$. *Figure made using* VTK [168].

Euclidean space. The molecule is then given an identical orientation to that point on the grid. We use D1 and R1 for generating diagonal and rotated initial conditions respectively, as D2 and R2–R4 are rotations of those states.

A demonstration of the growth process is given for all four initial configurations by Figure 4.4.



(a) Random configuration at $t = 1\,\mathrm{s}$

(b) Diagonal configuration at $t = 1\,\mathrm{s}$

(c) Rotated configuration at $t = 1\,\mathrm{s}$

(d) WORS configuration at $t = 1\,\mathrm{s}$

(e) Random configuration at $t = 2\,\mathrm{s}$

(f) Diagonal configuration at $t = 2\,\mathrm{s}$

(g) Rotated configuration at $t = 2\,\mathrm{s}$

(h) WORS configuration at $t = 2\,\mathrm{s}$

Figure 4.4: *A demonstration of the four different initial configurations in the 'growing' system at* $t = 1\,\mathrm{s}$ *and* $t = 2\,\mathrm{s}$. *We use* $K = 25\sigma_s$, $\Delta t = 2 \cdot 10^{-3}\,\mathrm{s}$, $t_{grow} = 2\,\mathrm{s}$ *and* $\rho = 0.3136$ *to get the above images, with GB potential parameters* $(\kappa, \kappa', \mu, \nu) = (3, 5, 1, 3)$. *Figure made using* VTK [168].

4.1.7 The Scalar Comparison Parameter

In studying the simulations, both from a random starting configuration and from LdG suggested nematic equilibria, it is desirable to be able to compare the simulations to the LdG states in a quantitative manner. To achieve this, we introduce the scalar comparison parameter E, designed to be similar to the scalar order parameter (1.13), but to give similarity between a simulation and a continuum model rather than similarity to a nematic director.

Suppose we have a molecule n with orientation $\mathbf{u}$ which makes angle θ_n with the x-axis. From this molecule we find the nearest molecule on the reference grid for the nematic equilibria discussed in Section 4.1.5, and suppose this molecule makes an angle θ_{ss} to the x-axis. This gives difference in angle $\theta'_n = \theta_n - \theta_{ss}$. To find the

comparison parameter for a single molecule E_n, we make the calculation

$$E_n = 2\left(\cos^2(\theta'_n) - \frac{1}{2}\right). \tag{4.30}$$

This is a similar calculation to the scalar order parameter for a 3D system (1.13), but it has been adapted to the 2D case such that $E = 0$ represents no similarity between simulation and reference. In order to find the scalar comparison parameter for the entire simulation to a steady state, we take the arithmetic average over all molecules to give

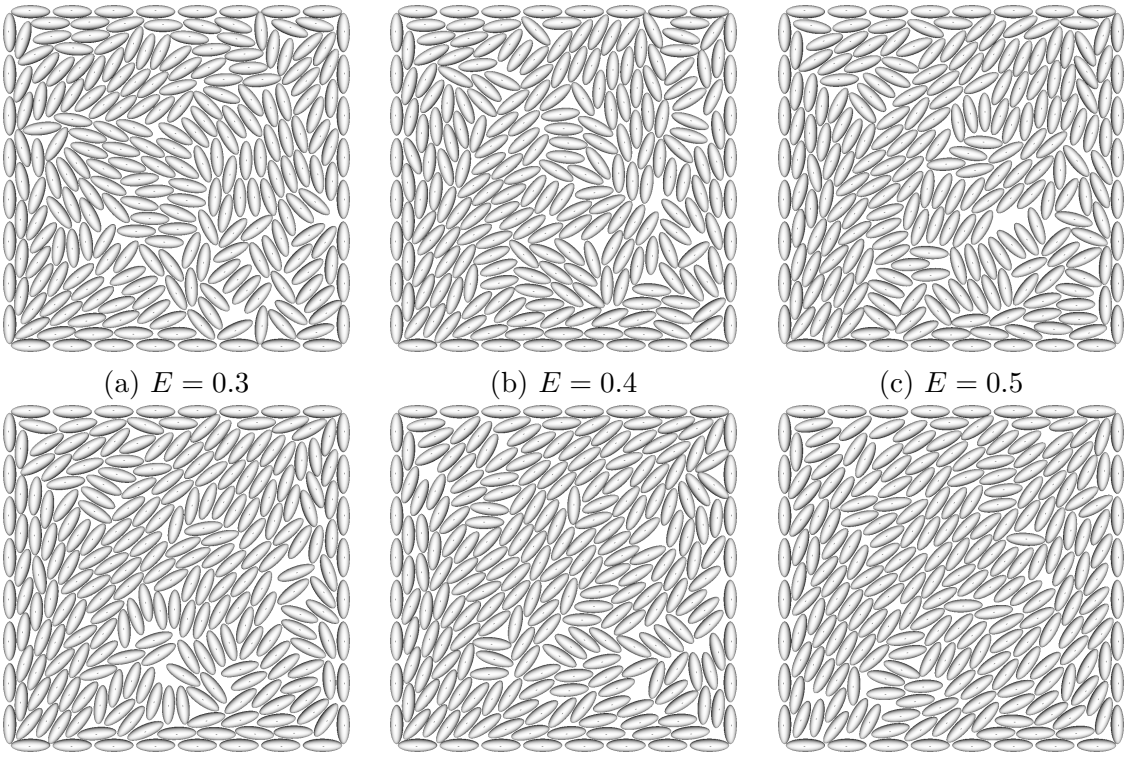
$$E = \langle E_n \rangle = \left\langle 2\left(\cos^2(\theta'_n) - \frac{1}{2}\right)\right\rangle. \tag{4.31}$$

The scalar comparison parameter is designed such that $E = 1$ represents a simulation identical to the continuum model, whilst $E = 0$ represents no similarity, which is the expected value for E when comparing a continuum model to a random configuration. For the diagonal and rotated states, we compare to D1–D2 or R1–R4 respectively and report the largest of the two or four values given to account for the degrees of rotational symmetry. An illustrative example of what different values of E look like during a simulation compared to the diagonal nematic equilibria is given in Figure 4.5.

4.2 Results

We run the simulations to answer two specific questions: whether the LdG suggested nematic equilibria form naturally under random initial starting conditions, as well as whether systems which begin in nematic equilibria remain in those states; in particular whether there is any difference in the behavior for different initial steady states.

The timestep for the system $\Delta t = 2{\cdot}10^{-3}$ s is chosen to be small so that movements over a timestep are mostly small relative to particle size, however due to the nature



(a) $E = 0.3$ (b) $E = 0.4$ (c) $E = 0.5$

(d) $E = 0.6$ (e) $E = 0.7$ (f) $E = 0.8$

Figure 4.5: *A demonstration of different values of the scalar comparison parameter in an illustrative simulation starting in the diagonal configuration for* $\rho = 0.3$*,* $K = 25.561\sigma_s$*,* $\Delta t = 2 \cdot 10^{-3}\,\mathrm{s}$*,* $t_{grow} = 2\,\mathrm{s}$*, with GB potential parameters* $(\kappa, \kappa', \mu, \nu) = (3, 5, 1, 3)$ *and temperature* $k_B T = 0.01\,\mathrm{J}$*. Figure made using* VTK [168].

of the integration scheme and the non-linearity of the GB potential, we reduce the timestep by a factor of 10 if a particle moves more than 0.025 nm, in a manner similar to the integration scheme in [197].

The growth of the system takes time $t_{grow} = 2\,\mathrm{s}$ for all simulations, the GB parameters used are $(\kappa, \kappa', \mu, \nu) = (3, 5, 1, 3)$ and we use viscosity $\eta_s = 1\,\mathrm{mPa{\cdot}s}$ in (4.19).

4.2.1 Random Configurations

In these simulations, we begin in a random configuration and grow the system as described in Section 4.1.6, and then run the for run either 500 s, or until the system is *stable*, whichever happens sooner. A system is judged to be stable if no particle

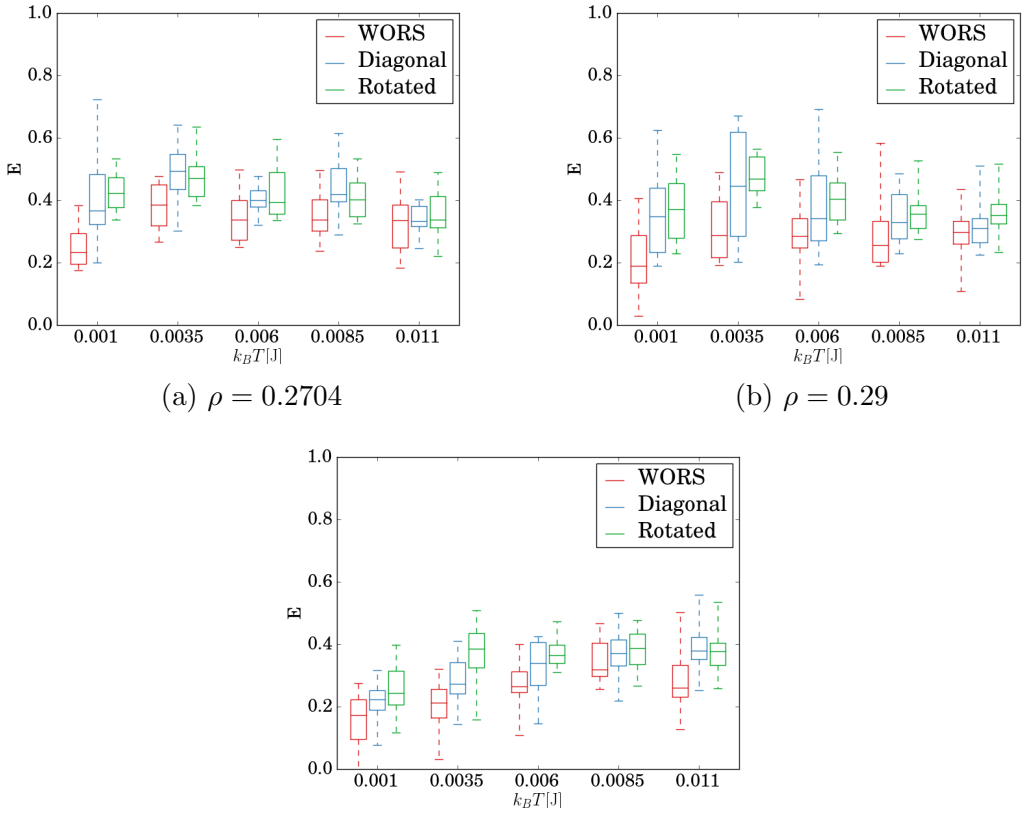
moves a distance greater than $\sigma_s/5$ over a time period of 5 s, a condition which is checked every 0.1s.

This is run for three densities for multiple temperature values k_BT. The first system has density $\rho = 0.2704$ with domain size $K = 25\sigma_s$, which gives a 13×13 initial grid of molecules; the second system has density $\rho = 0.29$ with domain size $K = 26\sigma_s$ to give a 14×14 initial grid of molecules. The third system has density $\rho = 0.31$ with domain size $K = 25\sigma_s$, which results in a 14×14 initial grid of molecules, with 3 molecules removed as described in Section 4.1.6. The three densities are chosen to range from 0.27 which is used in 3D simulations [198], to 0.31 chosen to be denser than the 0.3 used in Robinson et al. [156].

This is simulated at temperatures k_BT ranging from 0.001 J to 0.011 J. The effect of increasing temperature is to increase the size of the Brownian term in simulations which reduces the contribution from GB forces. Below this range of temperatures, the system would equibriate into a state similar to the initial random conditions, so we would not see the LdG equilibria form. Above this range the system would be sufficiently noisy that GB force contributions would be small enough that isotropic states would form away from boundaries.

The results are given in Figure 4.6, from 10 tests at each temperature for each density to find the equilibria. In the $\rho = 0.27$ system all simulations with $k_BT \geq 0.035$ J did not stabilise, 1 settled at $k_BT = 0.0035$ J and all settled at $k_BT = 0.001$J. In the $\rho = 0.29$ system, all simulations with $k_BT \geq 0.06$ J did not settle, 4 settled to stable at 0.0035 J and all settled at $k_BT = 0.001$ J. For $\rho = 0.31$ the system settled to stable for $k_BT \leq 0.0035$ J, 9 systems settled to stable for $k_BT = 0.006$ J and none settled to stable for $k_BT \geq 0.0085$ J. Where the system does not settle to stability, we report on values given at $t = 500$ s, which gives a snapshot of how similar a moving system is to the different LdG suggested equilibria.

In the $\rho = 0.27$ system, we see no WORS solutions forming above a scalar similar-



(a) $\rho = 0.2704$ (b) $\rho = 0.29$

(c) $\rho = 0.31$

Figure 4.6: *Comparison of the formation of LdG nematic equilibria from random initial configuration between different initial densities and values of the temperature* k_BT. *Simulations ran until either* 500 s *had passed or the system became stable, whichever occurs sooner. The results of the tests are given as a box-and-whisker plot to show the full range of similarity parameter values, as well as the median and 25/75% quartile values.*

ity parameter value of $E = 0.5$ at any temperature, with one diagonal state forming with a high similarity score of 0.723205. Out of a total 50 simulations, we see 10 systems with similarity to the diagonal solution above 0.5 and 9 above 0.5 for the rotated state.

For $\rho = 0.29$, there are 5 diagonal systems with similarity score above 0.6, with neither of the other types of equilibria going above this value, but we find 2 systems with similarity above 0.5 for the WORS equilibria, as well as 10 for the diagonal state and 10 for the rotated state.

For $\rho = 0.31$, almost all of the simulations did not see formation of the LdG solutions, with one WORS, one diagonal and two rotated solutions with similarity above 0.5 and none above 0.6.

4.2.2 Systems Which Begin in Nematic Equilibria

In these simulations, we begin the system in one of the the LdG-suggested nematic equilibria, and run the simulation until either the system becomes stable or we lose similarity the initial nematic equilibria. The definition of a stable system is identical to the one given in Section 4.2.1, whilst we say that the initial nematic equilibria is lost when the scalar comparison parameter E falls below some threshold E_T. In these simulations we use the threshold $E_T = 0.5$. Two simulations ran for longer than $t = 500\,\mathrm{s}$ with $E > E_T$, which are included as systems which remained in equilibria.

This system is run with a density of $\rho = 0.3$, which required a box size of $K = 25.561\sigma_s$, chosen to match the density chosen by Robinson et al. [156] for their off-lattice modelling with a 14×14 grid. The temperatures k_BT modelled in a range from $0.0005\,\mathrm{J}$ to $0.004\,\mathrm{J}$, chosen to best illuminate the transition between the nematic equilibria remaining stable and drifting to random noise.

The results are given in Figure 4.7. There are 20 simulations at each temperature for each nematic equilibria. We see that of systems starting in each of the equilibria, the diagonal state is the most robust to higher temperatures, with stable states forming for all temperatures studied. The simulations beginning in the WORS solution were the least robust, where even at the lowest temperatures studied we do not see all simulations settling to a steady state.

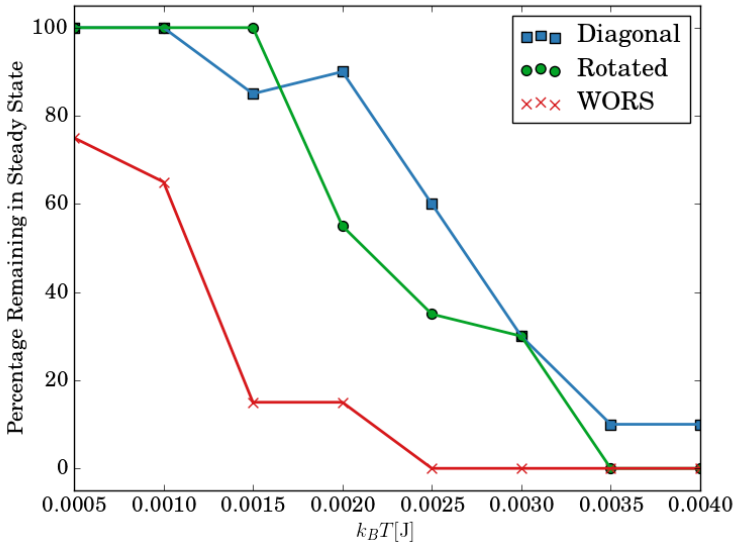


Figure 4.7: *The stability of LdG suggested nematic equilibria for different temperatures k_BT. Simulations were run until either stability or the comparison parameter E falling below* 0.5.

4.3 Discussion

In this chapter, we looked at nematic equilibria in confined systems of NLC molecules using the GB potential. In Sections 4.1.2–4.1.4 we introduce the equations of motion for the system, the numerical scheme and boundary conditions. In Section 4.1.5 we look at the nematic equilibria that we are comparing our simulations to, which are formed from LdG simulations. A novel method to create initial conditions in equilibria and random configurations is laid out in 4.1.6, and a scalar comparison parameter is proposed in 4.1.7. Results for the simulations are given in 4.2.

Starting from a random configuration, we had some success for finding nematic equilibria, with one similarity score above 0.7; however the majority of simulations had similarity score below 0.5, which would be a threshold for weak similarity exhibited. There were also many examples of systems which started with a random initial configuration that ended with similarity to the nematic equilibria with scalar comparison parameter values between 0.5 and 0.7, particularly in systems with lower particle

densities. Further research is needed with a wider parameter serach, particularly on larger domains, to find parameters for which nematic equilibria are consistently found.

In systems where we begin from the LdG nematic equilibria, there was a clear difference in the robustness of the between the diagonal, rotated and WORS solutions. The diagonal solution was the most robust to increasing temperatures compared to both rotated and WORS solutions, similar to the conclusions from the continuum modelling by Luo et al. [110], which suggested that the diagonal solution was more pervasive than the rotated solution. The rotated state was in turn shown to be more robust to higher temperatures than the WORS state, which follows on from the work of Robinson et al. [156] which did not find the WORS solution using discrete off-lattice approaches.

There are a few areas of this work which could be extended upon in future work. The use of the EM integration scheme resulted in prohibitively small timesteps, so that the box size studied was small relative to both previous studies of confined systems and experimental approaches. If a more advanced numerical scheme was applied, for example the use of an implicit method [57, 83], which allowed the use of significantly larger timesteps, then a more comprehensive study of larger boxes and a wider range of parameters could be used to attempt to consistently find the steady states from random initial configuration, as well as to see whether the increased robustness of the diagonal state is seen in other parameter regimes.

To ensure that simulations explore the entire state space of potential configurations, there are also methods which could be used to explore more of the state space, for example the method of continuous tempering [53], where the temperature of the system is dynamically and continuously varied throughout simulations.

This work could also be improved with a more realistic interaction with the boundary, so that instead of modelling the boundary as a line of NLC molecules, we model it as a straight wall and develop an extension to the shape parameter $\sigma(\mathbf{u}_n, \mathbf{u}_m, \hat{\mathbf{r}}_{mn})$

in the GB model for interactions between the particles and the wall. This would remove any minor defects in the wall which may have an influence on the results of simulations, particularly at low domain sizes.

Chapter 5

Conclusion

The main focus of my work has been on the application of BD on systems of particles in the context of polymers and nematic liquid crystals. The work on polymer physics was looking at extending bead-spring models to multiple resolutions, looking at both mathematical analysis applied to these models as well as methods to simulate them. The work on liquid crystals was looking at specific equilibria suggested by continuum modelling arising from applying BD to confined systems.

In Chapter 2, we developed a multi-resolution Rouse model in Algorithm 2.1, which was then applied to a model for the binding of a protein to a DNA filament in Algorithm 2.3. From this model we derived analytic expressions for two macroscopic statistics, the translational diffusion coefficient and the rms end-to-end distance in (2.10) and (2.18) respectively. This allowed us to develop scaling laws (2.20) which could be applied in order to create a family of models which keep these two statistics constant regardless of the resolution scheme chosen. This approach was backed up with numerical simulations compared to a single-scale high resolution model.

In Chapter 3, we looked at developing a multi-resolution generalization to the bead-spring model with HI. We started from a static model (3.1) which was an extension to the GC model with varying statistical segment lengths. This provided the form

for the diffusive displacement equation (3.6) for the polymer coupled with a mobility tensor. In contrast to Chapter 2, the introduction of HI required approximations to be made in order to derive analytic expressions for the translational diffusion coefficient, which was found in the form of a matrix equation (3.16), then in closed form in the long chain limit (3.18). From this we derived scaling laws (3.31) to maintain rms end-to-end distance, translational diffusion coefficient and the strength of HI to give a family of models with the same macro-scale statistics. An extension to the Ermak-McCammon algorithm was developed in Algorithm 3.1 and the simulations were compared against the analytic predictions.

In Chapter 4, a confined system of liquid crystals was studied, in particular looking at nematic equilibria formed from LdG modelling using BD simulations with the GB potential under Dirichlet boundary conditions. A novel method to generate initial conditions for the system was constructed, as well as a scalar comparison parameter in order to quantitatively study the similarity between a BD simulation and the LdG nematic equilibria. We found that there was a difference in behaviour of systems beginning in different LdG equilibria as temperature was varied. The diagonal solution was found to be most robust, with the WORS solution the least robust, which is in agreement with previous research on confined systems [110, 156]. We also looked at the behaviour of systems beginning in random initial conditions, and found systems with moderate levels of similarity to the LdG equilibria would form.

5.1 Further Extensions to my Work

One of the purposes of this work was to introduce the concept of multi-resolution modelling to bead-spring models for polymers. Although the models used were not the most detailed available in the current literature, they were mathematically tractable and so finding analytic expressions for scaling laws became significantly easier. It is

hoped that this approach could be extended to more realistic BD models, in order to increase the number of applications areas in real world problems.

A first step to extending the polymer modelling might be to look at including EV interactions in the modelling like in Chapter 4, for which there is a rich amount of theory which could be expanded upon in the case of polymers [47, 49, 132] in order to provide analytic scaling laws and a simulation scheme in a similar fashion to our above work.

Other steps would involve improving the spring potential used in the model from the Hookean spring to a more realistic potential [54, 84, 159, 167], which might involve a wormlike chain approach [3, 89], as discussed in Section 1.3. Analytic results for macroscopic statistics do exist for the wormlike chain model [64] which would imply that we might be able to find multiscale scaling laws for these models, however in many of the more realistic potentials these do not exist and so a numerical approach would be required.

Another step which could be taken might involve the creation of a hybrid model, whereby multiple models discussed above are combined to get super-detailed modelling in a region of interest coupled with significantly more basic and computationally inexpensive modelling elsewhere. This would involve pairing up numerical scaling laws discussed above, but we would imagine that particular care would need to be taken in the adjacent regions to where the model used changes. An alternative hybrid approach might be to pair a BD model with either coarse-grained or atomistic MD in order to see very large computational savings compared to pure MD. Although work has been done on hybrid particle models in this context [37, 38], pairing a polymer model between the two regions of BD and MD modelling would require further research.

In Chapters 2, 3 and 4 we use variants of the EM algorithm to simulate the systems studied. This was chosen either for simplicity in Chapters 2 and 3 as the main aim

of the simulations was as a demonstration and was chosen in Chapter 4 to follow the methods used by previous authors [119, 197, 198]. For the work on polymers, there have been significant improvements in algorithms which can now run in $\mathcal{O}(N)$ time with only minor approximations [35, 67] compared to the $\mathcal{O}(N^3)$ from the EM algorithm used in Chapter 3. The use of these more recent algorithms combined with the multi-resolution modelling for polymers would allow for even further speed-ups in computational time. With regards to liquid crystal modelling in Chapter 4, as the model does not include HI one could utilise methods from the general stochastic modelling literature [57, 83] rather than the EM algorithm. If more stable numerical approaches were followed, this would allow for larger timesteps used in the model to look at a more extensive range of parameters and in particular larger domain sizes.

There are also improvements in the modelling of NLC molecules in Chapter 4 to look at improving the approach to the Dirichlet boundary conditions, by modelling it as a straight edge rather than with ellipsoidal particles. This could also be coupled with more realistic potentials between particles which have been developed as modifications to the GB potential [138], which could be utilised to more closely match experimental results for liquid crystals.

5.2 How my work relates to the field

The general field of using hybrid modelling for sub-cellular systems is constantly growing, out of the need for accurate modelling on biologically realistic temporal and spatial scales, which current single-scale models often fail to achieve. One of the long-term goals of this area of research should be a full model for a cell on multiple scales, and the work on hybrid modelling will be a crucial part of that. With further developments, this would enable us to model, for example, the behaviour of a cell in the presence of a drug, where the elements of the cell which are transporting and

interacting with the drug are modelled in ultra-fine detail while the rest of the cell is measured in a coarse-grained fashion in order to meet the requirements of accuracy and computational efficiency. The field is very far away from being able to model this, but recent developments are bringing us closer to a place where such modelling might be possible.

To fit into this view of where we are heading, I see my model as sitting towards the less-detailed but more computationally efficient end of the spectrum of hybrid models applied to biopolymers. In particular the multi-resolution Rouse model allows us to model large quantities of polymer on multiple scales without requiring complex calculations. It was demonstrated in Section 2.3 that this multi-resolution model can be used to study biological interactions with external molecules while maintaining consistency of behaviour across scales. If the extensions discussed in Section 5.1 are explored for the multi-resolution bead-spring model then similar simulations of interactions with external particles should be possible, enabling this modelling to operate on additional scales.

It should be worth noting that at more microscopic scales there have been encouraging successes at multiscale modelling bought on by Dissipative Particle Dynamics (DPD) [58, 69, 105], which considers the interaction of soft spheres, as well as from Lattice Boltzmann methods [22], which models a fluid as particles rather than complex grids as is common in Navier-Stokes solutions to satisfy kinetic equations. By modelling the solvent in this way, both methods can utilise significant improvements in computational speed for molecular simulations, enabling a wider scope to be considered for both temporal and spatial dimensions. These approaches are being used widely in both polymer modelling as well as more general dynamic problems [23, 85, 134].

There have also been other key areas of development in the application of hybrid models between stochastic and atomistic scales, for example Erban has looked at the

Model	Scale	Brief Description
Multi-resolution bead-spring models discussed in Chapters 2 and 3	Mesoscale	Extends bead-spring models with and without HI to multiple resolutions
Dissipative Particle Dynamics (DPD) [58, 69]	Molecular	Models the solvent as interactions between soft spheres
Lattice Boltzmann [22]	Molecular	Models the fluid as particles
Models bridging from BD to MD [37, 38]	BD/MD	Particle models bridging the gap between stochastic and molecular modelling
Adaptive-resolution modelling [55, 96]	CG/MD	Models water adaptively with either MD or CG depending on proximity to a polymer

Table 5.1: *A brief summary of the different models in the field of hybrid modelling of polymers.*

potential for creating hybrid models at the particle level between BD and MD [37,38]. This could be extended in future to specifically study polymers between these scales.

At the molecular level, there are also exciting directions for hybrid modelling between CG and full-atomistic MD models, for example by taking an adaptive-resolution approach [55, 200]. Adaptive-resolution modelling models water molecules near the polymer atomistically and considers far away water molecules as collective units, with a dynamic procedure to assign water molecules to be modelled at either CG or atomistic scales depending on distance from the area of interest.

By bringing all of these DNA polymer models together, the field could then implement a model the entire life-cycle for a protein binding to DNA. It could start at a macroscopic scale, with very low-detailed models at the level of the full chromosome. As this protein comes sufficiently close to the chromosome we would then adaptively increase the resolution of the model for a polymer to ensure that we are sufficiently accurate. This could start with my models from Chapters 2 and 3, before zooming in to models which operate at the level of CG or MD, as discussed above. This would

create a cascade of models, each appropriate for the level of detail required at each lengthscale, without expending unnecessary amounts of computational energy on each problem. A summary of existing models which have seen successes at bridging scales in polymer modelling are given in Table 5.1.

Following on from my work on NLCs, it is hoped that some of the novel techniques which I have used to study this particular system of confined NLCs could be extended to a wider class of problems involving liquid crystals. Firstly, the approach to forming initial conditions by 'growing' the particles could be applied to dynamic systems which exhibit significant crowding effects such that creating initial conditions without overlaps is a problem. As well as this, the introduction of a metric to look at similarity between two systems of NLCs could be applied to theoretical or simulation results for other problems in which particle orientation is the key indicator of system behaviour.

Bibliography

[1] B. J. Alder and T. E. Wainwright. Studies in molecular dynamics. I. General method. *J. Chem. Phys.*, 31(2):459–466, 1959.

[2] M. P. Allen and M. R. Wilson. Computer simulation of liquid crystals. *J. Comput. Aided Mol. Des.*, 3(4):335–353, 1989.

[3] S. A. Allison. Brownian dynamics simulation of wormlike chains. Fluorescence depolarization and depolarized light scattering. *Macromolecules*, 19(1):118–124, 1986.

[4] M. S. Alnæs, J. Blechta, J. Hake, A. Johansson, B. Kehlet, A. Logg, C. Richardson, J. Ring, M. Rognes, and G. Wells. The FEniCS project version 1.5. *Archive of Numerical Software*, 3(100):9–23, 2015.

[5] S. Amelar, C. E. Eastman, R. L. Morris, M. A. Smeltzly, T. P. Lodge, and E. D. Von Meerwall. Dynamic properties of low-and moderate-molecular-weight polystyrenes at infinite dilution. *Macromolecules*, 24(12):3505–3516, 1991.

[6] T. Ando, E. Chow, Y. Saad, and J. Skolnick. Krylov subspace methods for computing hydrodynamic interactions in Brownian dynamics simulations. *J. Chem. Phys.*, 137(6):064106, 2012.

[7] S. S. Andrews. Methods for modeling cytoskeletal and DNA filaments. *Phys. Biol.*, 11(1):011001, 2014.

[8] A. Annunziato. DNA packaging: Nucleosomes and chromatin. *Nature Ed.*, 1(1):26, 2008.

[9] P. L. Auer and C. S. Gardner. Note on singular integral equations of the Kirkwood-Riseman type. *J. Chem. Phys.*, 23(8):1545–1546, 1955.

[10] M. Barbieri, M. Chotalia, J. Fraser, L. Lavitas, J. Dostie, A. Pombo, and M. Nicodemi. Complexity of chromatin folding is captured by the strings and binders switch model. *P. Natl. Acad. Sci.*, 109(40):16173–16178, 2012.

[11] M. A. Bates and G. R. Luckhurst. Computer simulation studies of anisotropic systems. XXX. The phase behavior and structure of a Gay–Berne mesogen. *J. Chem. Phys.*, 110(14):7087–7108, 1999.

[12] R. Berardi, Andrew P. J. Emerson, and C. Zannoni. Monte Carlo investigations of a Gay-Berne liquid crystal. *J. Chem. Soc., Faraday Trans.*, 89:4069–4078, 1993.

[13] H. J. C. Berendsen, D. van der Spoel, and R. van Drunen. GROMACS: A message-passing parallel molecular dynamics implementation. *Comput. Phys. Commun.*, 91(1-3):43–56, 1995.

[14] B. J. Berne and P. Pechukas. Gaussian model potentials for molecular interactions. *J. Chem. Phys.*, 56(8):4213–4216, 1972.

[15] R. B. Bird, R. C. Armstrong, O. Hassager, and C. F. Curtiss. *Dynamics of Polymeric Liquids-Volume 2: Kinetic Theory, 2nd edition.* Wiley, 1987.

[16] R. B. Bird, P. J. Dotson, and N. L. Johnson. Polymer solution rheology based on a finitely extensible bead-spring chain model. *J. Non-Newtonian Fluid Mech.*, 7(2):213–235, 1980.

[17] C. A. Brackley, M. E. Cates, and D. Marenduzzo. Intracellular facilitated diffusion: searchers, crowders, and blockers. *Phys. Rev. Lett.*, 111(10):108101, 2013.

[18] C. A. Brackley, J. Johnson, S. Kelly, P. R. Cook, and D. Marenduzzo. Simulated binding of transcription factors to active and inactive regions folds human chromosomes into loops, rosettes and topological domains. *Nucleic Acids Res.*, 44(8):3503–3512, 2016.

[19] R. Brown. XXVII. A brief account of microscopical observations made in the months of June, July and August 1827, on the particles contained in the pollen of plants; and on the general existence of active molecules in organic and inorganic bodies. *Philos. Mag.*, 4(21):161–173, 1828.

[20] K. Bystricky, P. Heun, J. Gehlen, L. R.and Langowski, and S. M. Gasser. Long-range compaction and flexibility of interphase chromatin in budding yeast analyzed by high-resolution imaging techniques. *Proc. Natl. Acad. Sci. U. S. A.*, 101(47):16495–16500, 2004.

[21] J. A. Castellano. *Liquid gold: the story of liquid crystal displays and the creation of an industry.* World Scientific, 2005.

[22] S. Chen and G. D. Doolen. Lattice Boltzmann method for fluid flows. *Annu. Rev. Fluid Mech.*, 30(1):329–364, 1998.

[23] Y. L. Chen, H. Ma, M. D. Graham, and J. J. de Pablo. Modeling DNA in confinement: A comparison between the Brownian Dynamics and Lattice Boltzmann method. *Macromolecules*, 40(16):5978–5984, 2007.

[24] S. Chib and E. Greenberg. Understanding the Metropolis-Hastings algorithm. *Amer. Statist.*, 49(4):327–335, 1995.

[25] C. Chiccoli, P. Pasini, and C. Zannoni. A Monte Carlo simulation of the inhomogeneous Lebwohl-Lasher lattice model. *Liq. Cryst.*, 2(1):39–54, 1987.

[26] R. Collepardo-Guevara and T. Schlick. Chromatin fiber polymorphism triggered by variations of DNA linker lengths. *PNAS*, 111(22):8061–8066, 2014.

[27] T. Cremer, M. Cremer, B. Hübner, H. Strickfaden, D. Smeets, J. Popken, M. Sterr, Y Markaki, K. Rippe, and C. Cremer. The 4D nucleome: Evidence for a dynamic nuclear landscape based on co-aligned active and inactive nuclear compartments. *FEBS letters*, 589(20PartA):2931–2943, 2015.

[28] P. D. Dans, J. Walther, Gómez H., and M. Orozco. Multiscale simulation of DNA. *Curr. Opin. Struct. Biol.*, 37:29 – 45, 2016.

[29] P. G. de Gennes and J. Prost. *The Physics of Liquid Crystals, 2nd edition*, volume 83. Oxford University Press, 1995.

[30] J. Dekker, M. A. Marti-Renom, and L. A. Mirny. Exploring the three-dimensional organization of genomes: interpreting chromatin interaction data. *Nat. Rev. Genet.*, 14:390–403, 2013.

[31] J. Dekker, K. Rippe, M. Dekker, and N. Kleckner. Capturing chromosome conformation. *Science*, 295(5558):1306–1311, 2002.

[32] N. Di Pasquale and P. Carbone. Local and global dynamics of multi-resolved polymer chains: Effects of the interactions atoms-beads on the dynamic of the chains. *J. Chem. Phys.*, 146(8):084905, 2017.

[33] M. Doi and S. F. Edwards. *The Theory of Polymer Dynamics*. Oxford University Press, 1988.

[34] Z. Duan, M. Andronescu, K. Schutz, S. McIlwain, Y. J.J Kim, C. Lee, J. Shendure, S. Fields, C. . Blau, and W. S. Noble. A three-dimensional model of the yeast genome. *Nature*, 465:363–367, 2010.

[35] B. Dünweg and A. J. C. Ladd. *Advanced Computer Simulation Approaches for Soft Matter Sciences III*, chapter Lattice Boltzmann Simulations of Soft Matter Systems, pages 89–166. Springer Berlin Heidelberg, Berlin, Heidelberg, 2009.

[36] D. Dürr, S. Goldstein, and J. L. Lebowitz. A mechanical model of Brownian motion. *Commun. Math. Phys.*, 78(4):507–530, 1981.

[37] R. Erban. From molecular dynamics to Brownian dynamics. *Proc. R. Soc. A*, 470(2167):20140036, 2014.

[38] R. Erban. Coupling all-atom molecular dynamics simulations of ions in water with Brownian dynamics. *Proc. R. Soc. A*, 472(2186):20150556, 2016.

[39] R. Erban and S. J. Chapman. Stochastic modelling of reaction–diffusion processes: algorithms for bimolecular reactions. *Phys. Biol.*, 6:046001, 2009.

[40] J. L. Ericksen. Liquid crystals with variable degree of orientation. *Arch. Ration. Mech. An.*, 113:97–120, 1991.

[41] D. L. Ermak and J. A. McCammon. Brownian dynamics with hydrodynamic interactions. *J. Chem. Phys.*, 69(4):1352–1360, 1978.

[42] W. Feller. *An introduction to probability theory and its applications*. John Wiley & Sons, 1968.

[43] G. Felsenfeld and M. Groudine. Controlling the double helix. *Nature*, 421:448–453, 2003.

[44] M. Fixman. Inclusion of hydrodynamic interaction in polymer dynamical simulations. *Macromolecules*, 14(6):1710–1717, 1981.

[45] M. Fixman. Construction of Langevin forces in the simulation of hydrodynamic interaction. *Macromolecules*, 19(4):1204–1207, 1986.

[46] M. B. Flegg, S. J. Chapman, and R. Erban. The two-regime method for optimizing stochastic reaction-diffusion simulations. *J. R. Soc. Interface*, 9:859–868, 2012.

[47] P. J. Flory. The configuration of real polymer chains. *J. Chem. Phys.*, 17(3):303–310, 1949.

[48] F. C. Frank. I. Liquid crystals. On the theory of liquid crystals. *Discuss. Faraday Soc.*, 25:19–28, 1958.

[49] K. F. Freed. *Renormalization Group Theory of Macromolecules*. John Wiley & Sons, 1987.

[50] J. G. Gay and B. J. Berne. Modification of the overlap potential to mimic a linear site–site potential. *J. Chem. Phys.*, 74(6):3316–3319, 1981.

[51] L. R. Gehlen, G. Gruenert, M. B. Jones, C. D. Rodley, J. Langowski, and J. M. O'Sullivan. Chromosome positioning and the clustering of functionally related loci in yeast is driven by chromosomal interactions. *Nucleus*, 3(4):370–383, 2012.

[52] T. Geyer and U. Winter. An $\mathcal{O}(N^2)$ approximation for hydrodynamic interactions in Brownian dynamics simulations. *J. Chem. Phys.*, 130(11):114905, 2009.

[53] G. Gobbo and B. J. Leimkuhler. Extended hamiltonian approach to continuous tempering. *Phys. Rev. E*, 91:061301, Jun 2015.

[54] Y. Goldtzvik, Z. Zhang, and D. Thirumalai. Importance of hydrodynamic interactions in the stepping kinetics of kinesin. *J. Phys. Chem. B*, 120(8):2071–2075, 2016.

[55] H. C. Gonzalez, L. Darré, and S. Pantano. Transferable mixing of atomistic and coarse-grained water models. *J. Phys. Chem. B*, 117(46):14438–14448, 2013.

[56] J. W. Goodby, P. J. Collings, T. Kato, C. Tschierske, H. F. Gleeson, and P. Raynes. *Handbook of Liquid Crystals*. Wiley-VCH, 2014.

[57] A. Greiner, W. Strittmatter, and J. Honerkamp. Numerical integration of stochastic differential equations. *J. Stat. Phys.*, 51(1):95–108, 1988.

[58] R. D. Groot and P. B. Warren. Dissipative particle dynamics: Bridging the gap between atomistic and mesoscopic simulation. *J. Chem. Phys.*, 107(11):4423–4435, 1997.

[59] A. Grosberg, Y. Rabin, S. Havlin, and A. Neer. Crumpled globule model of the three-dimensional structure of DNA. *EPL (Europhysics Letters)*, 23(5):373, 1993.

[60] A. Y. Grosberg. How two meters of DNA fit into a cell nucleus: Polymer models with topological constraints and experimental data. *Polym. Sci. Ser C+*, 54(1):1–10, 2012.

[61] M. G. Guenza. Theoretical models for bridging timescales in polymer dynamics. *J. Phys.: Condens. Matter*, 20(3):033101, 2007.

[62] E. Guth and H. Mark. Zur innermolekularen, Statistik, insbesondere bei Kettenmolekiilen I. *Monatsh. Chem.*, 65(1):93–121, 1934.

[63] P. J. Hagerman. Flexibility of DNA. *Annu. Rev. Biophys. Biophys. Chem.*, 17(1):265–286, 1988.

[64] P. J. Hagerman and B. H. Zimm. Monte Carlo approach to the analysis of the rotational diffusion of wormlike chains. *Biopolymers*, 20:1481–1502, 1981.

[65] D. W. Hair and E. J. Amis. Intrinsic dynamic viscoelasticity of polystyrene in Θ and good solvents. *Macromolecules*, 22(12):4528–4536, 1989.

[66] S. E. Halford and J. F. Marko. How do site-specific DNA-binding proteins find their targets? *Nucleic Acids Res.*, 32(10):3040–3052, 2004.

[67] J. P. Hernández-Ortiz, J. J. de Pablo, and M. D. Graham. Fast computation of many-particle hydrodynamic and electrostatic interactions in a confined geometry. *Phys. Rev. Lett.*, 98(14):140602, 2007.

[68] D. M. Hinckley, G. S. Freeman, J. K. Whitmer, and J. J. De Pablo. An experimentally-informed coarse-grained 3-site-per-nucleotide model of DNA: Structure, thermodynamics, and dynamics of hybridization. *J. Chem. Phys.*, 139(14):144903, 2013.

[69] P. J. Hoogerbrugge and J. M. V. A. Koelman. Simulating microscopic hydrodynamic phenomena with dissipative particle dynamics. *Europhys. Lett.*, 19(3):155, 1992.

[70] I. Hörger, E. Velasco, J. Mingorance, G. Rivas, P. Tarazona, and M. Vélez. Langevin computer simulations of bacterial protein filaments and the force-generating mechanism during cell division. *Phys. Rev. E*, 77(1):011902, 2008.

[71] A. Hotz and R. E. Skelton. Covariance control theory. *Int. J. Control*, 46(1):13–32, 1987.

[72] G. A. Huber and S. Kim. Weighted-ensemble Brownian dynamics simulations for protein association reactions. *Biophys. J.*, 70(1):97–110, 1996.

[73] J. S. Hur, E. S. G. Shaqfeh, H. P. Babcock, D. E. Smith, and S. Chu. Dynamics of dilute and semidilute DNA solutions in the start-up of shear flow. *J. Rheol*, 45(2):421–450, 2001.

[74] Joe S Hur, Eric SG Shaqfeh, and Ronald G Larson. Brownian dynamics simulations of single dna molecules in shear flow. *Journal of Rheology (1978-present)*, 44(4):713–742, 2000.

[75] I. Ivani, P. D. Dans, A. Noy, A. Pérez, I. Faustino, A. Hospital, J. Walther, P. Andrio, R. Goñi, A. Balaceanu, G. Portella, F. Battistini, J. L. Gelpí, C. González, M. Vendruscolo, C. A. Laughton, S. A. Harris, D. A. Case, and M. Orozco. Parmbsc1: a refined force field for DNA simulations. *Nat. Methods*, 13:55–58, 2016.

[76] D. J. Jeffrey and Y. Onishi. Calculation of the resistance and mobility functions for two unequal rigid spheres in low-Reynolds-number flow. *J. Fluid Mech.*, 139:261—290, 1984.

[77] R. M. Jendrejack, J. J. de Pablo, and M. D. Graham. Stochastic simulations of DNA in flow: Dynamics and the effects of hydrodynamic interactions. *J. Chem. Phys.*, 116(17):7752–7759, 2002.

[78] J. C. Jones. The Zenithal Bistable Display: From concept to consumer. *J. Soc. Inf. Display*, 16(1):143–154, 2008.

[79] J. E. Jones. On the determination of molecular fields. II. from the equation of state of a gas. *Proc. R. Soc. A*, 106(738):463–477, 1924.

[80] S. Jun and B. Mulder. Entropy-driven spatial organization of highly confined polymers: lessons for the bacterial chromosome. *P. Natl. Acad. Sci. USA*, 103(33):12388–12393, 2006.

[81] I. C. Khoo, D. H. Werner, X. Liang, A. Diaz, and B. Weiner. Nanosphere dispersed liquid crystals for tunable negative-zero-positive index of refraction in the optical and terahertz regimes. *Opt. Lett.*, 31(17):2592–2594, 2006.

[82] J. G. Kirkwood and J. Riseman. The intrinsic viscosities and diffusion constants of flexible macromolecules in solution. *J. Chem. Phys.*, 16(6):565–573, 1948.

[83] P. Kloeden and E. Platen. *Numerical Solution of Stochastic Differential Equations*. Springer, 1992.

[84] T. A. Knotts, N. Rathore, D. C. Schwartz, and J. J. de Pablo. A coarse grain model for DNA. *J. Chem. Phys.*, 126(8):084901, 2007.

[85] Y. Kong, C. W. Manke, W. G. Madden, and A. G. Schlijper. Simulation of a confined polymer in solution using the dissipative particle dynamics method. *Int. J Thermophys.*, 15(6):1093–1101, Nov 1994.

[86] R. D. Kornberg. Chromatin structure: a repeating unit of histones and DNA. *Science*, 184(4139):868–871, 1974.

[87] N. Korolev, L. Nordenskiöld, and A. P. Lyubartsev. Multiscale coarse-grained modelling of chromatin components: DNA and the nucleosome. *Adv. Colloid Interface Sci.*, 232:36–48, 2016.

[88] S. Kralj and A. Majumdar. Order reconstruction patterns in nematic liquid crystal wells. *Proc. R. Soc. A*, 470:20140276, 2014.

[89] O. Kratky and G. Porod. Röntgenuntersuchung gelöster Fadenmoleküle. *Recl. Trav. Chim. Pay. B.*, 68(12):1106–1122, 1949.

[90] K. Kremer and G. S. Grest. Dynamics of entangled linear polymer melts: A molecular-dynamics simulation. *J. Chem. Phys.*, 92(8):5057–5086, 1990.

[91] W. Kuhn. Über die Gestalt fadenförmiger Moleküle in lösungen. *Kolloid Z.*, 68(1):2–15, 1934.

[92] K. S. Kumar and J. R. Prakash. Equilibrium swelling and universal ratios in dilute polymer solutions: *Exact* Brownian dynamics simulations for a delta function excluded volume potential. *Macromolecules*, 36(20):7842–7856, 2003.

[93] J Langowski. Polymer chain models of DNA and chromatin. *Eur. Phys. J. E*, 19(3):241–249, 2006.

[94] R. G. Larson, H. Hu, D. E. Smith, and S. Chu. Brownian dynamics simulations of a DNA molecule in an extensional flow field. *J. Rheol*, 43(2):267–304, 1999.

[95] Ronald G Larson. The rheology of dilute solutions of flexible polymers: Progress and problems. *Journal of Rheology*, 49(1):1–70, 2005.

[96] P. A. Lebwohl and G. Lasher. Nematic-liquid-crystal order—a Monte Carlo calculation. *Phys. Rev. A*, 6(1):426–429, 1972.

[97] S. Lee, M. Karplus, D. Bashford, and D. Weaver. Brownian dynamics simulation of protein folding: A study of the diffusion-collision model. *Biopolymers*, 26(4):481–506, 1987.

[98] B. Leimkuhler and C. Matthews. Rational construction of stochastic numerical methods for molecular sampling. *Applied Mathematics Research eXpress*, 2013(1):34–56, 2013.

[99] B. Leimkuhler and C. Matthews. *Molecular Dynamics: With Deterministic and Stochastic Numerical Methods*. Springer, 2015.

[100] A. H. Lewis, I. Garlea, J. Alvarado, O. J. Dammone, P. D. Howell, A. Majumdar, B. M. Mulder, M. P. Lettinga, G. H. Koenderink, and D. G. A. L. Aarts. Colloidal liquid crystals in rectangular confinement: theory and experiment. *Soft Matter*, 10(39):7865–7873, 2014.

[101] E. Lieberman-Aiden, N. L. Van Berkum, L. Williams, M. Imakaev, T. Ragoczy, A. Telling, I. Amit, B. R. Lajoie, P. J. Sabo, M. O. Dorschner, et al. Comprehensive mapping of long-range interactions reveals folding principles of the human genome. *Science*, 326(5950):289–293, 2009.

[102] F. H. Lin and C. Liu. Static and dynamic theories of liquid crystals. *J. Partial Differential Equations*, 14(4):289–330, 2001.

[103] B. Liu and B. Dünweg. Translational diffusion of polymer chains with excluded volume and hydrodynamic interactions by Brownian dynamics simulation. *J. Chem. Phys.*, 118(17):8061–8072, 2003.

[104] C. Liu and M. Muthukumar. Langevin dynamics simulations of early-stage polymer nucleation and crystallization. *J. Chem. Phys.*, 109(6):2536–2542, 1998.

[105] M. B. Liu, G. R. Liu, L. W. Zhou, and J. Z. Chang. Dissipative particle dynamics (DPD): An overview and recent developments. *Arch. Comput. Methods Eng.*, 22(4):529–556, Nov 2015.

[106] T. W. Liu. Flexible polymer chain dynamics and rheological properties in steady flows. *J. Chem. Phys.*, 90(10):5826–5842, 1989.

[107] A. S. Lodge and Y. Wu. Constitutive equations for polymer solutions derived from the bead/spring model of Rouse and Zimm. *Rheologica Acta*, 10(4):539–553, December 1971.

[108] A. Logg, G. N. Wells, and J. Hake. *Automated Solution of Differential Equations by the Finite Element Method. Lecture Notes in Computational Science and Engineering, vol 84.*, chapter DOLFIN: a C++/Python finite element library, pages 173–225. Springer, Berlin, Heidelberg, 2012.

[109] G. R. Luckhurst, R. A. Stephens, and R. W. Phippen. Computer simulation studies of anisotropic systems. XIX. mesophases formed by the Gay-Berne model mesogen. *Liq. Cryst.*, 8(4):451–464, 1990.

[110] C. Luo, A. Majumdar, and R. Erban. Multistability in planar liquid crystal wells. *Phys. Rev. E*, 85(6):061702, 2012.

[111] M. R. Machado, P. D. Dans, and S. Pantano. A hybrid all-atom/coarse grain model for multiscale simulations of DNA. *Phys. Chem. Chem. Phys.*, 13:18134–18144, 2011.

[112] M. R. Machado and S. Pantano. Exploring LacI–DNA dynamics by multiscale simulations using the SIRAH force field. *J. Chem. Theory Comput.*, 11(10):5012–5023, 2015. PMID: 26574286.

[113] K. Maeshima, K. Kaizu, S. Tamura, T. Nozaki, T. Kokubo, and K. Takahashi. The physical size of transcription factors is key to transcriptional regulation in chromatin domains. *J. Phys-Condens. Mat.*, 27(6):064116, 2015.

[114] K. Maeshima, R. Rogge, S. Tamura, Y. Joti, T.i Hikima, H. Szerlong, C. Krause, J. Herman, E. Seidel, J. DeLuca, et al. Nucleosomal arrays self-assemble into supramolecular globular structures lacking 30-nm fibers. *EMBO J.*, 35(10):1115–1132, 2016.

[115] A. Majumdar. Equilibrium order parameters of nematic liquid crystals in the Landau-de Gennes theory. *Eur. J. Appl. Math.*, 21(2):181–203, 2010.

[116] A. Majumdar and A. Zarnescu. Landau-de Gennes theory of nematic liquid crystals: the 0seen-Frank limit and beyond. *Arch. Ration. Mech. An.*, 196(1):227–280, 2010.

[117] L. Miao, C. D. Young, and C. E. Sing. An iterative method for hydrodynamic interactions in Brownian dynamics simulations of polymer dynamics. *J. Chem. Phys.*, 147(2):024904, 2017.

[118] L. A. Mirny. The fractal globule as a model of chromatin architecture in the cell. *Chromosome Res.*, 19(1):37–51, 2011.

[119] N. Mori, R. Semura, and K. Nakamura. Simple shear flows of suspensions of Brownian ellipsoids interacting via the Gay-Berne potential. *Mol. Cryst. Liq. Cryst. A*, 367(1):445–453, 2001.

[120] N. Mottram and C. J. P. Newton. Introduction to Q-tensor theory. Working paper, University of Strathclyde, September 2014.

[121] O. Müller, N. Kepper, R. Schöpflin, R. Ettig, K. Rippe, and G. Wedemann. Changing chromatin fiber conformation by nucleosome repositioning. *Biophys. J.*, 107(9):2141–2150, 2014.

[122] S. Nawaz, M. Redhead, G. Mantovani, C. Alexander, C. Bosquillon, and P. Carbone. Interactions of PEO–PPO–PEO block copolymers with lipid membranes: a computational and experimental study linking membrane lysis with polymer structure. *Soft Matter*, 8:6744–6754, 2012.

[123] R. M. Neal. Slice sampling. *Ann. Statist.*, 31(3):705–767, 2003.

[124] E. Nelson. *Dynamical Theories of Brownian Motion*, volume 3. Princeton University Press, 1967.

[125] H. Ochiai, T. Sugawara, and T. Yamamoto. Simultaneous live imaging of the transcription and nuclear position of specific genes. *Nucleic Acids Res.*, 43(19):e127, 2015.

[126] L. Onsager. The effects of shape on the interaction of colloidal particles. *Ann. N. Y. Acad. Sci.*, 51(4):627–659, 1949.

[127] T. Oppelstrup, V. V. Bulatov, A. Donev, M. H. Kalos, G. H. Gilmer, and B. Sadigh. First-passage kinetic Monte Carlo method. *Phys. Rev. E*, 80(6):066701, 2009.

[128] S. Orlandi, E. Benini, I. Miglioli, D. R. Evans, V. Reshetnyak, and C. Zannoni. Doping liquid crystals with nanoparticles. a computer simulation of the effects of nanoparticle shape. *Phys. Chem. Chem. Phys.*, 18(4):2428–2441, 2016.

[129] H. C. Öttinger. Generalized Zimm model for dilute polymer solutions under theta conditions. *J. Chem. Phys.*, 86(6):3731–3749, 1987.

[130] H. C. Öttinger. Translational diffusivity from the Zimm model. *J. Chem. Phys.*, 87(5):3156–3165, 1987.

[131] H. C. Öttinger. *Stochastic processes in polymeric fluids: tools and examples for developing simulation algorithms.* Springer-Verlag Berlin Heidelberg, 1996.

[132] H. C. Öttinger and Y. Rabin. Renormalization-group calculation of viscometric functions based on conventional polymer kinetic theory. *J. Non-Newtonian Fluid Mech.*, 33(1):53–93, 1989.

[133] P. Palffy-Muhoray. The diverse world of liquid crystals. *Phys. Today*, 60(9):54–60, 2007.

[134] H. Pan, T. Y. Ng, H. Li, and E. Moeendarbary. Dissipative particle dynamics simulation of entropic trapping for DNA separation. *Sens. Actuat. A Phys.*, 157(2):328 – 335, 2010.

[135] S. Pan, D Ahirwal, D. A. Nguyen, T. Sridhar, P. Sunthar, and J. R. Prakash. Viscosity radius of polymers in dilute solutions: Universal behavior from DNA

rheology and Brownian dynamics simulations. *Macromolecules*, 47(21):7548–7560, 2014.

[136] Alberto Pérez, F. J. Luque, and M. Orozco. Frontiers in molecular dynamics simulations of DNA. *Acc. Chem. Res.*, 45(2):196–205, 2012.

[137] T. T. Perkins, Quake, D. E. Smith, and S. Chu. Relaxation of a single DNA molecule observed by optical microscopy. *Science*, 264(5160):822–826, 1994.

[138] R. A. X. Persson. Note: Modification of the gay-berne potential for improved accuracy and speed. *J. Chem. Phys.*, 136(22):226101, 2012.

[139] J. C. Phillips, R. Braun, W. Wang, J. Gumbart, E. Tajkhorshid, E. Villa, C. Chipot, R. D. Skeel, L. Kale, and K. Schulten. Scalable molecular dynamics with NAMD. *J. Comput. Chem.*, 26(16):1781–1802, 2005.

[140] B. Pierce. *Genetics: A Conceptual Approach, 6th edition*. WH Freeman, 2016.

[141] T. D. Pollard and G. G. Borisy. Cellular motility driven by assembly and disassembly of actin filaments. *Cell*, 112(4):453–465, 2003.

[142] S. A. Ponomarenko, N. I. Boiko, V. P. Shibaev, R. M. Richardson, I. J. Whitehouse, E. A. Rebrov, and A. M. Muzafarov. Carbosilane liquid crystalline dendrimers: from molecular architecture to supramolecular nanostructures. *Macromolecules*, 33(15):5549–5558, 2000.

[143] R. Potestio, C. Peter, and K. Kremer. Computer simulations of soft matter: Linking the scales. *Entropy*, 16(8):4199–4245, 2014.

[144] D. A. Potoyan, A. Savelyev, and G. A. Papoian. Recent successes in coarse-grained modeling of DNA. *WIREs. Comput. Mol. Sci.*, 3(1):69–83, 2013.

[145] J. R. Prakash and H. C. Öttinger. Universal viscometric functions for dilute polymer solutions. *J. Non-Newtonian Fluid Mech.*, 71(3):245–272, 1997.

[146] S. R. Quake, H. Babcock, and S. Chu. The dynamics of partially extended single molecules of DNA. *Nature*, 388:151–154, 1997.

[147] J. O. Rädler, I Koltover, T. Salditt, and C. R. Safinya. Structure of DNA-cationic liposome complexes: DNA intercalation in multilamellar membranes in distinct interhelical packing regimes. *Science*, 275(5301):810–814, 1997.

[148] F. Reinitzer. Beiträge zur kenntniss des cholesterins. *Monatshefte für Chemie*, 9(1):421–441, 1888.

[149] H. Rezvantalab and R. G. Larson. Bridging dynamics of telechelic polymers between solid surfaces. *Macromolecules*, 51(5):2125–2137, 2018.

[150] H. Rezvantalab, G. Zhu, and R. G. Larson. The effect of wall depletion and hydrodynamic interactions on stress-gradient-induced polymer migration. *Soft matter*, 12(27):5883–5897, 2016.

[151] D. Richter, A. Baumgärtner, K. Binder, B. Ewen, and J. B. Hayter. Dynamics of collective fluctuations and Brownian motion in polymer melts. *Phys. Rev. Lett.*, 47(2):109–113, 1981.

[152] Jacob Riseman and John G. Kirkwood. The intrinsic viscosity, translational and rotatory diffusion constants of rod-like macromolecules in solution. *The Journal of Chemical Physics*, 18(4):512–516, 1950.

[153] H. Risken and T. Frank. *The Fokker-Planck Equation: Methods of Solution and Applications*. Springer-Verlag Berlin Heidelberg, 1996.

[154] R. M. Robertson, S. Laib, and D. E. Smith. Diffusion of isolated DNA molecules: dependence on length and topology. *P. Natl. Acad. Sci. USA*, 103(19):7310–7314, 2006.

[155] M. Robinson and M. Bruna. Particle-based and meshless methods with Aboria. *SoftwareX*, 6:172–178, 2017.

[156] M. Robinson, C. Luo, P. E. Farrell, R. Erban, and A. Majumdar. From molecular to continuum modelling of bistable liquid crystal devices. *Liq. Cryst.*, 44(14-15):2267–2284, 2017.

[157] E. Rolls and R. Erban. Multi-resolution polymer Brownian dynamics with hydrodynamic interactions. *J. Chem. Phys.*, 148(19):194111, 2018.

[158] E. Rolls, Y. Togashi, and R. Erban. Varying the resolution of the Rouse model on temporal and spatial scales: Application to multiscale modeling of DNA dynamics. *Multiscale Model. Sim.*, 15(4):1672–1693, 2017.

[159] A. Rosa and R. Everaers. Structure and dynamics of interphase chromosomes. *PLoS Comput. Biol.*, 4(8):e1000153, 2008.

[160] J. Rotne and S. Prager. Variational treatment of hydrodynamic interaction in polymers. *J. Chem. Phys.*, 50(11):4831–4837, 1969.

[161] P. E. Rouse. A theory of the linear viscoelastic properties of dilute solutions of coiling polymers. *J. Chem. Phys.*, 21(7):1272–1280, 1953.

[162] A. Saadat and B. Khomami. Computationally efficient algorithms for incorporation of hydrodynamic and excluded volume interactions in Brownian dynamics simulations: A comparative study of the Krylov subspace and Chebyshev based techniques. *J. Chem. Phys.*, 140(18):184903, 2014.

[163] R. K. Sachs, G. Van Den Engh, B. Trask, H. Yokota, and J. E. Hearst. A random-walk/giant-loop model for interphase chromosomes. *P. Natl. Acad. Sci.*, 92(7):2710–2714, 1995.

[164] Y. Saito and M. Mitsui. Stability analysis of numerical schemes for stochastic differential equations. *SIAM J. Numer. Anal.*, 33(6):2254–2267, 1996.

[165] A. L. Sanborn, S. S. P. Rao, S. Huang, N. C. Durand, M. H. Huntley, A. I. Jewett, I. D. Bochkov, D. Chinnappan, A. Cutkosky, J. Li, et al. Chromatin extrusion explains key features of loop and domain formation in wild-type and engineered genomes. *P. Natl. Acad. Sci.*, 112(47):E6456–E6465, 2015.

[166] K. Sangtae and J. K. Seppo. *Microhydrodynamics: Principles and Selected Applications*. Butterworth-Heinemann, 1991.

[167] C. M. Schroeder, E. S. G. Shaqfeh, and S. Chu. Effect of hydrodynamic interactions on DNA dynamics in extensional flow: Simulation and single molecule experiment. *Macromolecules*, 37(24):9242–9256, 2004.

[168] W. Schroeder, K. Martin, and . Lorensen. *The Visualization Toolkit, 4th edition*. Kitware, 2006.

[169] J. V. Selinger. *Introduction to the Theory of Soft Matter: From Ideal Gases to Liquid Crystals*. Springer International Publishing, 2015.

[170] J. Sgrignani and A. Magistrato. QM/MM MD simulations on the enzymatic pathway of the human flap endonuclease (hFEN1) elucidating common cleavage pathways to RNase H enzymes. *ACS Catal.*, 5(6):3864–3875, 2015.

[171] J. C. Shah, Y. Sadhale, and D. M. Chilukuri. Cubic phase gels as drug delivery systems. *Adv. Drug Delivery Rev.*, 47(2-3):229–250, 2001.

[172] E. S. G. Shaqfeh. The dynamics of single-molecule DNA in flow. *J. Non-Newtonian Fluid Mech.*, 130(1):1–28, 2005.

[173] S. Shinkai, T. Nozaki, K. Maeshima, and Y. Togashi. Dynamic nucleosome movement provides structural information of topological chromatin domains in living human cells. *PLOS Comput. Biol.*, 12(10):e1005136, 2016.

[174] D. E. Smith, T. T. Perkins, and S. Chu. Dynamical scaling of DNA diffusion coefficients. *Macromolecules*, 29(4):1372–1373, 1996.

[175] B. E. K. Snodin, F. Randisi, M. Mosayebi, P. Šulc, J. S. Schreck, F. Romano, T. E. Ouldridge, R. Tsukanov, E. Nir, A. A. Louis, and J. P. K. Doye. Introducing improved structural properties and salt dependence into a coarse-grained model of DNA. *J. Chem. Phys.*, 142(23):234901, 2015.

[176] M. Somasi, B. Khomami, N. J. Woo, J. S. Hur, and E. S. G. Shaqfeh. Brownian dynamics simulations of bead-rod and bead-spring chains: numerical algorithms and coarse-graining issues. *J. Non-Newtonian Fluid Mech.*, 108(1-3):227–255, 2002.

[177] T. J. Spencer, C. M. Care, R. M. Amos, and J. C. Jones. Zenithal bistable device: comparison of modeling and experiment. *Phys. Rev. E*, 82(2):021702, 2010.

[178] F. Sterpone, S. Doutreligne, T. T. Tran, S. Melchionna, M. Baaden, P. H. Nguyen, and P. Derreumaux. Multi-scale simulations of biological systems using the OPEP coarse-grained model. *Biochem. Biophys. Res. Commun.*, 498(2):296 – 304, 2018. Multiscale Modeling.

[179] I. W. Stewart. *The Static and Dynamic Continuum Theory of Liquid Crystals: A Mathematical Introduction*, volume 17. CRC Press, 2004.

[180] S. Takada, R. Kanada, C. Tan, T. Terakawa, W. Li, and H. Kenzaki. Modeling structural dynamics of biomolecular complexes by coarse-grained molecular simulations. *Acc. Chem. Res.*, 48(12):3026–3035, 2015.

[181] K. Takahashi, S. Tănase-Nicola, and P. R. ten Wolde. Spatio-temporal correlations can drastically change the response of a MAPK pathway. *P. Natl. Acad. Sci.*, 107(6):2473–2478, 2010.

[182] P. Tian and G. D. Smith. Translocation of a polymer chain across a nanopore: A Brownian dynamics simulation study. *J. Chem. Phys.*, 119(21):11475–11483, 2003.

[183] N. Tokuda, T. P. Terada, and M. Sasai. Dynamical modeling of three-dimensional genome organization in interphase budding yeast. *Biophys. J.*, 102(2):296–304, 2012.

[184] C. Tsakonas, A. J. Davidson, C. V. Brown, and N. J. Mottram. Multistable alignment states in nematic liquid crystal filled wells. *Appl. Phys. Lett.*, 90(11):111913, 2007.

[185] P. T. Underhill and P. S. Doyle. On the coarse-graining of polymers into bead-spring chains. *J. Non-Newtonian Fluid Mech.*, 122(1-3):3–31, 2004.

[186] L. Verlet. Computer "experiments" on classical fluids. I. Thermodynamical properties of Lennard-Jones molecules. *Phys. Rev.*, 159(1):98–103, 1967.

[187] E. G. Virga. *Variational Theories for Liquid Crystals*. Chapman and Hall/CRC, 1995.

[188] G. J. Vroege and H. N. W. Lekkerkerker. Phase transitions in lyotropic colloidal and polymer liquid crystals. *Rep. Prog. Phys.*, 55(8):1241–1309, 1992.

[189] J. Wang and H. Gao. A generalized bead-rod model for Brownian dynamics simulations of wormlike chains under strong confinement. *J. Chem. Phys.*, 123(8):084906, 2005.

[190] Harold R Warner Jr. Kinetic theory and rheology of dilute suspensions of finitely extendible dumbbells. *Ind. Eng. Chem. Fundamen.*, 11(3):379–387, 1972.

[191] L. E. Wedgewood, D. N. Ostrov, and R. B. Bird. A finitely extensible bead-spring chain model for dilute polymer solutions. *J. Non-Newtonian Fluid Mech.*, 40(1):119–139, 1991.

[192] R. Williams. Domains in liquid crystals. *J. Chem. Phys.*, 39(2):384–388, 1963.

[193] E. B. Wilson. Probable inference, the law of succession, and statistical inference. *J. Am. Stat. Assoc.*, 22(158):209–212, 1927.

[194] A. Wolffe. *Chromatin*. Academic Press, third edition, 2012.

[195] H. Wong, H. Marie-Nelly, S. Herbert, P. Carrivain, H. Blanc, R. Koszul, E. Fabre, and C. Zimmer. A predictive computational model of the dynamic 3D interphase yeast nucleus. *Curr. Biol.*, 22(20):1881–1890, 2012.

[196] H. Yamakawa. Transport properties of polymer chains in dilute solution: Hydrodynamic interaction. *J. Chem. Phys.*, 53(1):436–443, 1970.

[197] H. Yamamoto, T.and Kasama. Brownian dynamics simulation of multiphase suspension of disc-like particles and polymers. *Rheol. Acta*, 49(6):573–584, 2010.

[198] Takehiro Yamamoto, Takanori Suga, and Noriyasu Mori. Brownian dynamics simulation of orientational behavior, flow-induced structure, and rheological properties of a suspension of oblate spheroid particles under simple shear. *Physical Review E*, 72(2):021509, 2005.

[199] M. Zacharias and P. J. Hagerman. Influence of static and dynamic bends on the birefringence decay profile of RNA helices: Brownian dynamics simulations. *Biophys. J.*, 73(1):318–332, 1997.

[200] J. Zavadlav, R. Podgornik, and M. Praprotnik. Adaptive resolution simulation of a DNA molecule in salt solution. *J. Chem. Theory Comput.*, 11(10):5035–5044, 2015.

[201] Y. Zhang, J. J. de Pablo, and M. D. Graham. An immersed boundary method for Brownian dynamics simulation of polymers in complex geometries: Application to DNA flowing through a nanoslit with embedded nanopits. *J. Chem. Phys.*, 136(1):014901, 2012.

[202] Z. Zhang and D. Thirumalai. Dissecting the kinematics of the kinesin step. *Structure*, 20(4):628–640, 2012.

[203] B. H. Zimm. Dynamics of polymer molecules in dilute solution: Viscoelasticity, flow birefringence and dielectric loss. *J. Chem. Phys.*, 24(2):269–278, 1956.

[204] P. J. Zuk, E. Wajnryb, K. A. Mizerski, and P. Szymczak. Rotne-Prager-Yamakawa approximation for different-sized particles in application to macromolecular bead models. *J. Fluid Mech.*, 741:R5, 2014.